Additive manufacturing of bioceramic and biocomposite devices for bone repair

A thesis submitted to the Faculty of Science, Agriculture and Engineering for the Degree of Doctor of Philosophy

by

Priscila Melo

School of Engineering

Newcastle University

September 2019

Abstract

Advancements in technology allow for longer lifespans, creating the need for improved medical devices, especially in orthopaedics. New technologies like additive manufacturing (AM) allow the creation of patient-specific implants with complex shapes and controlled porous structures. This project aimed to exploit AM for the development of novel materials and devices within bone regeneration.

Several glass-ceramics are bioactive, presenting a similar composition to human bone, and improved mechanical properties. Here, we investigate the use of Apatite-Wollastonite (AW) as feedstock for AM techniques. Alumina-doped AW powders and polymer ceramic biocomposites were developed and their manufacturing processes optimized. Characterization of the materials, physicochemical and biological, proved the devices suitability for bone regeneration. The effect of alumina on the surface of AW particles on material processing, crystallization mechanism and mechanical properties was investigated. AW containing 0.13 wt% alumina at the surface was printed using binder jetting. Samples presented low open porosity and flexural modulus, but their bioactivity was preserved, including osteoconductivity. To explore the potential of unsintered AW glass composition, two biodegradable composite filaments were developed, with particles or fibres as fillers, at 5 wt% loading. Printed struts prepared with Fused Filament Fabrication showed mechanical properties comparable to cancellous bone and induced the differentiation of mesenchymal stromal cells to osteoblasts. It was determined that both composites expressed bioactivity, further enhancing cell biomineralisation, but the fibre filler expressed enhanced ion leaching and flexural modulus. In considering the use of AW glass and glass-ceramic as feedstock for AM processes, it is concluded that it is versatile biomaterial, in both powder and fibre form, and processable via different routes. Exploring the effects of its morphology and composition allows for higher freedom in material design, widening the application range within the market for devices targeting bone repair.

To my family, for the love, trust and support.

Acknowledgements

This PhD was an immense opportunity to grow both professionally personally, and for that I would like to acknowledge several people, and the institutions that received me.
First, I would like to thank my academic supervisory team, Professor Kenny Dalgarno, Dr. Ana Ferreira Duarte and Dr. Piergiorgio Gentile for their guidance, encouragement, patience and friendship. With the same emphasis, I thank my industrial supervisors, Dr Marlin Magallanes and Martyn Marshall, for the extra time spent aiding me during my internship at Glass Technology Services. To Marcin Kotlarz for his contribution towards this study, his commitment and will to learn, being the best student and colleague, one could wish to work with.

I would like to express my gratitude to the EPSRC, Newcastle University and Glass Technology Services for funding my research, and making this project possible.

To all the people that collaborated in my project, my most sincere acknowledgement. To Dr Kevin Waldron, Dr Emma Tarrant, Dr Matthew German and Dr Thomas Swift, I am grateful for kindly providing their services and expertise, essential for the successful scientific publications obtained. To my technical team at the School of Engineering, who were incredible and never hesitated whenever I needed help, or a good laugh. You were essential to my work, and unknowingly constantly improve student's lives.

A special acknowledgement to my friend, colleague and mentor, Dr Ricardo Ribeiro, for all the training, ideas, critiques and especially emotional support whenever I needed. To my dearest friends Annachiara Scalzone and James Smith for being by my side during this process, always armed with a smile and supporting kind words, and willing to brainstorm and give input to this project. To all my PhD colleagues and friends who shared this experience with me, starting in Nottingham and ending in Newcastle University. You made this country feel like home and your friendship made this journey unforgettable (from the casual pint to the panic of deadlines). An extended acknowledgment to my friends from Portugal who always encouraged me and endorsed me along these 4 years, even at the distance.

Finally, a special dedication to my family because without them this wouldn't be possible. To my father Fernando and my mother Ana, for always showing me how proud I made them, motivating me through their love and support, even behind teary eyes upon each departure. To my sisters Ana Sofia and Maria, this achievement is also yours, and will hopefully inspire you to follow your aspirations and never give up your dreams.

Table of contents

List of figures

List of tables

List of abbreviations

2D – Two-dimensional

3D – Three-dimensional

ABS - Acrylonitrile Butadiene Styrene

ALP - Alkaline Phosphatase

AM - Additive Manufacturing

AOR - Angle of Repose

AR – Alizarin Red

ASTM - American Society for Testing and Materials

AW - Apatite-Wollastonite

β-TCP – beta Tricalcium Phosphate

BG – Bone Grafting

BMPs - Bone Morphogenic Proteins

CAD – Computer Aided Design

CAM - Computer Aided Manufacturing

CaP - Calcium Phosphate

CT - Computer Tomography

DBM – Demineralised bone matrix

DED - Direct Energy deposition

DI - Di-ionized Water

DMEM - Dulbecco's Modified Eagle Medium

DO - Distraction Osteogenesis

DOSY - Diffusion Ordered Nuclear Magnetic Resonance Spectroscopy

DPBS - Dulbecco's Phosphate Buffered Solution

DSC - Differential Scanning Calorimetry

EBM - Electron Beam Manufacturing

ECM - Extracellular Matrix

FA – Fluorapatite

FDA - Food and Drug Administration

FDM - Fused Deposition Modelling

FFF - Fused Filament Fabrication

HA – Hydroxyapatite

HCA – Hydroxycarbonate

hMSCs - human Mesenchymal Stem Cells

HSCs - Hematopoietic Stem Cells

HSM - Hot Stage Microscopy

hTERT-MSCs – bone marrow derived human Mesenchymal Stromal Cells

ICP-MS - Inductively Coupled Plasma Mass Spectrometry

MD – Maltodextrin

LDM - Low-Temperature Deposition Manufacturing

LENS - Laser Engineered Net Shaping

LOM - Laminated Object Manufacturing

MRI - Magnetic Resonance Imaging

NA – Not Applicable

NMR - Nuclear Magnetic Resonance

PBS - Phosphate Buffered Solution

PCL – Polycaprolactone

PGA - Poly (glycolic acid)

PGF – Phosphate Glass Fibres

PLGA – Poly (lactic-co-glycolic acid)

PLLA - Poly (L-lactic acid)

PMMA - Poly (methyl methacrylate)

RM - Regenerative Medicine

SBF - Simulated Body Fluid

SEM - Scanning Electron Microscopy

sGAG - Sulphated Glycosaminoglycan

SLA – Stereolithography

SLM - Selective Laser Melting

SLS - Selective Laser Sintering

TE - Tissue Engineering

TGA - Thermogravimetric Analysis

TJA - Total Joint Arthroplasty

UHMWPE - Ultrahigh Molecular Weight Polyethylene

USD – United States Dollars

UV - Ultraviolet

XPS - X-ray Photoelectron Spectroscopy

XRCT – X-Ray Computer Tomography

XRD - X-Ray Diffraction

XRF - X-Ray Fluorescence

Y-TZP - Yttrium stabilised Tetragonal Zirconia

Chapter 1. Introduction

1.1 Background and clinical need

A need to invest in the orthopaedic area has emerged in the past years due to an increase in life expectancy. The development of an adequate bone substitute, economical and bioresorbable, has been a major challenge for orthopaedic, and reconstructive surgeons. Autografts have been the most common solution for bone defects, but with major drawbacks: 1) inconvenient for patients with degenerative bone diseases; 2) impractical for large defects as bone harvesting sites are limited. Allografts and xenografts report a high rate of rejection by the host due to antigenicity issues (Fujita *et al.*, 2000; Wang and Yeung, 2017). The current solutions for joint replacement or fracture fixation are mainly metal based, which leads to the problem of stress shielding, causing the bone to weaken and consequently the failure of the implant Metal implants, commonly titanium (Ti) based, are known for their ability to integrate within the body, and some studies claim an ability to create calcium (Ca) precipitation *in vitro.* These results do not translate directly *in vivo,* as researchers agree on the material's osteoconductivity but doubt the osteoinductivity (Shah, Thomsen and Palmquist, 2019). Most metal-based implants are bioinert, and the cell survival on them is an issue, in addition to bacterial infection. These problems are usually addressed with coatings and surface functionalisation, adding more steps to the manufacturing process (Zhang *et al.*, 2018). Such information turned the attention to other materials such as bioceramics and composites. New solutions were drafted based on the use of synthetic materials, capable of mimicking bone and withstand the needed loads of the application site. These materials would be used as support and regeneration platforms, and the base of the new investigative fields of Tissue Engineering (TE) and Regenerative Medicine (RM) (Ratner *et al.*, 2004; Wang and Yeung, 2017). These devices, support and enable tissue growth, and they can be bidimensional (2D) as films and 3D as scaffolds (Khang Kim, Moon Suk, Less, Hai Bang and Ltd., 2007; Meyer Thomas *et al.*, 2009). The access to additive manufacturing techniques, introduces a whole new range of possibilities in the TE and RM area. This additive approach increases the range in terms of design, shape and material choice for the scaffolds production (Butscher *et al.*, 2011). The technology has been used widely since it allows the design and fabrication of a device based on the patient's anatomical information, obtained by computer tomography (CT), or other techniques, and later converts it into a three-dimensional (3D) model. This offers an alternative to traditional manufacturing which is based on a subtractive philosophy, limited in terms of the design range and the option of raw materials (Javaid and

Haleem, 2019). For bone, glass-ceramics such as Apatite-Wollastonite (AW) have been used as scaffolds to study several pathologies because they combine bioactivity with mechanical strength (Wopenka and Pasteris, 2005; Xiang and Spector, 2006; Zwingenberger *et al.*, 2012; Gomes, Zocca and Guenster, 2015). In terms of applications, AW has been used as a bone repair scaffold, implant and filler (Fujita *et al.*, 2000; Kokubo, Kim and Kawashita, 2003; Ohtsuki, Kamitakahara and Miyazaki, 2009; Gomes *et al.*, 2014; Gomes, Zocca and Guenster, 2015). Recent studies report the processing of AW via binder jetting printing, followed by sintering, for load bearing applications (Alharbi, 2016; Mancuso *et al.*, 2017). The method of producing AW with Maltodextrin (MD) scaffolds using binder jetting printing showed successful primary results, with the scaffolds presenting mechanical properties mimicking those of cortical bone and osseointegration, when implanted in rat calvaria (Alharbi, 2016). AW is a versatile material but has not been studied as reinforcement of polymer and metallic matrices of biocomposites to enhance fixation and osteoconductivity (Juhasz *et al.*, 2004; Navarro *et al.*, 2008). Since biodegradability is desirable, many polymers with mechanical properties within the range of bone have been explored, e.g. poly (L-lactic acid) (PLLA). The reaction of the cells upon implantation is also under study, being the main goal the translation from osteoconductive to osteoinductive (Zwingenberger *et al.*, 2012; Winkler *et al.*, 2018). A material that is osteoconductive can support osteoblast growth and proliferation whilst being osteoinductive implies the differentiation of bone progenitor cells into osteoblasts. The addition of a bioactive material such as hydroxyapatite (HA) and AW, is known to promote tissue growth adjacent to the implant and could possibly enhance the differentiation of human mesenchymal stem cells (Boccaccini and Maquet, 2003; Wang, 2003; Ahmed *et al.*, 2011). Up to date, studies on biocomposites using AM are limited, with most of them consisting of polymer matrices reinforced with CaP particles (Yasa and Ersoy, 2018). Fibre-reinforced composites have proved to enhance mechanical properties, whilst promoting osteoconduction (Ahmed *et al.*, 2011; Felfel *et al.*, 2013). Multiple combinations can be used in terms of fibre configuration and length, but most studies have focused on long fibres, in a continuous or random configuration. For short fibres, the effect of this form on the bioactivity are unknown, however the influence of ion leaching from Ca-doped phosphate short glass fibres is reported and appears to contribute for the biomineralization of human Mesenchymal Stromal Cells (hMSCs) (Melo *et al.*, 2019).

1.2 Aims and objectives

The aim of this project is to investigate the physicochemical and biological properties of bioceramics and biocomposites, based on AW provided by Glass Technology Services (Sheffield, United Kingdom) and produced via AM, as devices for bone repair. A priority was to create a repeatable manufacturing process encompassing the development of biomaterials with a good combination of mechanical properties, chemical composition, resorption rate and osteoconductive and osteoinductive abilities.

The main objectives consist on:

- Literature review of biomaterials used for bone repairs and their processing techniques, including AM.
- Development and characterization of biomaterials for bone applications;
- Development and optimization of manufacturing processes for the selected biomaterials, using AM to produce complex 3D structures capable of mimicking bone architecture;
- Assess the combination of mechanical and biological properties of the developed structures in terms or suitability for medical devices.

1.3 Thesis structure

This first chapter has presented the introduction to the subject as well as the aim of the project and the objectives drawn to achieve it. The second chapter reviews bone biology, biomaterials in orthopaedics, and manufacturing techniques previously and currently used to prepare bone implants and scaffolds. The third chapter is the materials and methods and is divided into two sections: 1) standard materials and methods; 2) developed materials and methods. The fourth chapter is based on a collaborative work, initiated in the beginning of the PhD project. This chapter presents the optimisation of AW sintering process, by exploring the influence of alumina as an impurity, and as dopant. This would allow the production of AW implants using binder jetting and sintering, described in the fifth chapter. The knowledge obtained in the fourth chapter creates the base for the understanding of the results obtained for the structural and mechanical properties of the printed parts. Taking advantage of AW properties, namely the bioactivity, and using a well-known biocompatible polymer, the sixth chapter focuses on the development of two types of PLLA-AW biocomposites, consisting on a matrix of PLLA containing AW in the form of particles or fibres. An overall discussion chapter considers the performance of all the materials and processing routes, to identify the most

promising materials and devices for clinical applications. This leads to the conclusions and recommendations for future work.

Chapter 2. Literature Review

In order to understand and design effective solution for tissue repair or substitution, it is essential to know its composition, properties and self-maintenance mechanisms. This section gives an overview on bone properties and composition alongside its regeneration mechanisms, related to bone loss. It then introduces the materials used in orthopaedics alongside the explanation on their properties and main applications. An in-depth approach is taken for the bioceramics and biocomposites since they are the materials developed in this project. Finally, an overview of AM of ceramics and composites is done, and the applications targeted.

2.1 Bone composition and morphology

The human body is composed of 213 bones, excluding sesamoid bones, which are modelled during an individual's lifetime. Bones are connected through joints to form a stable and flexible structure, the skeleton. The skeleton is responsible for muscle support, organ and soft tissue protection, body motion, and mineral storage. Histologically, bone is considered a connective tissue, which is composed by two phases: a type I collagen, an organic matrix that incorporates living cells, and the mineral phase containing hydroxyapatite (HA) crystals (D. W. Buck and Dumanian, 2012).

2.1.1 Physicochemical properties of bone

Composition and microstructure

Bone tissue consists of two phases, organic and inorganic. The inorganic portion consists of a mineral phase, HA, with a base chemical composition $Ca_5(PO_4)_3X$, where X could be either an OH- ion or a $CO_{2-3,}$ depending on the area and the age (K.H. Jürgen Buschow, Robert W. Cahn, 3001). The mineral phase accounts for 60% of bone weight and provide its consistency. The remaining 40% include 30% of organic type I collagen matrix and 10% of water. Volume wise, the percentages change faintly, with approximate values of 40% for the mineral phase, 25% for the water and 35% for the organic matrix. Most water in bone is located around the collagen fibres and ground substances, but an important part remains in the cavities that contain bone cells, and in nutrient delivery canals that feed and clean bone tissue (Frankel and Margareta, 2012).

At a macroscopic level, an adult skeleton is made of cortical and cancellous bone, with a weight percentage of 80% and 20%, respectively. Figure 1 shows both cortical and cancellous

phases, as well as their internal organization (Ratner *et al.*, 2004; D. W. Buck and Dumanian, 2012). Cortical bone is structured into single units, the osteons, which are composed of concentric layers that form around the Haversian canal. These layers are intercepted by blood vessels that pass through the Volkmann's canals, a system of canaliculi responsible for blood supply to the osteon layers. Osteons are highly compacted in the periosteal layer, which leads to cortical bone's high density (90-95%) and mechanical strength, needed to support cyclic loads without breakage. On the other hand, cancellous bone is highly porous due to its organization into a mesh of trabeculae, with a diameter varying between 150 μm and 300 μm. This design results in porosity values ranging from 50 to 90%, consequently a greater surface area. This translates into an improved flow of growth factors and nutrients. The overall result is an increase of remodelling, and a fast response to mechanical stimuli (Ratner *et al.*, 2004; D. W. Buck and Dumanian, 2012). All bones, excluding the joint area, are surrounded by the periosteum, a dense fibrous layer permeated with blood vessels and nerve fibres. On its inner side, the periosteum possesses an osteogenic layer containing osteoblasts, that will promote bone growth and repairing. Long bones have another membrane, the endosteum, located at the medullary cavity, encompassing giant multinucleated osteoclasts, and osteoblasts, that also aid on bone growth and remodelling. Altogether, the assembly of these layers provide bone with its mechanical properties, characteristic of a biphasic composite material made of a flexible matrix with brittle crystals embed in it. The combination of these materials result on a higher mechanical strength, which wouldn't be possible if they were isolated (Frankel and Margareta, 2012).

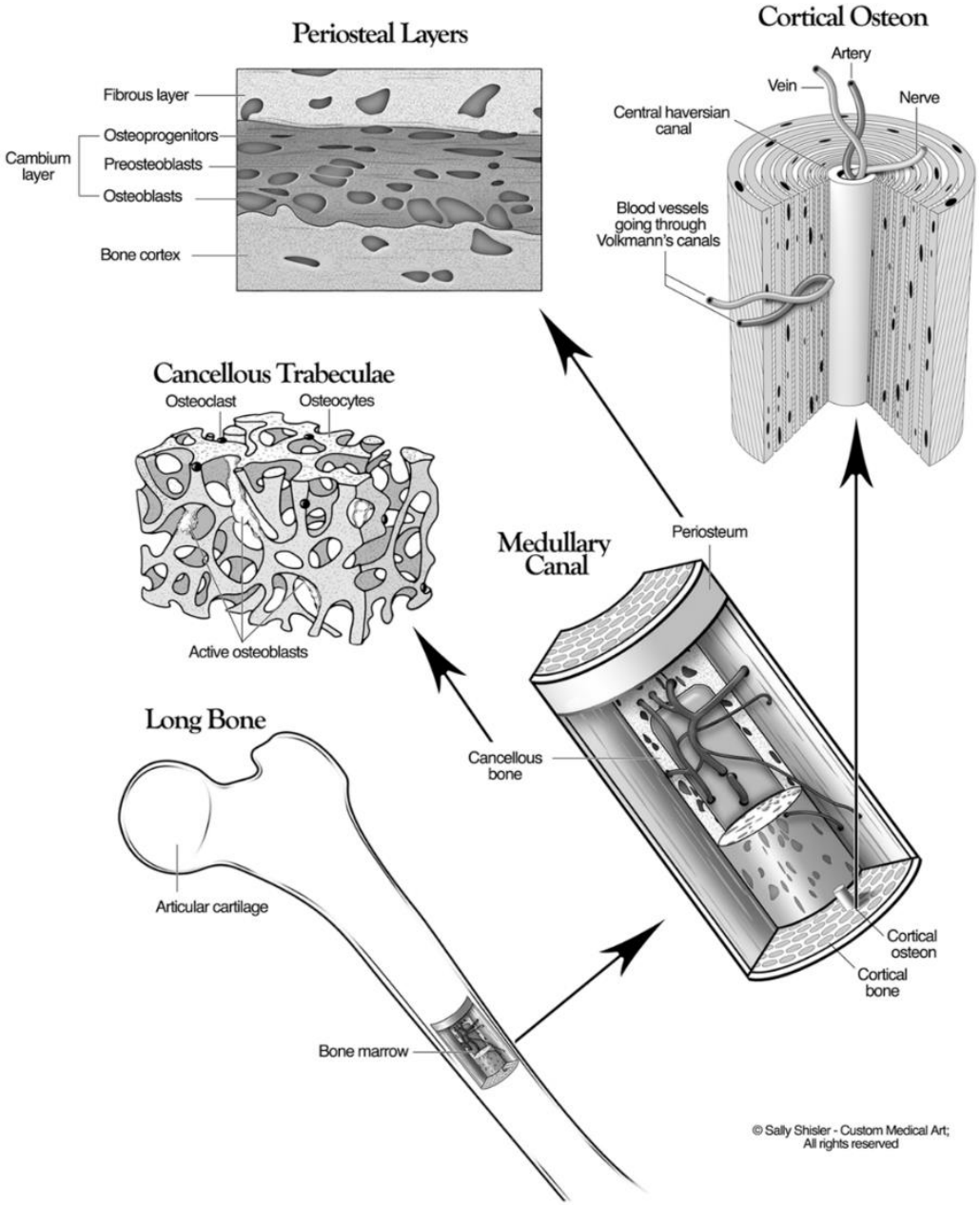

Figure 1 - Bone anatomy and histology. Illustration of bone tissue organisation, at macroscopic and microscopic level (D. W. Buck and Dumanian, 2012).

Bone changes in size and shape using specific processes controlled by the conjugal activity of bone cells and biofactors (Marion and Mao, 2006; D. W. Buck and Dumanian, 2012). The cells responsible for bone formation, maintenance, protection and resorption are osteoblasts, osteocytes, lining cells and osteoclasts, respectively (figure 2). These cells differ in both function and origin. Osteoblasts, lining cells and osteocytes originate from MSCs, the osteoprogenitor cells, whilst osteoclasts originate from hematopoietic stem cells (HSCs). Regarding their position in bone, osteoblasts, bone lining cells and osteoclasts are located at the bone surface, while osteocytes remain inside the matrix, in order to maintain and develop

it. Cells development and placement within the bone formation mechanism is also demonstrated on figure 2. The activation and control mechanisms involved in bone formation rely on intricate interactions between an individual's genetic potential, surrounding environment, and nutritional factors (Rahman *et al.*, 2015).

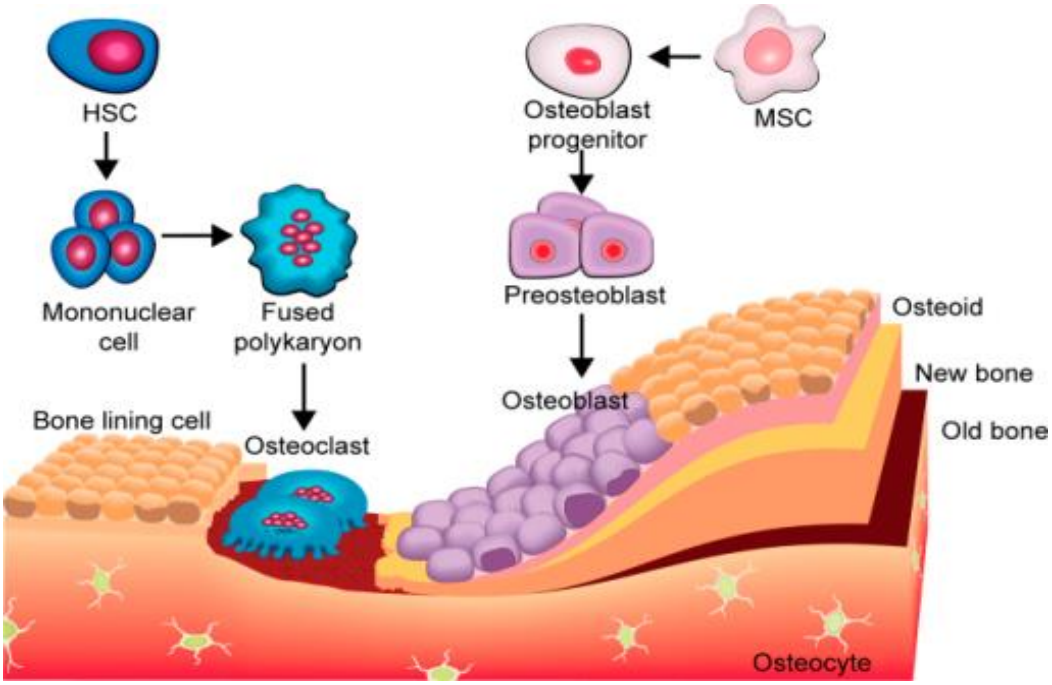

Figure 2 - The evolution of osteoblasts and osteoclasts in bone formation. Adapted from (Rahman *et al.*, 2015).

Mechanical properties

The most important mechanical properties of bone are strength, stiffness and toughness (table 1). The mineral phase of bone is known for the contribution towards the tissue's strength, but the collagen matrix is fundamental for toughness and post-yield properties (Wang *et al.*, 2000; Frankel and Margareta, 2012). Studies performed by Wang *et al.* showed a decrease in bone's toughness after denaturating the collagen, with an overall strength loss of 60%. They unravel the connection between collagen content and failure energy, pointing towards a relation between type I collagen and the energy required for matrix failure, despite size or geometry. The results plotted in figure 3 relate to bone phases and their stress-strain relationship. Stress is considered the load applied to the sample and is measured in Newtons per meter squared (N/m^2) or Pascal (Pa). Strain is the deformation resultant from the load application, obtained from the division of the linear deformation by the original length, the reason why it is non-dimensional. In figure 3a, the mechanical behaviour of collagen is presented as the relation

between stress and strain before and after denaturation. The results show a decrease in stress after denaturation, which has implications on the bone health and performance under loading. Figure 3b demonstrates the deformation of cortical bone under tension test. From A to B, bone presents an elastic behaviour, therefore it can return to its initial shape. Past point B the plastic domain is inserted and any deformation induced is permanent, up to point C where the structure fails, in this case, bone fractures (Frankel and Margareta, 2012).

Bone	**Bending strength (in Ringer's solution) (MPa)**	**Fracture toughness ($MPa \cdot m^{-1/2}$)**	**Compressive strength (MPa)**	**Young's modulus (GPa)**
Cortical	50-150	2-12	100-230	7-30
Trabecular	NA	NA	2-12	0.05-0.5

Table 1 - Cortical and Trabecular bone mechanical properties (Jones and Hench, 2006).

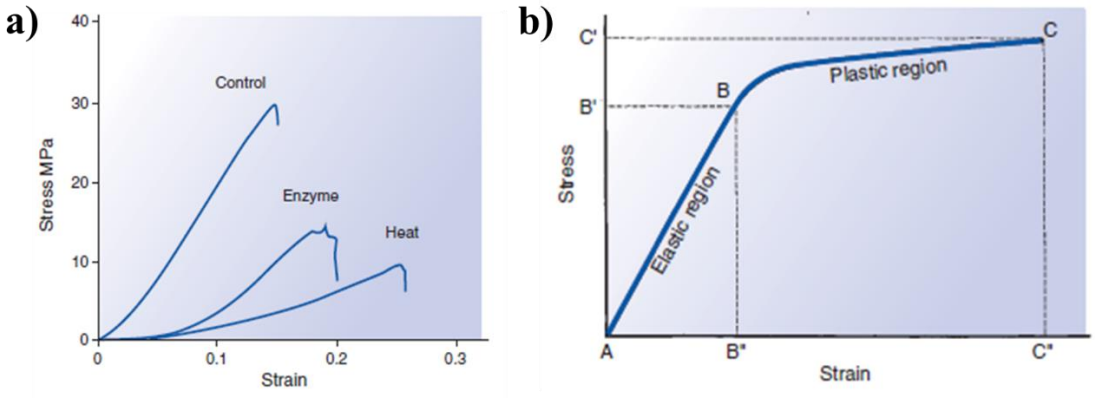

Figure 3 - Stress-strain curves in MPa for: a) collagen network mechanical behaviour under heat and enzyme treatment. Weakening of the network upon collagen denaturation. b) Tension test on cortical bone sample. A considered the initial point. Point B representing the transition point of elastic to plastic, where permanent deformation occurs. B' represents the yield stress value, load per unit per area, preceding plastic deformation, and B'' the yield strain, referring to the deformation caused by B'. The ultimate failure point and respective causing load and consequent deformation, are represented by C, C' and C'' respectively (Frankel and Margareta, 2012).

Both bone phases behave distinctly under loading, however they act as a single composite structure. Material characterization demands the standardisation of testing conditions and specimens, to guarantee the results uniformity. Bone's stress and strain can be measured by pulling the ends of the sample and monitoring the middle section between the two-gauge arms (figure 4a). The result is a stress-strain curve. The area under the curve corresponds to the

toughness, the materials' energy storage capacity, mainly the amount of energy needed to deform the material. The ability of the material to deform, stiffness, is provided by the Young's Modulus (E), which is obtained when stress (σ) is divided by strain (ε) in a determined point (equation 1) (Callister and Rethwisch, 2007; Frankel and Margareta, 2012).

$$E = \frac{\sigma}{\varepsilon} \; GPa \quad Equation \; (1)$$

Cortical bone is stiffer than trabecular bone, meaning it can withstand higher loads, and deforms less before fracturing. Experiments performed by Keaveny and Hayes in 1993 demonstrated that, *in vitro*, cortical bone sustained 1.5% to 2% of the strain before yielding while trabecular bone values raised to 50% before yield starts. Elastic properties change with age, being young bone more ductile and older bone more brittle, due to the loss of bone density. Loading rate is also important once its increase leads to a faster yielding. Under tension (figure 4b), yielding happens due to osteon debonding in areas with microfractures. Under compression, it results from cracking of osteons and/or interstitial lamellae (Keaveny and Hayes, 1993; Frankel and Margareta, 2012).

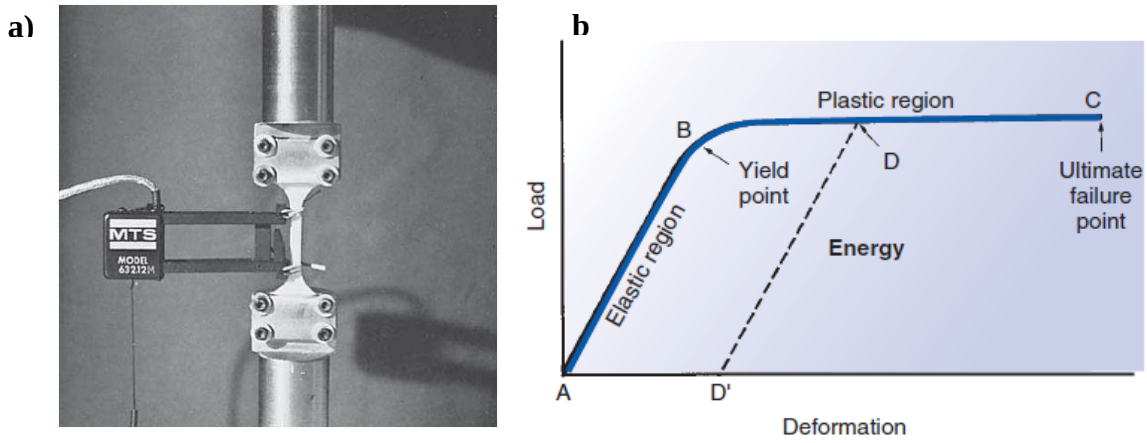

Figure 4 - Tension test of a standardized bone sample (cortical and trabecular). a) Tensile strength testing machine where the strain between the two-gauge arms is measured with a strain gauge. Stress is calculated from the total load measured. b) Load-deformation curve of a standardized bone sample (Frankel and Margareta, 2012)

Cortical and trabecular bone possess different limits when faced with loading (table 2), e. g. cortical bone can withstand up to 190 MPa, under compression, while trabecular bone will fail after 50 MPa. Tension values follow the same fashion, with 130 MPa and 8 MPa for cortical and trabecular bone, respectively. Load direction directly affects these values with cortical

bone experiencing a decrease of 17 GPa to 11 GPa when load changes from longitudinal/axial to transverse. The values for strength and Young's modulus of cortical bone, according to the load direction, are compiled on table 2 (Burstein, Reilly and Martens, 1976; Frankel and Margareta, 2012).

Load direction	**Average anisotropic stress properties (MPa)**		**Anisotropic Young's modulus (GPa)**
	Tension	Compression	
Longitudinal	133.00	193.00	17.00
Transverse	51.00	133.00	11.00
Shear	68.00		3.30

Table 2 - Average biomechanical properties of cortical bone according to the direction of the load (Burstein, Reilly and Martens, 1976; Frankel and Margareta, 2012).

2.1.2 Bone healing mechanisms

Bone undergoes several and continuous transformations during life: growth, modelling and remodelling. These mechanisms aim to maintain bone mass and bone shape daily, most importantly after fractures or arising defects. Bone modelling consists on bone overall re-shaping process in response to a mechanical and/or physiological stimulus. This shape is maintained through the remodelling process, where old bone is resorbed by osteoclast and new bone is produced by osteoblast, resulting in a new osteon (D. W. Buck and Dumanian, 2012). According to Wolff's law, a long bone's shape adapts to accommodate the loads placed on it, in the absence of stress bone is resorbed whilst in stressed areas it is reinforced. This knowledge justifies bone resorption for cases like edentulous mandibles, where the lack of mastication forces leads to bone resorption, impeding a prosthesis application. Areas with bone grafts, shielded from mechanical stresses, can also weaken due to resorption, leading to either a fracture or defects at the implantation site (Clarke, 2008; D. W. Buck and Dumanian, 2012).

The understanding of how bone regenerates is essential for the development of healing strategies. The healing process occurs in the presence of bone loss, e.g. due to fracture or upon tumour removal. Bone's healing cascade is demonstrated in figure 5. It is initiated by chondrocyte proliferation, followed by hypertrophy and calcification. The regeneration is triggered by an inflammatory response that leads to the formation of a hematoma, shadowed by tissue granulation, denominated cartilaginous callus. The callus is replaced by

endochondral tissue that spreads in between the fracture ends and the periosteal sites. The callus chondrocytes proliferate and hypertrophy causing the matrix calcification, making it unfertile. During hypertrophy, the chondrocytes release alkaline phosphatase and angiogenic factors, leading to a capillary ingrowth and migration of osteoprogenitor cells, that later differentiate into osteoblasts. The mineralized cartilage is then resorbed and replaced by new bone (D. W. Buck and Dumanian, 2012; Marsell and Einhorn, 2012).

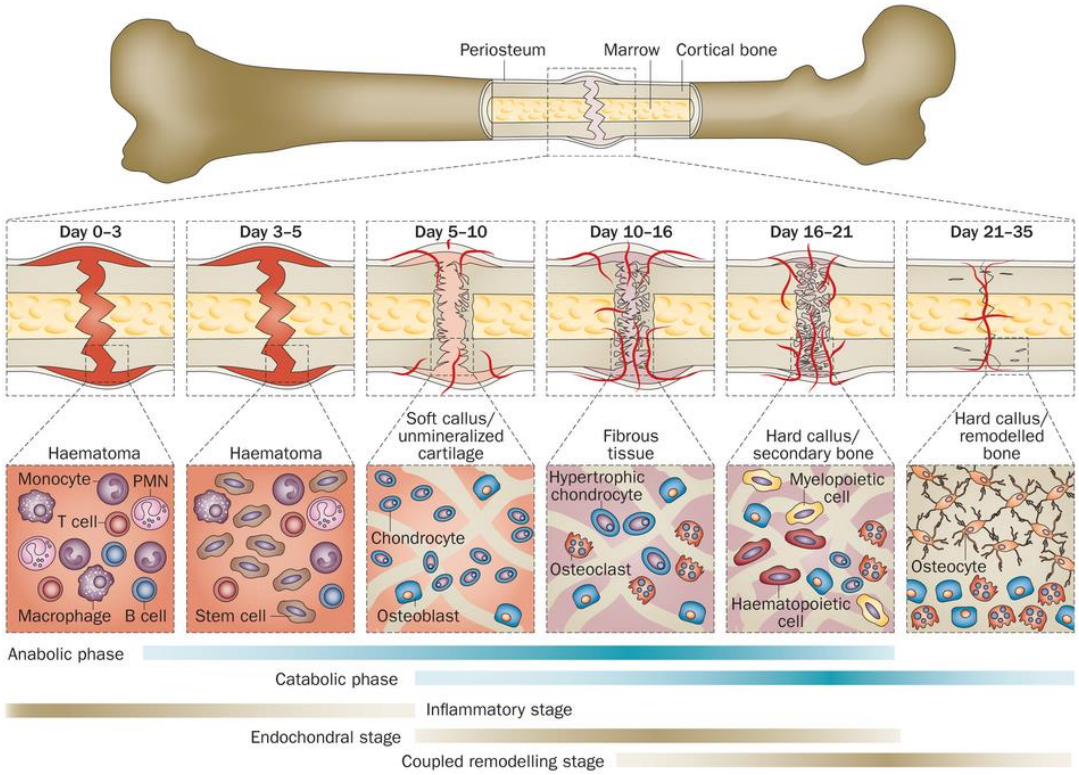

Figure 5 - Bone healing process, divided by metabolic stages. The transformation at a morphological level between the first day of injury and the completion of the regeneration process. Cell action alongside the major stages and their contribution for the morphological changes. Adapted from (Einhorn and Gerstenfeld, 2015).

2.2 Clinical approaches for bone defects

The main goal of defect treatment is to speed up the healing whilst avoiding significant deformity or limb shortening. The treatment used depends on the location and type of defect, the muscle and body loading, and the various passive soft tissue constraints such as ligaments (Nordin and Frankel, 2012). The determining factors for an optimal treatment method are:

- mechanical loading and its type (tension, bending and/or torsion) and magnitude of the forces acting on the site (cyclic means additional strength will be needed to avoid failure by fatigue);

- quality of the bone where the device will be fixed;
- nature of the original injury and the amount of soft tissue damage;
- other surgical and anatomic considerations such as exposure (possible scarring and vascular compromise), device fitting and neurovascular structures at risk (Nordin and Frankel, 2012).

2.2.1 Cell and tissue-based therapies

To optimize the care of patients with bone disease or suffering bone fractures, it is imperative to understand the mechanisms that led to the problem. Surgeons frequently encounter cases where the successful outcome depends on this knowledge. The clinical solutions developed included the application of Wolff's law, on distraction osteogenesis (DO), and bone transfer to the fracture site, bone grafting (BG). DO consists on the creation of a bone gap that is submitted to tension. The constant tension prevents callus mineralization and causes the area to divide into zones, where the following processes elapse: 1) collagen fibre formation; 2) early bone formation; 3) matrix mineralization and organization into lamellae. Despite the success of DO, BG became the gold standard procedure to heal bone damage (D. Buck and Dumanian, 2012).

The first experiment performed using BG dates from 1611-1666, with the work of Mekeeren, but its popularity arose in 1800s and the 1900s (Haeseker, 1988; D. Buck and Dumanian, 2012). In 1975, Taylor et al. demonstrated the success of the first vascularized graft, from a free fibula flap, on the healing of a mandible defect, implementing the practice. The technique was later modified by Kokosis et al. in a work published in 2016 (Kokosis *et al.*, 2016). The grafts are harvested from both cortical and cancellous bone, being the common harvesting sites the iliac crest, femur and tibia (table 3). The main advantages of BG are the rapid vascularization, immediate mechanical strength and low donor-site morbidity, however, for bigger defects, tissue availability is limited. For some grafts, slow vascularization and incorporation might jeopardize the patient's recovery requiring another intervention, which increases clinical costs. Another important factor for bone graft incorporation is the patient's health state. If treatments such as chemotherapy and radiotherapy, are being applied to the body, a negative response could endanger the patient's life. Despite the disadvantages, bone grafts contributed for the study of bone morphogenic proteins (BMPs) and its regenerative capacities. This allowed the exploration of new alternatives such as synthetic materials, specifically biomaterials (D. Buck and Dumanian, 2012).

Graft type	Revascularization	Clinical case	Advantage	Disadvantage
Cancellous	Rapid (≤ 2 days)	Non union Small defects Cavities	Rapid revascularization Conformability Low donor-site morbidity	Limited supply Size limitations Slow revascularization for cortical and cancellous grafts Loss of strength 6-12 months after the surgery Donor-site morbidity Require expertise Long operative time that may cause complications
Cortical	Slow (≥ 2 months)	Large gaps Lack of mechanical strength	Immediate mechanical strength is provided	
Vascularized	Rapid (most of graft osteocytes remain alive after implantation)	Large bone gaps (> 6 cm) Composite defects	Immediate strength Minimal graft necrosis Rapid incorporation Normal healing and remodelling	

Table 3 - Bone grafts applications, advantages and disadvantages (D. Buck and Dumanian, 2012).

In summary, the bone healing pathway can follow an electrical, mechanical or biological approach, or a combination of these. The strategies used range from biological enhancement of the process using BMPs, or growth factors, to electrical shock waves. Recently, RM in association with TE provided other solutions based on the use of osteogenic cells and bioactive molecules that are seeded onto scaffolds, i.e. tissue supporting platforms (Johnson, Urist and Finerman, 1992; Mistry, 2005; Giannoudis, Psarakis and Kontakis, 2007).

2.2.2 Biomaterials as bone replacements

Biomaterials are present in our society since prehistorical times, e.g. linen, which was used by the Egyptians, 32 000 years ago, to suture big wounds. The term biomaterials is defined as *''any substance or combination of substances, other than drugs, synthetic or natural in origin, which can be used for any period of time, which augments or replaces partially or totally any tissue, organ or function of the body, in order to maintain or improve the quality of life of the individual''*, a definition applied by the American National Institute of Health.

The ability of a material to be integrated within an organism, without an adverse response by the host, was defined as biocompatibility (Ratner *et al.*, 2004; D. Buck and Dumanian, 2012). In orthopaedics, biomaterials can be used as bone healers and/or substitutes, e.g. partial or total joint replacement prosthesis, fixation devices, implants, cements and bone fillers. Some examples of biomaterials and their application in orthopaedics and dentistry are shown in table 4, including suppliers and product brands (Ratner *et al.*, 2004).

Materials	Application	Product and supplier
Titanium alloys (Ti-6%Al-4%V)	Plates, screws, Total joint arthroplasty (TJA) components (non-bearing surface), coatings, dental implants	Plasmafit™- Aesculap (AESCULAP implant systems, no date) LCU® Classic uncemented - LINK® (LINK, no date) Continuum® acetabular system, Trinca® and Trinica® select anterior cervical plate system, Dental temporary abutment - ZIMMER® (ZIMMER, no date)
Cobalt-Chromium-Molybdenum (Co-Cr-Mo)	TJA components	Revitan® revision hip system, CPT® hip system, Maxera™ cup - ZIMMER®
Stainless steel	TJA components, screws, plates, cabling	DVR anatomic plate® - Biomet (Biomet, no date) Protosul S30 – Sulzer (now Centrepulse Orthopedics Inc)
Poly (methyl methacrylate) (PMMA)	Bone cement	Vertebro X - SOMATEX(Technologies, no date) (≈90€ per piece) CEMFIX 3, GENTAFIX – Teknimed (Medical Expo, no date)
Calcium phosphates (HA and β-TCP)	Small bone defects	IngeniOs® HA or β-TCP Bone Graft Substitute - ZIMMER® Maxresorb® - Botiss (65€ per 0.5ml) Maxresorb® injectable - Botiss (105€ per 0.5ml)

Table 4 - Example of biomaterials and their applications in orthopaedics and dentistry.

Bone devices can be made of:

1. Polymers
    a. Natural, e.g. cellulose, collagen and alginate;
    b. Synthetic, e.g. PMMA for cementation and ultrahigh molecular weight polyethylene (UHMWPE) as low friction inserts for TJA;
2. Metals, e.g. stainless steel and Ti alloys for fixation plates, screws and TJA components;
3. Ceramics, glasses and glass-ceramics (bioceramics and bioactive glasses and glass-ceramics), e.g. alumina and zirconia as bearing surfaces on TJA, Bioglass 45S5® and Ceravital® as implants and bone fillers;
4. Composites, e.g. UHMWPE reinforced with carbon fibre and HA-poly (ethylene) (Ratner *et al.*, 2004).

A device targeting bone defects or fractures, including load bearing applications, must be mechanically strong, making ceramics and metals highly considerable. Despite their high mechanical strength and fracture toughness, metals cause stress shielding and bone resorption due to the big difference in material properties comparing to bone, and the absence of an osteoinductive character. Alongside these faults, they are not biodegradable, one of the market requisites (Kokubo, 2008). Ceramics such as calcium phosphates (CaP) and bioglasses, have similar composition to bone mineral phase (HA which is a CaP) and a bioactive character (Kokubo, 2008). Another advantage is the growing market for these materials for orthopedic applications, estimated at United States dollars (USD) $ 16.3 billion by 2020. A compound annual growth rate of 6.4% between 2015 and 2020 has been driven by development and evolution of new dental and orthopaedic implants, alongside their increasing global demand (marketsandmarkets.com, 2016). A second report on bioactive ceramics was performed by Technavio for the period of 2016-2020, registering an increase to USD $ 2.14 billion on the investment. These values are justified mainly by an increased demand from organ failure and replacement procedures, orthodontics, and several other coating applications, with special emphasis on the aging population. The support from the scientific community on research carried out in the field of oncology is another prominent driver for the market (Technavio, 2016). Based on these values, the next section describes the potential of RM, properties of bioactive ceramics and regarding bone and the use of bioceramics.

2.3 Regenerative medicine applied to bone defects

To address the problem with present therapies for bone defects, a shift in the clinical approach from synthetic implants and tissue grafts to RM, was done. RM involves implantation of a new generation of acellular or cell seeded scaffolds, immediately after injury or bone removal. Depending on the application and the target tissue, implants can be made of a variety of biomaterials, and processed using different techniques (Butscher *et al.*, 2011).

2.3.1 Tissue-implant interaction vs material nature

When designing a device, the first step to guarantee the implantation success is the tissue attachment. The tissue attachment to the implant surface depends on the material reactivity, which influences the thickness of the layer between bone and implant. There are 4 types of implant, according to its nature:

1. Inert: dense, nonporous, inert materials where bone grows into the surface irregularities, cementing the device into the tissues.
2. Porous: bone ingrowth is the major cause of fixation, called biological fixation, regardless of the material. The ingrowth of tissue into the implant pores increases interfacial area, resulting in inertial resistance to the movement. However, the high degree of porosity compromises mechanical performance, making them unsuitable for load bearing applications.
3. Resorbable: materials such as CaPs and some polymeric bone fillers degrade gradually with time, then are replaced by the host's tissue. It is ideal short-term, but not for long term applications where maintaining the strength and stability of the interface is key.
4. Bioactive: bioactive glasses and some glass-ceramics, stimulate the formation of a hydroxycarbonate apatite (HCA) layer, which works as the interface between tissue and implant allowing bonding to both hard and soft tissues (Jones and Hench, 2006). The chemical process for the formation of HCA layer is demonstrated on figure 6.

<u>The bioactivity process</u>

The HCA layer formed for bioactive materials is chemically equivalent to bone's mineral phase and capable of handling a substantial mechanical load. In cases where it was tested, the failure would commonly be verified on the implant or the bone itself, not for the interface. To avoid failure, it is necessary to quantify the time necessary for these changes to happen, respective to material type. The rate of HCA layer formation and posterior crystallization is essential for the success of the bonding and varies greatly. Extremely slow rates of formation prevent bonding, therefore the material is no longer bioactive (Kokubo, 2008).

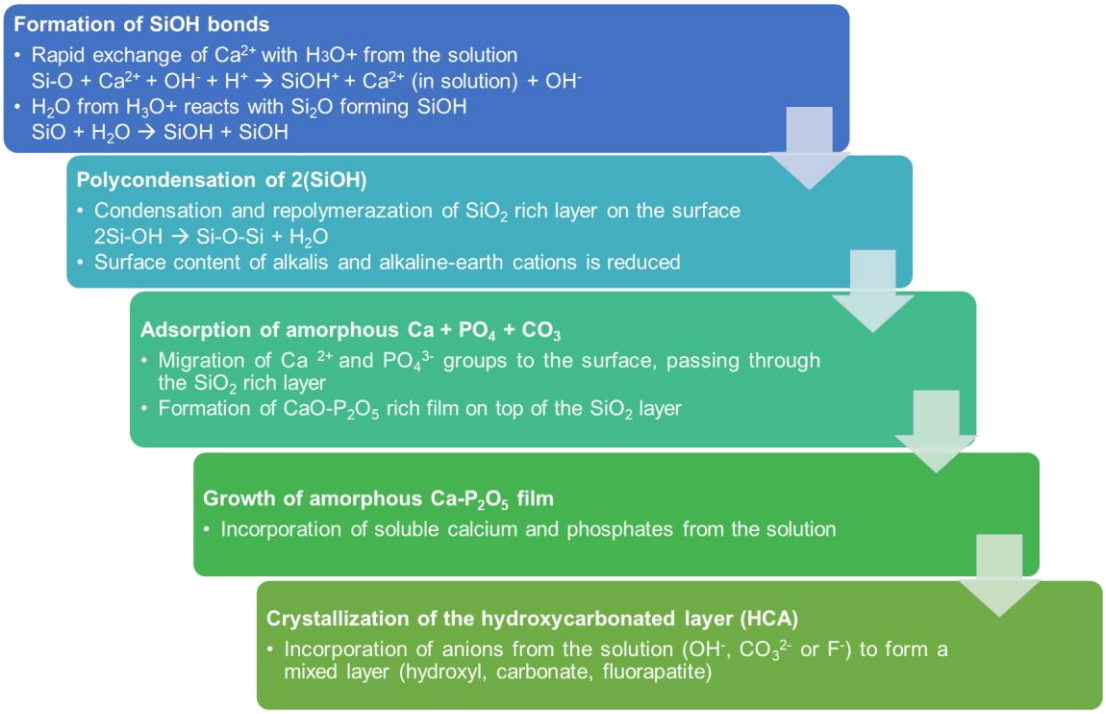

Figure 6 - Surface reaction stages in the interface between bioactive ceramics and bone (Hench, 1998).

2.3.2 Bone regeneration in defect sites: requisites and state of the art

Bone implants are meant to mimic bone tissue's chemical and physical characteristics, alongside the microstructure. According to Hutmatcher et al. (Hutmacher, 2000), a bone implant should be biocompatible and bioresorbable, with a controlled degradation rate to match the tissue regeneration. The surface chemistry should promote cell attachment, proliferation and differentiation. For bone, 3D highly interconnected porous structures are desirable, to allow nutrient flow and cell migration (Hollister, 2005). Bone is porous and supports cyclic loads daily, meaning a balance between porosity and mechanical properties is sought. Pore size and distribution must be carefully defined and adapted to the application, namely defect size and location within the body. Such balance relies highly on the material properties, namely the similarity to bone composition, mechanical strength and bone cells stimulation (both proliferation and differentiation) (Nordin and Frankel, 2012; Henkel *et al.*, 2013). Some common requisites for bone regeneration implants are listed in table 5. These requirements vary with the material used, therefore serve only as a guideline (Chu Liu, Xuanyong, 2008).

Parameters	Requirements
Porosity	Maximum possible to maintain mechanical stability
Pore size	200-400 μm
Pore structure	Interconnected

Table 5 - Base requisites to design a porous implant for bone regeneration (Chu Liu, Xuanyong, 2008).

2.3.3 Bone regeneration in fracture fixation devices

The use of metals is common, with Ti plates and screws on the top of the market, but problems like stress shielding lead to bone weakening, resulting on implant loosening or secondary fractures. The therapies used in bone fracture fixation are listed on table 6, alongside their advantages and disadvantages. An implant targeting bone fractures, possibly in load bearing areas, demands a strong material. Metals are not biodegradable or bioactive, therefore, in the context of RM, they are not suitable. Ceramics such as CaPs and bioglasses, are a highly-studied option, not only for their similar composition to bone mineral phase (HA), but for their bioactive character (Kokubo, 2008). Composites, namely fibre reinforced have been studied for this application, consisting mostly of polymer matrices with bioceramics fillers. Common fillers are phosphate glass and silane-treated alumina-silicate glass (Goldberg and Burstone, 1992; Ahmed *et al.*, 2011).

Therapy	Advantages	Disadvantages
Electrical stimulation	Osteoconductive Mimics the body's electrical stimulus Constant stimulation of the bone increases patient compliance	Synovial pseudarthrosis Does not address deformity problems • Possible electrode dislodgement and surgical procedure needed to insert and remove the electrodes (increased risk of infection) • Dose dependant • Device must be worn between 30 min to 24h resulting in skin irritation and decrease patient compliance
External fixation	Immediate immobilization High levels of stability Suitable for comminute fractures Good 2nd option upon intramedullary nailing failure	Damage to soft and nervous tissue Infection on pin-site, risks or thrombosis and pulmonary embolism Invasive and aggressive to the patient Pain, bleeding and high degree of inflammation
Internal fixation	Immediate immobilization Can be done with limited exposure of bone to maintain vascularity and decrease infection Manages malalignment Increases periosteal blood supply	Osteotomy and adequate soft tissue coverage is required Might need bone grafting Initially destroys endosteal blood supply Not applicable to articular non-unions and malunions
Cellular and tissue based	Osteoinductive, osteogenic and osteoconductive Good callous formation ratio to progenitor cells	High cost Limited availability of tissue grafts Conflicting studies for BMP's

Table 6 - Advantages and disadvantages of therapies applied to bone fracture (Healey et al., 1990; Cain, 2002; Poitout, 2004; Einhorn, Joint and Am, 2007; Peterson and Bronzino, 2008; Kokosis et al., 2016).

2.4 Bioceramics in orthopaedics

The discovery of fire triggered society evolution and the development of processes such as clay transformation into a ceramic, for varied applications. Ceramics usage started as simple tools to improve lifestyle, e.g. pottery and furnaces. With time their application extended to the medical area, where their use includes optical lenses, diagnostic instruments, tissue culture

flasks and carriers for enzymes and anti-bodies (Jones and Hench, 2006; Kokubo, 2008). Ceramics provide advantages such as resistance to microbial attack, pH changes, solvent conditions, temperature and packing under pressure, making them suitable for a varied range of applications. Biocompatible ceramics used for biomedical applications are referred as bioceramics (Ratner *et al.*, 2004).

2.4.1 Types of bioceramics

Being applied to orthopaedics mainly, these materials can repair and restore parts of the musculo-skeletal system. They can be presented in the form of single crystals, polycrystalline, glass, glass-ceramics or composites. The most common applications for these materials are joint replacement, teeth repairing and/or replacement, and bone filling (figure 7) (Hench, 1991). A limitation for most bioceramics is their unpredictable behaviour under complex stress states, reporting slow crack growth and cyclic fatigue in many clinical applications. To improve their mechanical performance, it is necessary to increase flexural strength and strain to failure. The mechanical properties of highly studied bioceramics are listed on table 7 (Hench, 1991, 1998; Kokubo, 2008).

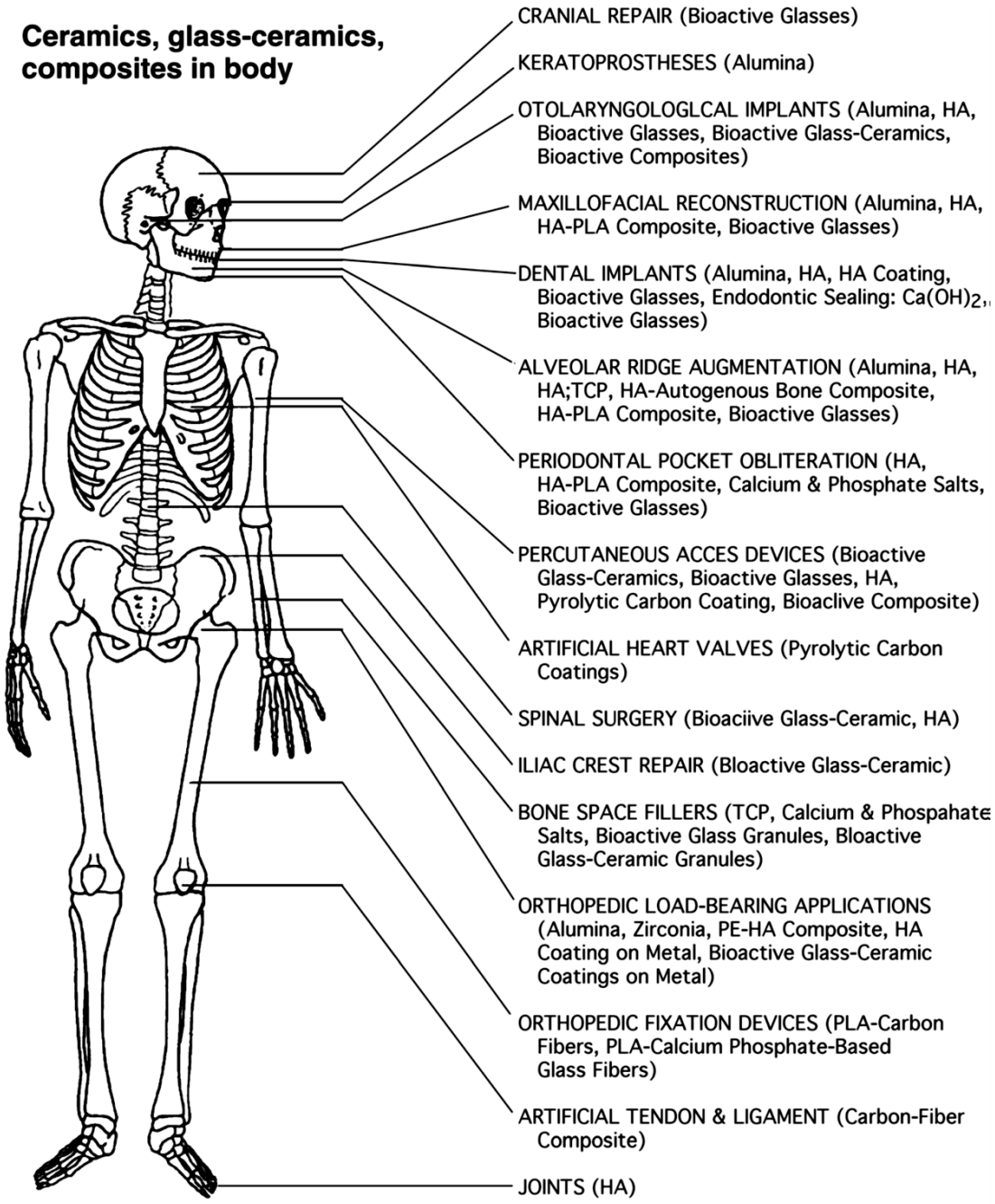

Figure 7 - Applications of bioceramics in the body (Park, 2013).

Material	Bending strength (MPa)	Compressive Strength (MPa)	Elastic Modulus (GPa)	Fracture Toughness K_{IC}(MPa $m^{1/2}$)
Natural bone **Cancellous** **Cortical**	 ---- 50-150	 2-12 100-230	 0.05-0.50 7-30	 ---- 2-12
Alumina	345	2100	300	3.50
Y-TZP	>1000	2000	200	9-10
β-TCP	140-154	460-687	33-90	----
HA	115-200	500-1000	80-110	1
Bioglass® 45S5	42 (tensile)	----	35	----
AW	220	1080	118	2

Table 7 - Mechanical properties of commercial bioactive ceramics used clinically. (Y-TZP) Yttrium stabilised tetragonal zirconia. (Christel *et al.*, 1989; Kokubo, Kim and Kawashita, 2003; Kokubo, 2008; Alharbi *et al.*, 2015).

Inert materials are used when a reaction or stimulation is not needed upon implantation. Materials such as single crystal alumina are attractive for their high density and non-porous character, ideal for morphological fixation where a press-fit of the device into the defect is needed. These implants must be produced at high standard conditions to avoid failure. When processed correctly, it has been predicted it could last 30 years under 1200 N loading. This allied to low friction coefficient makes it resistant to wear turning it into a "super tribological material", being used in orthopaedic surgery since 1971 (Kokubo, 2008; Adamovic, Ristic and Zivic, 2018). Studies on total hip arthroplasty showed a decrease of 25-30% on the ball-socket interface for alumina/UHMWPE when compared to metal/UHMWPE. For alumina-alumina, the wear was close to 0. Other materials such as zirconia (figure 8) and porcelain are used in dentistry as laminates, crowns and implants for the same reasons (Ovsianikov, Yoo and Mironov, 2018).

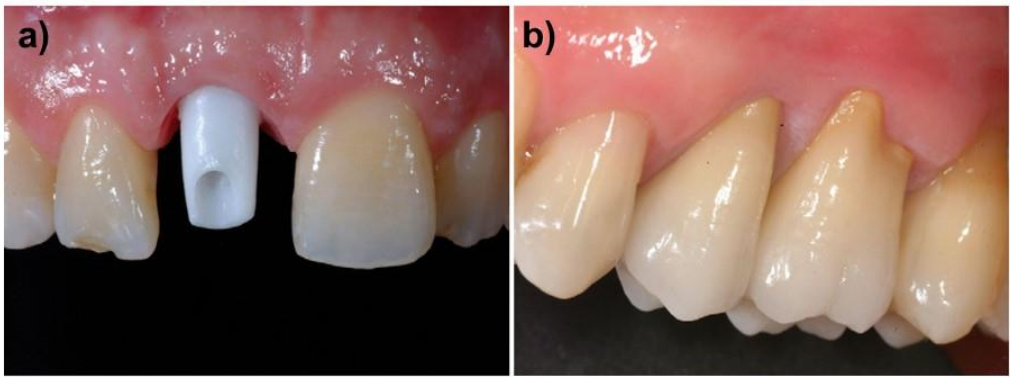

Figure 8 – a) Customized zirconia implant on front tooth (white pin). b) Intraoral view of cemented zirconia restoration (Manicone, Rossi Iommetti and Raffaelli, 2007).

Zirconia became a second-generation material, aiming to substitute alumina in hip implants, and was later introduced on knee implants. Mostly seen under the form yttria stabilized tetragonal zirconia (Y-TZP), it is superior to alumina in terms of wear resistance, fracture toughness and strength, providing more safety on the long term. Despite its high mechanical properties, fast ageing under humid environments caused the implants to fail faster. Roughening and micro cracking, due to surface degradation in contact with body fluids, lowered wear resistance (Christel *et al.*, 1989; Li, Wang and Chen, 2015). Particles of the material leach into the blood current causing a critical reaction of the immune system. The rate and dimension at which the process happens depends on how the components are processed, namely their sintering conditions (temperature and atmosphere). Saint Gobain Demarques, a french company, was considered world-leader in zirconia components for hip replacement until 2000, but a change in the manufacturing process, caused the femoral heads to fail early and in abnormal conditions, causing the removal of the product (Prozyr®) from the market in 2001 (Adamovic, Ristic and Zivic, 2018). Since then, zirconia is used in combination with alumina to improve its fracture toughness. The results showed a high resistance to cracking and crack propagation without premature ageing. This material evolved and is now commercialised under the brand Biolox® delta, by CeramTec AG. The company used nano-sized particles of Y-TZP for their ability to uniformly distribute within the alumina matrix. Addition of chromium oxide to reduce hardness and strontium oxide to prevent cracks during sintering, made this product a staple in the orthopaedic market. Used mostly for biological fixation, where the roughness of the surface or porous microstructure is key, these inert materials provide biocompatibility and excellent mechanical strength, and don't degrade (kept until failure or until the patient's death). A disadvantage is their fixation mechanism, mechanical fit. It lacks a bond with the tissue, unlike bioactive materials, and this leads to

loosening and wear of the implant resulting in failure. Adding to this, the lack of degradability prevents their use in temporary applications. These limitations shifted the focus to biodegradable and bioactive materials, i.e. CaP based ceramics, bioactive ceramics, biodegradable polymer and even biodegradable metals (Gao *et al.*, 2017).

Bioactive ceramics and CaP based ceramics are biocompatible and osteoconductive, and their bonding strength to the native tissue, when implanted, is 5-7 times higher than that of inert bioceramics. Unfortunately, these ceramics are not highly crystalline, structure wise, and their mechanical strength is lower than that of cortical bone, limiting their usage to low/non-loading areas, i.e. tooth root replacements and jaw augmentation. Source wise, mineral such as HA can be extracted from corals or animal bones (natural sources) or made in the laboratory (synthetic). It is extremely appealing for its high affinity with amino acids, protein and organic acids in the body, however it does not degrade *in vivo* (Gao *et al.*, 2017). When the hydroxyl groups in HA are substituted by fluorine ions, the materials become fluorapatite (FA), a more stable version at high temperatures and under degradation (Shareef, 2018). A degradable bioceramic is TCP, also known as whitlockite. It can be found in various forms (am-, ap-, ß – and α-), but ß-TCP is the most investigated for medical applications due to its crystalline structure. Applications include cements for small bone defects, acting as hardening agent, dental implants and filler for its surface reactivity (provider of Ca^{2+} ions and PO_4^{3-}). When spray coated into implants that were placed in dogs femora, it did not perform as well as HA, however it is still implemented in metallic prostheses (Kokubo, 2008). In a study conducted by Yuan et al. (Yuan *et al.*, 2007) TCP scaffolds containing bone marrow osteoblasts were implanted in dogs. The results showed a rapid integration with the host bone and full repair of the defect in 3 months. This was attributed to the fast degradation rate (10-20 times higher than HA), that allows for a greater availability of Ca and P ions to conduct osteoblasts and accelerate the regeneration process. An alternative to Ca-P ceramics is Calcium-Silicon (Ca-Si) ceramics such as wollastonite and diopside. These have better mechanical properties than CaP based materials and benefit from the effect of Si *in vivo*. Si is an important element in the human body and can be found in bone and in the extracellular matrix (ECM). It has an important role in bone calcification and has been reported as beneficial for bone density improvement, and in preventing osteoporosis. It promotes the production of collagen and proteoglycans and activates the expression of genes related to osteoblasts proliferation and differentiation. These features allied to their mechanical properties, make them suitable for bone repair applications (Gao *et al.*, 2017).

As demonstrated previously, bioactive ceramics (bioglasses and glass-ceramics) allow the formation of an HCA layer that improves the response of osteoblasts, and more recently of MSCs (Kokubo, 2008; Park, 2013). They are mainly composed of silicon dioxide, phosphorus pentoxide and calcium oxide, with other additions possible, depending on the application and the desired properties. Glasses are extremely versatile, and their bioactivity and mechanical properties can be tuned depending on their composition and processing. Their low toughness and insufficient strength limit their use but improvement has been attempted through the use of nanoscale second phases, and dimension reinforcement with nanoparticles (Gao *et al.*, 2017). Another option was discovered in 1982 by Kokubo et al., a bioactive glass-ceramic named AW. This material presented both bioactivity and improved mechanical properties, close to those of human cortical bone. AW containing crystalline oxyfluoroapatite ($Ca_{10}(PO_4)_6(O,F_2)$) and β-wollastonite ($CaO{\cdot}SiO_2$) in an MgO–CaO–

SiO_2 glassy matrix . The glass is obtained via melting and quenching route, but every supplier could change and tune the production method. The glass frit obtained is then milled to reduce the particle size and create the AW powder. The initial powder is amorphous, but when heated, apatite and β-wollastonite form. The amount of crystallinity can be controlled by changing the hold times for the crystal nucleation and crystal growth (Hench, 1991; Kokubo, Kim and Kawashita, 2003). AW glass ceramic applications have been intensively studied since its discovery targeting several areas of the body (e.g. hip and spine). Fujita et al. produced intramedullary plugs for total hip replacement and implanted them in 22-year-old beagle dogs. The implant consisted of porous AW rods with an average pore size of 200 μm. the scaffold performance was evaluated at different times after the implantation, and 24 months later the implant was resorbed and substituted by newly-formed bone (Fujita *et al.*, 2000).

2.4.2 Processing of bioceramics

In order to attain good results, a device should be designed accordingly to the application, and the material chosen prepared and processed in a repeatable and reliable fashion. In bone implants, shape and morphology are highly important for tissue integration, as explained previously. Porous structures are usually created using porogens, or similar additives, that are added to the initial mixture and then removed using a solvent, or by pyrolysis. Particle leaching and freeze drying are also common methods, particularly for polymer-ceramic combinations (Goudouri, Balasubramanian and Boccaccini, 2016). These techniques allow the pore formation, but the absence of control upon their shape and distribution jeopardizes

the success of the device (Khang Kim, Moon Suk, Less, Hai Bang and Ltd., 2007; Meyer Thomas *et al.*, 2009).

In ceramics processing, regardless of their nature, preparation of raw materials, forming of the green body and sintering processes are highly related, and influence each other directly. The chemical composition will dictate which process should be used, and the final properties of the part. Another approach could rely on the desired material properties according to a certain application, which will dictate what materials could be suitable and the best processing method to attain them. The same applies to the manufacturing method, because not all materials can be processed the same way, and not all processes give the same end results, for a determined material formulation (Lee, 1996).

2.4.2.1 Conventional processes of crystalline ceramics

Sintering at high temperatures is the most common route to produce a crystalline ceramic. The process starts with the powder processing, followed by the green body forming and finally the sintering to create the microstructure (Kokubo, 2008).

Powder processing

Powders can be processed using a wet or dry chemical route, according to the product being made. Particles obtained via dry route agglomerate due to the solid-state thermal reactions, which demands the use of a comminution method to decrease the particle size and homogenise the mixture. The wet route is more precise for the creation of crystalline bioceramics, controlling the process at an atomic level through the use of liquid precursors (Kokubo, 2008). Powders main characteristics include size, morphology, density, specific area, roughness, porosity, degree of agglomeration, purity and interparticular forces. Interaction forces during packing and sintering depend on geometry, roughness, nature of the surface and interparticle distance (Fatah, 2009). In a mixture, the size distribution of particles combined with shape, roughness, density, hardness and moisture content, have a great impact on the structure, the tap density and its flow properties. The tendency has moved towards fine powders, but the use of particles below 1 μm often comes associated with agglomerate formation, leading to heterogeneity of the mixture. Small particles have high surface area to volume ratio making them more reactive in a mixture and prompt to agglomerate. Agglomerates can be soft or hard depending on the type of bonding between the particles. Soft agglomerates are associated with van der Walls forces and can be broken down using

mechanical methods such as milling and pressing. Hard agglomerates are bond chemically therefore must be avoided. The presence of agglomerates in the powder lead to variation in the packing density during forming and an heterogeneous microstructure after sintering (De Campos and Ferreira, 2013). A monodisperse powder allows a greater control of the microstructure whilst a polydisperse powder doesn't. Larger grains coarsen rapidly at the expense of smaller grains, hindering densification process and promoting irregular grain size. A polydisperse mixture can increase mechanical resistance, provided the ratio between small and big particles is carefully calculated and narrow (monodisperse-like mixture) (Ganguli and Chatterjee, 1997). The particle shape can also dictate the ability of the powder to pack. Equiaxial shapes are preferred, with preference for spheres, to promote flowability, homogeneous packing and high matter diffusion. Irregular shapes may cause particle interlocking hindering the packing and therefore the sintering ability of the precursor. Differential sintering due to agglomerates or irregular particle shape, leads to different shrinking rates across the green body and development of large pores and cracks in the final part, causing its failure upon mechanical testing (Ganguli and Chatterjee, 1997).

Powders are commonly produced via wet methods, e.g. spray drying and freeze drying. Spray drying consists mainly on the breakdown of a fluid feedstock into droplets (solution, slurry, emulsion, or sol), by spraying it into a heated chamber where the droplets dry and deposit into a vessel (figure 9). The nozzle system is under pressure, promoted by a pump, which controls the droplet size. For big droplets, nozzle diameter, viscosity and surface tension of the solution, are increased. Smaller droplets are generated by decreasing the nozzle diameter and the viscosity, whilst increasing the pressure. The main steps of the spray drying process are:

1. Preparation of feedstock by proper dispersion of the agglomerates using pre-milling and dispersants;
2. Atomization of the feedstock. The solid content should be at least 75% with a particle size suitable for the nozzle (high particle size leads to nozzle clogging and too small provokes agglomeration);
3. Drying of droplets into solid agglomerates;
4. Calcination and, if necessary, sintering of the products.

This method is a large-scale, low-cost alternative to dry routes, where the solid substances are thermally bonded, and the product milled to obtain a smaller particle size. Breakage of the agglomerates is caused by the high thermal energy used to melt the raw materials. It is extremely effective for the production of fine powders, ideal for moulding (Lee, 1996; Kokubo, 2008). Similarly, freeze drying uses a wet precipitated powder that is frozen due to the air evacuation under freezing conditions. The solid solvent is then evaporated in a

chamber, via sublimation, and removed from the dried object, leaving only the particles. The powders deriving from freeze drying have high surface areas, promote high packing density and faster matter diffusion, ideal for forming and sintering (Kokubo, 2008).

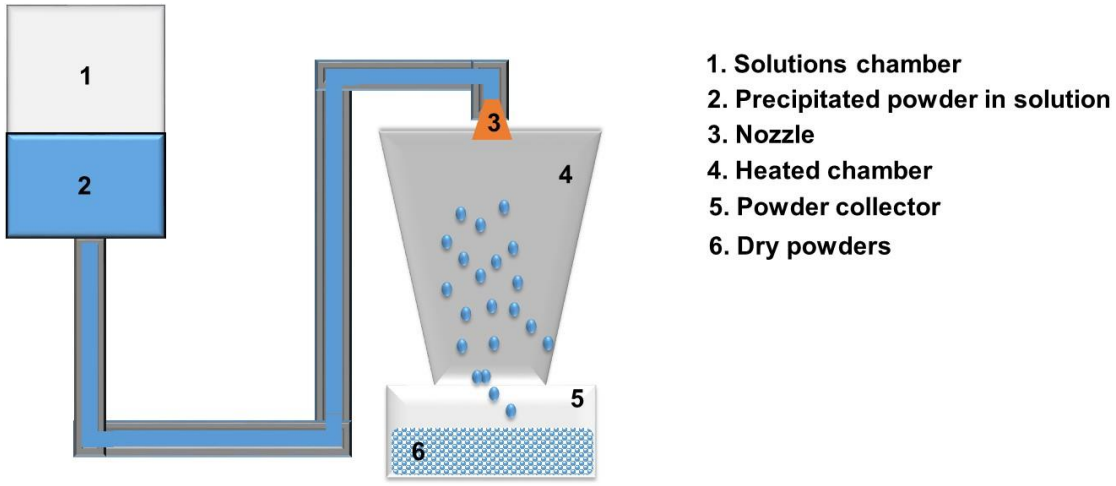

Figure 9 – Illustration of a common spray drying system, divided by components (numbered 1-6).

Powder consolidation and forming

The green body production can be achieved using either dry or wet powders with viscous fluids, via two routes: melt casting and firing of compacted powders. On melt cast, the raw powders are molten together and then formed using casting, rolling, pressing, blowing and spinning. This route is not appropriate for ceramics with high melting points or that decompose after melting, therefore is mainly used for glasses. For crystalline ceramics, firing of compacted powders is the ideal route. This method consists on the consolidation of dry powders followed by their shaping using a mould to produce the green body. The green body is then fired to densify. Polymers such as polyvinyl alcohol and paraffin are added as glues to increase the plasticity of the green body, to form it into the desired shape (Kokubo, 2008). A mould is created, and the mixture poured in, followed by cold isostatic pressing in Argon atmosphere, preventing the accumulation of internal stresses caused by air bubbles or excess of water in the part. Common forming methods are uniaxial compaction, slip casting and injection moulding. The process used dictates the additives that will be present in the mixture, e.g. uniaxial compaction uses water-soluble resins such as poly vinyl alcohol (PVA) in a 3-5wt%. Slip casting applies sodium alginates in a 0.5-3 wt%, whilst injection moulding relies on thermoplastic resins and paraffin, in a 10-25 wt%, or plasticizers such as phthalate esters in a 0.5 to 5 wt% solvent. The demoulding process is usually easy due to shrinkage of the part

after water evaporation and densification, but to prevent problems upon part removal, olive oil or silicone are added as lubricants (Kokubo, 2008).

Sintering and densification

Sintering is the stage where the microstructure is created, a main step to attain the desired final properties. The part is heated to 50-75% of the melting temperatures to promote matter diffusion between particles, joining them and reducing porosity. In the solid state the matter exchange occurs via atomic diffusion, denominated solid state sintering (Lee, 1996). The main goal of sintering is to reduce surface energy for particles to bond. This physical bonding can happen via diffusion, where the matter is transported from inside the grains into the pores, or via coarsening, the rearrangement of matter between different parts of the pore surface. Both methods lead to densification and depend highly on particle size and shape (figure 10). The result is a defined microstructure composed by grains that are separated by a grain boundary. Depending on the predominant mechanism the part density varies, being diffusion the best route to attain full densification. Coarsening tends to promote the formation of highly porous parts, with weak mechanical properties (Lee, 1996).

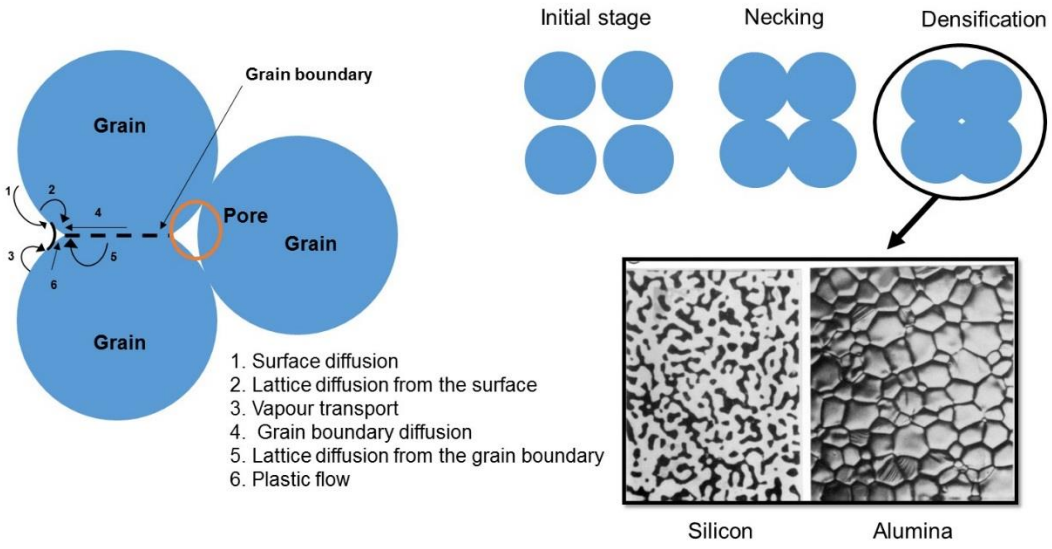

Figure 10 - Sintering mechanism and matter transport systems. When temperature increases, matter starts diffusing binding particles and decreasing porosity, necking and densification, e.g. sintered silicon and alumina (Lee, 1996).

To control densification, several factors must be kept stable: temperature, particle size, pressure and atmosphere. High densities are easily achieved using fine powders and spherical

particles for the reasons discussed on the powder processing section. Hering (Lee, 1996) states that small particles require less time to sinter, according to the relation:

$$\frac{t_1}{t_2} = \left(\frac{r_1}{r_2}\right)^n \quad Equation\ (2)$$

In equation 2, *n* varies according to the diffusion type, 3 for lattice diffusion and 4 for grain boundary diffusion. This applies to a constant temperature and spherical particles with radius *r*, with a hexagonal or cubic close packing. The required amount of time needed to sinter the part is represented by *t*. This relation predicts that a decrease on particle size from 1 μm to 0.01 μm will accelerate the sintering from 10^6 to 10^8 factors. Another valid point to be accounted for is that smaller particles are more reactive therefore tend to agglomerate if not handled with caution. To prevent it, the surface area must be measured or calculated using equation 3:

$$S_A = 4\pi a^2 N = \frac{3V_m}{a} \quad Equation\ (3)$$

In this equation *N* is the number of particles in the mixture, *a* is the radius and V_m the molar volume. This directly influences the surface free energy (*E*) as represented on equation 4:

$$E_s = \frac{3\gamma_s V_m}{a} \quad Equation\ (4)$$

The specific surface energy per surface area (γ_s) is multiplied by the molar volume and the result divided by the particle radius. This represents the decrease in surface free energy of the system when densification occurs. Since the particles surface area is also smaller due to their bonding to other particles, the driving force for sintering is the reduction of the surface energy via consolidation of the mass of particles (Lee, 1996).

The problem of coarsening prevails on solid state sintering, but it is reduced on liquid phase sintering (figure 11). In this process, an additive with lower melting point is used to create a liquid phase that infiltrates between grains, prompting diffusion mechanisms. Consequently, an increased transport of matter to the pores occurs. Liquid phase sintering is very effective on ceramics with high degree of covalent bonding because they are harder to densify using solid state. It is also used to reduce costs of solid-state sintering, when temperatures for melting are too high, causing a high expenditure of energy. The amount of liquid phase shouldn't exceed 30 vol%, a value applied solely to traditional ceramics. The most common

additives are silicates that remain as a glassy phase after cooling, providing the material with a glassy appearance which is the base of their designation as vitrified ceramics (Lee, 1996).

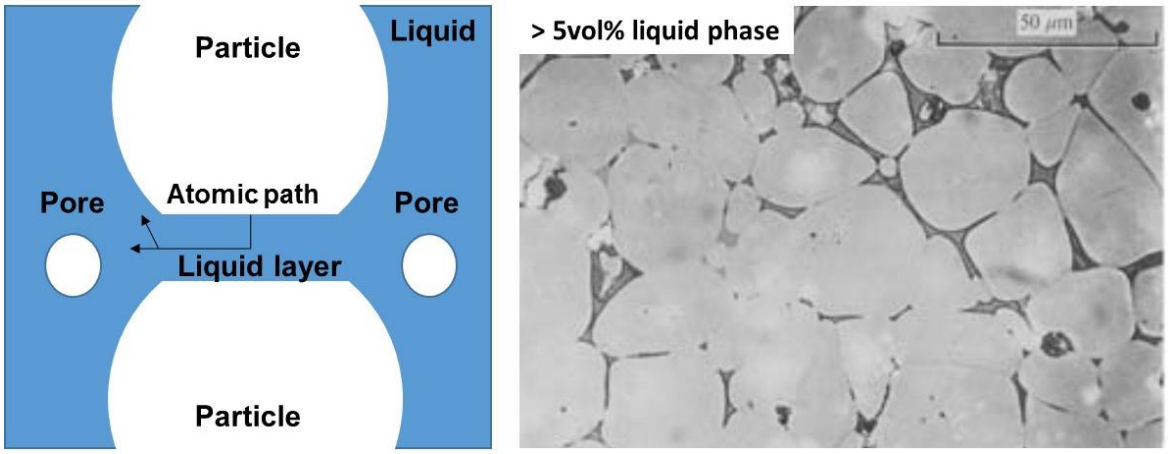

Figure 11 - Liquid sintering mechanism and example of resulting microstructure using over 5vol% of liquid phase (Lee, 1996).

In theory, liquid sintering's driving force is based on Young Laplace equation (equation 5) which assumes that the pressure in the liquid is lower than in the pore, generating capillary stress on the particles.

$$\Delta p = -\frac{2\gamma_{lv}}{r} \quad Equation\ (5)$$

In this equation, *r* represents the radius of the pore in a liquid and γ_{lv} the specific surface energy of the liquid-vapour interface. When dividing that energy for the pore radius, the pressure difference (Δp) across the curved surface is given. That stress is equivalent to submitting the system to hydrostatic pressure. The increased compressive capillary stress, generated by the liquid infiltrating the pores, reduces friction and aids particle rearrangement. This results in enhanced densification, faster grain growth and occasionally the production of a specific grain boundary (Lee, 1996). In most cases the liquid phase remains in a glassy state as mentioned before. In some specific cases this phase might be incorporated in the solid solution, crystallize or evaporate, commonly known as a transient liquid phase. For evaporation, the liquid phase disappears during sintering. Despite the aid in densification of the part, by itself this measure is not enough to attain full density. Parameters that were previously mentioned such as powder particle size and morphology and presence of pressure and controlled atmosphere are still paramount (Lee, 1996).

2.4.2.2 Conventional processes: glasses and glass-ceramics

Bioactive glasses commonly arise from melting metal oxides, carbonates and fluorides together, resulting in a composition based on silicates (SiO_2), phosphate pentoxide (P_2O_5), alkaline (Na_2O, K_2O) and non-alkaline earth oxides (CaO, MgO). Structurally, the silicates and phosphates form a network that composes the skeleton of the glass and strengthens it. The alkaline and non-alkaline earth oxides break it, allowing the formation of spaces where the oxides can bond. The addition of oxides, also called modifiers, lowers the melting point, changes the refractive index, the viscosity of the melt, the density of the material and the glass transition temperature (T_g). Nonetheless, these oxides are essential for bioactivity (Kokubo, 2008). Glasses are amorphous solids obtained by the melt cast route, also known as melting and quenching. The melt is cooled from a liquid state becoming rigid, without specific volume changes. According to the American Society for Testing and Materials (ASTM) glass is *"an inorganic product of fusion, which has been cooled to a rigid condition without crystallization".* Another 2 common routes are water evaporation from a solution containing the glass elements, and the use of organic materials as precursors (e.g. Pexiglas®). If enough energy is provided for a long period of time, the glass state changes into crystalline state, with a rate of crystallization determined by equation 6, where H_f is the heat of fusion at the melting temperature, *a* is the lattice spacing, and η the viscosity of the liquid (Park, 2013).

$$v = \frac{H_f(T_m - T)}{3\pi a^2 \eta T_m} \quad Equation\ (6)$$

This equation states the influence of viscosity in the speed of crystallization, high viscosity at T_m promotes the formation of glass and slows down the crystallization rate (Park, 2013). This relation is presented in figure 12, where the result is dependent on the temperature influence on the volume and cooling rates. According to this, if the melt is cooled rapidly, then crystallisation is avoided, however if temperature is kept at the melting point, the high energy in the system allows the ions to rearrange and form small crystals. The glass must also be annealed at a temperature lower than the T_g to eliminate the residual stresses originated through the fast cooling and contraction of the structure. Crystalline glasses present a crystallisation temperature (T_c), which is located between the T_g and the T_m. By lowering the temperature at a slow rate, the nucleated crystals start growing giving origin to a glass-ceramic.

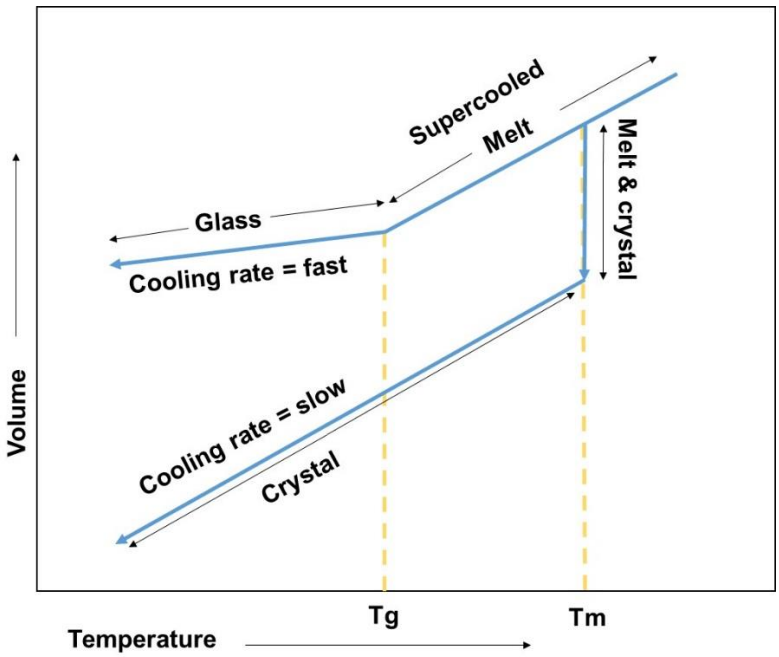

Figure 12 - Volume changes depending on the melt transitions (Kokubo, 2008).

Glass-ceramics are primarily formed by annealing the glass at a temperature above the T_c, generating a fine microstructure where each grain has an average diameter of approximately1 µm, the key to their improved mechanical properties (Kokubo, 2008). To estimate the crystallisation tendency of the glass, several parameters can be calculated based on the thermal transitions: crystallisation tendency (δ), glass forming ability (K_{gl}), and sinterability (S_c), represented on equation 7, 8 and 9 (Hrubý, 1972; Lara *et al.*, 2004). According to Hruby, the smaller the δ, the highest is the probability of the glass having structural units with high crystallisation tendency, i.e. with high liquidus temperature of the melt which is unfavourable for glass formation. For glass forming ability, if values are below 0.1, the glass formation is difficult and extreme control of conditions must be applied. For values equal to or close to 0.5, glass is easily prepared by free cooling of the melt in air. S_c in the context presented by Lara et al., refers to the competition between sintering and crystallisation kinetics during heating. The higher is the sinterability, more independent are the processes. High S_c values are related to better sintering behaviour and higher densification of the final sample (Hrubý, 1972; Lara *et al.*, 2004).

$$\delta = T_c - T_g \qquad Equation\ (7)$$

$$K_{gl} = \frac{\delta}{T_m - T_c} \qquad Equation\ (8)$$

$$S_c = T_c - T_{MS} \qquad Equation\ (9)$$

In the represented equations, T_c refers to the temperature at which crystallisation is initiated, T_g the glass transition temperature, T_m the melting temperature and T_{MS} the temperature of maximum shrinkage.

In the medical field, the first glass-ceramic developed was AW where apatite grains crystallized in a strong wollastonite matrix, via surface crystallization, the reason why it must be processed using sintering. AW processing is based on the melting of metal oxides, carbonates and fluorides with the addition of modifiers to produce specific changes (Kokubo, 2008). Tuning of the glass-ceramic properties allows for higher freedom regarding the application. The smallest of changes (below 2 wt% in glass composition) can affect parameters such as the bioactivity and degradation rate (Abou Neel *et al.*, 2009; Murphy *et al.*, 2009; Miola *et al.*, 2014). Within the medical field, such changes can dictate whether the material will be used for a temporary or permanent solution. Researchers such as Filho et al. (Filho, La Torre and Hench, 1996; Massera *et al.*, 2015) demonstrated how the increase in crystallization can retard the development of the carbonated apatite layer. Introduction of oxides is often done on purpose to easy the processing of the material. In some cases, they result from the processing of the material itself, being a common one alumina, originating from the glass frit milling. This oxide acts as stabilizer and has been used in many applications to control the microstructure during the sintering process of glasses and other polycrystalline ceramics (Baino *et al.*, 2016). AW can resist failure by fatigue under a constant loading of 65 MPa, stronger compared to sintered HA which sustained the same loading for only 1 minute. In the study developed by Kokubo et al. was estimated that AW can prevail for 10 years when submitted to those loading conditions, immersed in SBF (Duminis, Shahid and Hill, 2017). Bioactive materials are also in study as reinforcement of polymer and metallic matrices of biocomposites once they can induce the precipitation of an HCA layer and improve the fixation of biodegradable polymeric implants, whilst enhancing osteoconductivity (Navarro *et al.*, 2008).

2.5 Biocomposites in orthopaedics

A composite consists of two or more different materials, separated by an interface, at the micro or macro scale. Briefly, a composite consists of a continuous phase (matrix), reinforced by one or more discontinuous phases (filler). The composite is usually designed according to the final properties of the device, demanding a fine balance between material ratio/weight percentage (wt%). The choosing of the appropriate processing technique is also key to obtain the desired orientation and distribution of filler. In terms of reinforcement, a composite can be

classified as a particulate, fibre or laminate composite. Particle can be spherical, cubic, tetragonal or with random shape, e.g. crushed glass. Fibres can be long or short in terms of size, unidirectional or random in terms of orientation. Laminates are produced by stacking oriented fibre composite laminae to form a structural element (Ratner *et al.*, 2004). An important aspect is the relationship between matrix and reinforcement/s, whether they work separately or synergistically. A common goal is achievement of high mechanical properties such as stiffness, strength, toughness and fatigue resistance. Fibres are a preferred reinforcement for these applications because their strength can be tuned by changing fibre orientation and wt%. Some of these composites reach stiffness and strength values similar, or higher, than those of metals (Ratner *et al.*, 2004). Particulates are isotropic therefore not as useful for improvement of mechanical properties. They can be used to induce a chemical reaction, increase degradation or even to attract a certain type of organism/cells (Navarro *et al.*, 2008; Ahmed *et al.*, 2011).

2.5.1 Types of biocomposites

Composites have been introduced for clinical application for their ability to mimic the hierarchical structure of human tissues. The combination of two different materials with desired properties is a main advantage, namely for load bearing applications, eliminating problems such as stress shielding and post-implantation fractures, common in metals. The use of degradable matrices reinforced by stronger materials is seen as a viable solution for the problem. Balancing the materials ratios allows the control of the degradation rate and consequently of the mechanical strength (Shikinami and Okuno, 1999; Agarwal, Broutman and Chandrashekhara, 2006; Ahmed *et al.*, 2011). In medicine, most matrices are made of biodegradable polymers due to their physicochemical properties, and successful use in clinical applications. Materials such as PLA, Poly (glycolic acid) (PGA), polycaprolactone (PCL) and Polyhydroxybutyrate are considered perfect candidates to process biocomposites for bone and ligament repair. They have also been combined with bioactive molecules and particles to promote cell guidance and/or stimulation towards a response (Navarro *et al.*, 2008). Studies on their ability to improve osteoconductivity had positive results. Composite scaffolds made of PLLA and HA, or poly(lactic-co-glycolic acid) (PLGA) and HA, demonstrated improved mechanical properties, osteoconductivity and bone formation (Zhang and Ma, 1998). Another study performed by Ma et al. showed the positive effects of adding HA, on the osteoblastic cell seeding uniformity, and a significantly enhanced expression of mature bone marker genes such as osteocalcin, compared to PLLA scaffolds (Ma *et al.*, 2000).

2.5.1.1 Biocomposites for bone regeneration

Biocompatibility and biodegradability are important when processing a scaffold for tissue regeneration. A wide range of materials can be used to attain these properties, however the technique to process them must be adequate. Several processing techniques have been used to produce 3-D scaffolds, from particle-leaching to solvent casting. New techniques such as fibre bonding, membrane lamination and gas saturation are amongst the most common, and recently, 3D- braiding to make scaffolds for ligament replacement (Laurencin and Freeman, 2005; Navarro *et al.*, 2008). The production of biocomposites can be challenging and should mirror the target tissue. Bone is a composite by nature, apatite reinforced with collagen, with different types of structures at the micro and macro-scale. A bioactive ceramic-polymer composite has potential to mimic this. Using a polymer with mechanical properties within the range of bone, e.g. PLLA, guarantees the device will withstand the loads, be ductile, and by being biodegradable, to disappear once the bone tissue is fully regenerated. The addition of a bioactive material such as HA and AW, promotes the tissue growth adjacent to the implant, whilst enhancing the proliferation of osteoblasts, and the differentiation of MSCs (Wang, Kukobo and Bonfield, 1996; Wang, 2003).

2.5.1.2 Biocomposites for fracture fixation

In fracture fixation, Ti plates are the gold standard device but problems such as stress shielding, and re-fracturing are highly associated with these devices. Other disadvantages include plate migration and, in the case of maxillofacial fractures, a potential interference with facial growth and thermal sensitivity (Suuronen, 1993; Giannoudis, Psarakis and Kontakis, 2007). To counter these problems, research on biodegradable devices as taken place, with the most common being associated to PLLA due to its low cost and suitable mechanical properties. PLLA plates and screws are broadly studied, with interesting works developed by Bos et al. for zygomatic fractures and Suuronen et al. on PLA and PGA, for mandible and orbital fractures (Bos *et al.*, 1987; Suuronen, 1993). Commercially, products such as the OSTEOTRANSMX (Takiron CO, Ltd, Osaka, Japan) are in the market. This device is composed of PLLA and HA which makes it bioactive and completely resorbable (Sukegawa *et al.*, 2016). Fibre reinforced composites made of a PLA matrix and iron doped phosphate glass fibres (PGF) are reported in literature for internal fixation purposes. These had varying amounts of reinforcement (30-40 wt%), that could be under the form of a random mat or

unidirectional-oriented (Ahmed *et al.*, 2011). At 5 wt%, PLLA/Ca-doped short phosphate glass fibres composites proved to stimulate biomineralization of hMSCs (Melo *et al.*, 2019).

2.5.2 Processing of biocomposites

The processing of non-porous bioactive polymer-ceramic composites for tissue replacement is well known. Avoiding contamination is imperative since it can lead to leaching of toxic substances upon implantation and/or when the device starts degrading (biodegradable biocomposites) (Wang, 2003). Two routes currently exist either based on physicochemical methods or on thermo-mechanical methods. The first route includes precipitation of mineral crystals *in situ* in the polymer matrix (CaP reinforced with collagen) (Clarke *et al.*, 1993) and, dispersion of bioceramic particles/fibres in the polymer solution (HA/Chitin) composites (Wang, Weng and Poret, 2001), with subsequent consolidation. The second route, based on thermal and mechanical mechanisms, allows the impregnation of porous bioceramic matrix with a polymer. This method is useful for the manufacturing of biodegradable composites and/or incorporation of bioceramic particles/fibres into a polymer matrix, via conventional plastic processing technologies, including hydrostatic extrusion (Ladizesky, Ward and Bonfield, 1997; Wang, 2003). In industry it allows the process of composites with enhanced mechanical performance, via compounding, milling, compression and injection moulding. Different geometries and homogeneous distribution of the reinforcement can be obtained by using a compounding extruder, internal mixer or a two-roll mill (Wang, Porter and Bonfield, 1994; Wang, L Hench and Bonfield, 1999).

2.6 Additive manufacturing

To overcome the problems of traditional manufacturing, new processing techniques, such as AM, with the ability to generate complex shapes with high porosity, at various scales, have been developed (Yasa and Ersoy, 2018). Personalisation attracted the attention of professionals in the bone RM area, and has been the hype of orthopaedic research (Butscher *et al.*, 2012; Morris *et al.*, 2016). Another advantage of AM is its growing market, already published on Wohlers report of 2018, which states an industry continuous growth of 21%, lower than in 2015 (25.9%) (Caffrey, Campbell and Wholers, 2016; Wohlers *et al.*, 2018) which is still translated into USD$ 7 billion. A rise is predicted for 2025 due to the demand from industries such as automotive, dental, manufacturing and healthcare (Caffrey, Campbell and Wholers, 2016).

In AM, the parts are produced in a layer by layer fashion, using a computer aided design (CAD) model that is converted into an STL file. The information can come from a scanning method, such as CT and magnetic resonance imaging (MRI), designed by the researcher, or a combination of both. Depending on the material and application, different AM processes can be applied. Both liquid or solid-state materials are accepted, i.e. thermoplastic polymers that are molten to a viscous state, resins that are cured using light, solid bulks that are deformed using mechanical energy, and powders that are shaped using binders or laser. A general overview of the techniques is demonstrated in table 8, according to ASTM F42 (Gibson, Rosen and Stucker, 2010).

AM process	Example technique
Vat photopolymerazation	**SLA** A liquid photopolymer is contained un a vat and processed by selectively delivering energy to cure specific regions of a part cross-section
Powder bed fusion	**SLS and SLM** A container filled with powder that is processed selectively using an energy source, most commonly a scanning laser or electron beam
Material extrusion	**FDM** Processes that deposit a material by extruding it through a nozzle, typically while scanning the nozzle in a pattern that produces a part cross-section
Material jetting	**Ink jetting** Droplets of material are selectively deposit onto a platform and cured using an energy source
Binder jetting	**3DP** A binder is printed into a powder bed in order to form part cross-sections
Sheet lamination	**LOM** Processes that deposit a layer of material at a time, where the material is in sheet form
Direct energy deposition	**EBM** Processes that simultaneously deposit a material (usually powder or wire) and provide energy to process that material through a single deposition device

Table 8 - AM processes according to ASTM F42, and some examples of used techniques (Wong and Hernandez, 2012).

Liquid-based processes include Fused Deposition Modelling (FDM) or Fused Filament Fabrication (FFF), where the materials used are generally thermoplastic polymers such as acrylonitrile butadiene styrene (ABS) and PLA. The second process is Stereolithography (SLA) which uses acrylate or epoxy resins that contain monomers and photoinitators that are activated by ultra-violet (UV) light. They act as catalysts for the polymerization reaction, allowing the material to solidify. A third process, is ink jetting, similar to SLA, except that liquid inks are created using either polymers (urethane acrylates and methacrylate resins), metals (bismuth, led and thin alloys), or ceramics (zirconia and alumina), with a viscosity range between 20-40 cP, at printing temperature (Gibson, Rosen and Stucker, 2010; Wong and Hernandez, 2012).

Solid-based material processes can use either bulk forms or powder, depending on the material and the application. On Laminated Object Manufacturing (LOM) sheets of metal, plastic, ceramics or paper, are joined through the application of heat and pressure. Powder based processes provide better resolutions and do not require the application of supports, or post processing in most cases, once the powder bed acts as the support itself, and the high resolutions permit a higher level of accuracy and surface smoothness. In powder bed methods, the material can be molten, sintered or bound using a liquid binder. Processes using melting include Selective Laser Melting (SLM) and Selective Laser Sintering (SLS). SLM is used only for metals and metal-ceramic composites, commonly aluminium (Al) and Ti alloys, stainless steel and other tool steels, nickel-based alloys and cobalt-chrome. Some companies provide precious metals such as silver and gold. SLS materials range from thermoplastic polymers, usually polyamide 12, PLA or even PCL, to ceramics such as HA and AW (Lorrison, Dalgarno and Wood, 2005; Williams *et al.*, 2005; Lee *et al.*, 2015). Finally, Binder Jetting uses polymers such as PMMA, gypsum, and starch-based materials. For ceramics sintering must be used to finish the part. The binder varies but is commonly water based. Ceramics aside, most parts are infiltrated with glues and other types of adhesives provided by material and equipment suppliers, to attain structural integrity. Special cases such as Electron Beam Manufacturing (EBM) and Laser Engineered Net Shaping (LENS) can process both metals and ceramics, using wire or powder forms as feedstock. In this case a melt pool is created, and powder is deposited onto it, solidifying once the laser moves away from the melt. The wire form is used mainly for simple geometries, coatings or when thin to thick transitions are required (Lorrison, Dalgarno and Wood, 2005; Williams *et al.*, 2005; Gibson, Rosen and Stucker, 2010; Wong and Hernandez, 2012; Butscher *et al.*, 2013; Lee *et al.*, 2015; Mancuso *et al.*, 2017).

Within the medical area, AM has been widely studied for production of devices targeting tissue regeneration. Printing of biocompatible and biodegradable materials, both natural and synthetic, is evolving, with study numbers growing by the year (Sachlos and Czernuszka, 2003). Binder Jetting is a frequently used technique as previously assessed. Early on 1998, Kim et al. had printed chloroform onto a PLGA powder bed to create 3D scaffolds for liver TE. These comprised channels with a diameter of 800 µm with microporosity created by sodium chloride leaching from the PLGA powder. Despite the desirable microstructural features, the use of organic binders demanded an exhaustive procedure for solvent cleanse and evaporation (Kim *et al.*, 1998). Lam et al. used water as binder for starch base scaffolds. The scaffolds were free of toxins, but hadn't the mechanical stability needed, leading to their infiltration with PLLA and PCL solutions in methylene chloride (Lam *et al.*, 2002).

2.6.1 AM of ceramics for bone repair devices

AM of ceramics in literature consist mainly of a multi-step process involving the use of sacrificial binders and powder particles, e.g. binder jetting where the binder is removed inside the furnace during a "de-binding" stage. SLM and Direct Energy deposition (DED) are the only routes reported with the ability to process ceramics in a single step. The AM processes used to obtain ceramic parts are presented on table 9 alongside the feedstock form, advantages and disadvantages of each route (Deckers, Vleugels and Kruth, 2014).

Single-step methods are also limited in terms of materials used since these cannot include cells and the nozzle limits the features size. Some geometries might need supports in the case of DED, and for SLM and SLS, trapped powder can be a problem as in SLS. SLA provides high resolutions and accuracy as well as repeatability but is limited in terms of materials that can be used. HA suspended in photocurable monomers was processed by SLA to produce orbital floors and other craniofacial devices (Sachlos and Czernuszka, 2003). Despite the success it is known that the use of cells with the resins is also limited once most of the resins are toxic. SLS allows for the use of cells once the materials can be biocompatible, however the range is limited to some bioceramics such as CaPs. For load bearing applications in bone tissue, HA and CaPs are not suitable. Lee et al. used SLS to produce personalized AW scaffolds which incorporated a cylindrical central channel. This design was chosen to increase cell penetration and medium flow, guaranteeing nutrient delivery to the cells in the centre of the structure. The *in vivo* results report osteoid formation and tissue in-growth. Also AW scaffolds do not require osteogenic pre-induction, highlighting their aptitude for custom-designed bone replacements (Vlasea *et al.*, 2010; Lee *et al.*, 2015).

Steps	Process	Feedstock form	Advantages	Disadvantages
Single step	SLM	Powder	Do not require binder removal step Limited options of processes	Not able to process many ceramics at the moment Thermal cracks arise from the rapid cooling (might be prevented by preheating the powder before irradiation) Deposit of dry powder agglomerates of 10 – 100µm generally lead to low-density ceramics
	DED	Powder		
Multi-step	LOM	Green ceramic tape-cast layers	Able to produce different types of ceramics Colloidal based processes attain higher densifications and better surface quality (e.g. SLA) Slurry based systems also produce crack and pore free structures	Require time-consuming binder removal step Thermal cracks might form if the process steps is not well controlled (especially the binder burnout step) Deposit of dry powder agglomerates of 10 – 100µm generally leads to low-density ceramics Poor surface quality in some processes
	Slurry based	Slurry		
	3DP	Powder + sacrificial binder (optional)		
	SLS	Powder + sacrificial binder		
	SLA	Powder suspension		
	Direct inkjet	Suspension containing ceramic		
	Aerosol jet printing	Suspension of droplets containing fine ceramic particles		
	FDM	Ceramic particles dispersed into a thermoplastic or wax filament		

Table 9 - Processing of ceramics using AM (Deckers, Vleugels and Kruth, 2014).

Binder jetting theoretically allows the use of any powder and corresponding binder. The powder bed acts as a reagent and support simultaneously, resulting in decreasing of material costs and increasing of design possibilities. When applied to ceramics (figure 13) it can include a sacrificial solid binder, added to the powder bed, to increases interparticular contact, enhancing green part density. Later, during sintering, it promotes material diffusion resulting in high densities and improved mechanical properties. A burnout stage allows for controlled

binder removal, avoiding part distortion via swelling or excessive shrinkage (Lee, 1996; Dyson *et al.*, 2007; Rodrigues, 2018). Despite the lower resolutions, compared to other powder bed methods, and the lack of control over porosity, binder jetting is material versatile, if it is post-processed accordingly. Trapped materials are easily removed once the particles aren't strongly bound prior to sintering.

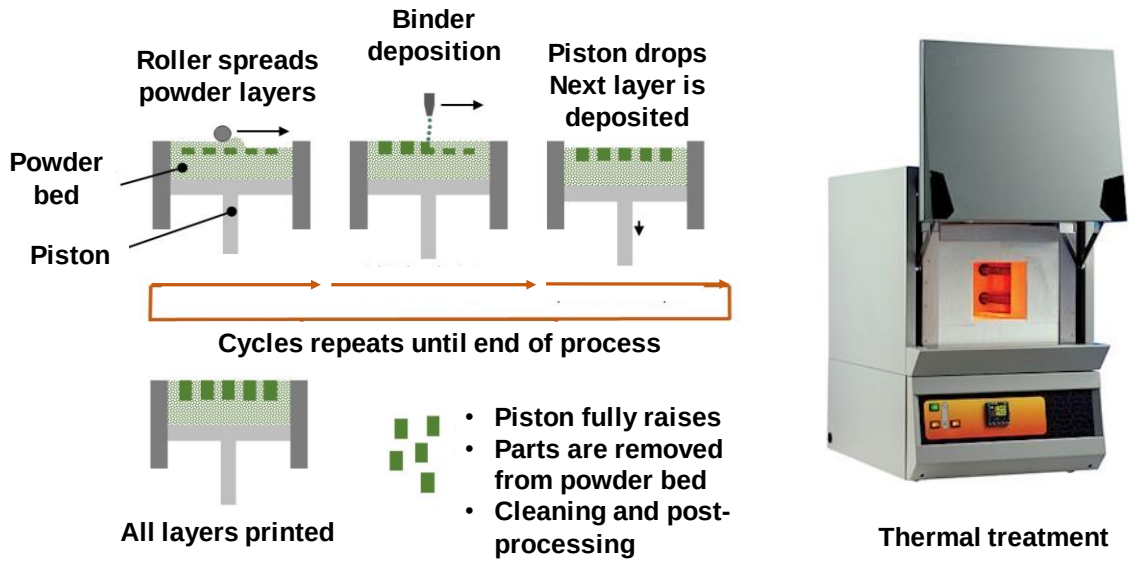

Figure 13 – Left: Binder jetting printing process. A roller spreads a layer of powder onto the powder bed and an inkjet head selectively deposits the binder. The platform lowers down, and another layer is spread. The process continues until the part is finished. The part is then cleaned and sintered to attain structural integrity (Gibson, Rosen and Stucker, 2010). Right: Sintering furnace.

2.6.1.1 Binder jetting of bioactive glasses and glass-ceramics

Bone is heterogeneously porous, which suggests use of a technique that could create this type of microstructure, ideally without the use of any additives. Binder jetting offers such a technique and could be ideal to fabricate personalised bone implants. As mentioned in section 2.4, the most commonly processed bioceramics are HA and TCP. These materials have been used under powder form as feedstock for binder jetting, alone and in combination with polymers or other ceramics (Lv *et al.*, 2019). HA in both nanoscale and microsphere form (Suwanprateeb *et al.*, 2009; Lv *et al.*, 2019) has proved its suitability to create bone scaffolds using binder jetting, however with lower mechanical properties, compared to cortical bone. NanoHA scaffold, sintered at 1250 ˚C and a porosity of 58%, reached a compressive strength of 84 MPa. In this study it was also observed that higher binder saturation allowed for better mechanical properties. This relation between binder and mechanical performance was also observed by Szucs et al. (Szucs and Brabazon, 2009) when printing TCP precursor powders.

Here the binder acted as a ligand and wet chemical reagent, promoting the reaction between dicalcium phosphate anhydrous and calcium hydroxide to obtain TCP. An alternative to a reaction process, using resins as binders can improve both flexural strength and modulus whilst improving strain at break (Suwanprateeb, Sanngam and Suwanpreuk, 2008). The morphology of the powder bed is important, meaning the powder preparation must be adequate. Studies comparing milling with spray drying of HA powders showed that milling is more advantageous since it leads to better mechanical properties (Suwanprateeb, Sanngam and Panyathanmaporn, 2010). Spray dried powders benefited tap density however milling promotes packing and therefore increases green density. This leads to a higher level of interaction during sintering, through inter and intra particle forces, consequently to a stronger part. Another strategy to improve the mechanical properties involves doping the powders, to induce a reaction during sintering. TCP powders doped with SiO_2 and ZnO produced scaffolds with better mechanical properties and enhanced cell proliferation, compared to TCP only (Fielding, Bandyopadhyay and Bose, 2012).

The versatility of the binder jetting process is not limited to the raw materials (binder and powders) but also to the printing parameters. HA parts produced with a layer thickness of 0.10 mm proved to yield better flexural strength and modulus, compared to those printed with layers of 0.08 mm and 0.20 mm (Suwanprateeb *et al.*, 2012). In considering load bearing applications, the processing technique can be applied to glass-ceramics such as AW (Vlasea *et al.*, 2010; Alharbi, 2016; Mancuso *et al.*, 2017). Binder jetting of bioactive ceramics, specifically Bioglass formulations and AW, both blended with MD, was extensively studied and experimented by Mancuso et al. (Mancuso *et al.*, 2017) with values obtained for the printed implants matching previous studies, with minimum variation. The use of binder jetting permitted the production of strong accurate structures, at lower cost. Examples of printed AW implants and their microstructure, compared to bone, can be seen in figure 14. This work aimed to test the printing of different shapes using different powder blends to assess the process capabilities.

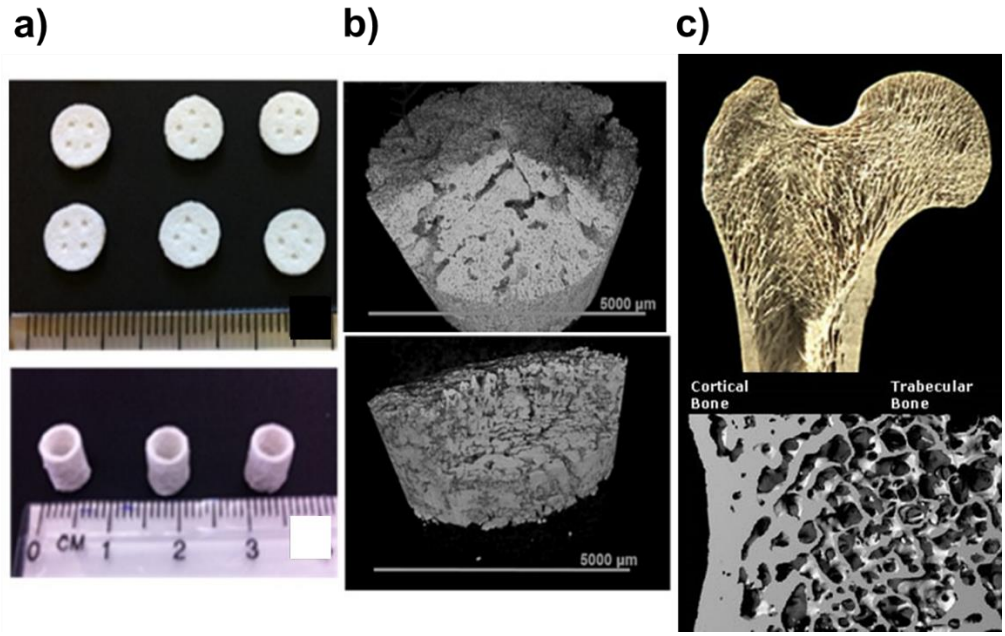

Figure 14 – a) AW implants processed via 3DP. b) Microstructure of the printed parts obtained via µCT, c) compared to bone (Mancuso *et al.*, 2017).

2.6.1.2 Important parameters binder jetting

Binder jetting uses powders as feedstock and sintering as post processing. When using powders, it is key to control the particle size, shape and size distribution, in order to obtain uniform layers, a faster sintering, and stronger part. The powder size and morphology directly affect the flowability and wettability of the material. This influences the layers homogeneity, binder concentration and distribution. When establishing printing parameters, it is also important to define the values for the binder to volume ratio of the inner core and shell. These relate to the amount of binder deposited on the outer edges and surfaces of the part (shell) and in its interior (inner core) (Alharbi, 2016). The parameters and respective effects are described below:

1. Powder packing: spherical particles, or equiaxial shapes, benefit packing uniformity. An increase in surface roughness, shape irregularity and aspect ratio, promotes packing density. In a powder mixture, packing density can be improved by upgrading the size ratio between the 2 powders, according to their composition (fraction of large to small particles). A polydisperse powder blend benefits packing density leading to an increment on green body strength (Ganguli and Chatterjee, 1997).

2. Flowability (described as the powder deformation, in movement, when submitted to external forces): an alteration in the powders state of balance occurs causing the powder to move in order to find a new balance, each particle moves freely, sliding on

top of the other. This is considered a “free flow” (like a viscous liquid). Cohesive powders might have the appearance of conventional powders but once the flow starts, it is possible to see the slip between agglomerates (Fatah, 2009). Flowability in AM dictates the powder bed homogeneity and content uniformity (De Campos and Ferreira, 2013). It is measured by the flowability factor (ffc - ratio between consolidation stress and compression strength) and by both size and particle shape. Rough surfaces have a significant effect on the adhesion force and changing the roughness can change the Van der Waals interaction by up to several orders of magnitude. Mohammed et al. observed that irregularities in particle shape cause considerable interlocking amongst the particles and increases their resistance to flow. Their roundness reduces the interparticle forces and improves their flow properties (De Campos and Ferreira, 2013). Fine powders usually have poor flowability due interparticular forces that overcome gravitational forces, causing the powder to agglomerate. At this point, the ratio of Van der Waals forces to the particle’s weight increases with size reduction. As a result, the particle’s surface area per unit of mass decreases, generating a platform for cohesive forces to interact (De Campos and Ferreira, 2013). The poor flowability leads to heterogeneities in the powder layers and powder entrapment inside the part, even after de-powdering (Butscher *et al.*, 2012). This theory was proved by Geledar et al. in 2008, when comparing the angle of repose (AOR) of alumina powders with 6.59 μm and 63.1 μm. AOR increases when particle size decreases, implying a high degree of cohesion and low flowability (Geldart, Abdullah and Verlinden, 2009).

3. Wetting (the ability of the powder to absorb a binder): excessive wetting will cause binder spreading whilst lower leads to poor layer building. This is dependent on the powder hydrophilicity and can be determined by the contact angle between binder and powder. Higher binder viscosity hinders coverage whilst low viscosity promotes overspreading. Topography of the powder bed surface dictates absorbed binder quantities, specifically powder particle size and shape, e.g. round smaller particles have higher surface areas therefore a higher capacity for adhesion. Chemical reactions between powder and binder can lead to particle swelling when the amount applied is excessive. Particle dissolution occurs when the binder is not correctly chosen (Butscher *et al.*, 2011).

4. Interaction with fluids/binding: the interaction of the liquid binder with the powder bed involves the dissipation of kinetic energy of the droplet, surrounding of droplets by powder, infiltration of the liquid and rearrangement of the powder particles under the capillary forces (Lanzetta and Sachs, 2003). Binder concentration must be minimized because too high reactivity prevents binder spreading whilst too low favours it. Binder concentration should be adjusted to provide the part mechanical stability. Binding can happen via two mechanisms: powder dissolution by the binder with subsequent recrystallization, or by gluing of the powder particles with polymer-based binder (Butscher *et al.*, 2011). The 2 essential binding steps are binder absorption and mechanical interlocking. Binder absorption may happen via a chemical reaction and subsequent inter particle crystallization, or by particle adhesion. Either way the part needs to be post-processed to attain mechanical interlocking (Butscher *et al.*, 2011).

5. Sintering: the sintering step is very important for the successful processing of a ceramic part and has been described in detail on section 2.4.2. The protocol should encompass a de-binding step before the sintering step to allow the binder to evaporate without causing part distortion. For a glass-ceramic, the protocol includes a nucleation step and a crystal growth step that allows those crystals to grow. These steps are crucial once they provide the material enough crystallization to improve the mechanical properties (Butscher *et al.*, 2012; Alharbi, 2016; Mancuso *et al.*, 2017).

2.6.2 AM of biocomposites

AM as proven to be a powerful tool, especially in the medical area. The freedom of design and wide range of techniques available to produce lightweight complex geometries makes it an attractive approach to produce medical devices. Unfortunately, current AM is filled with proprietary materials which limits the range of physicochemical properties attainable. To overcome these problems, researchers are focusing on developing their own materials, especially composites, to enhance variety and improve properties of printed parts (Gao *et al.*, 2015; Yasa and Ersoy, 2018; Melo *et al.*, 2019). Although multi-material printers already provide a method of making composites layer by layer, a growing interest grew towards pre-blending materials (matrix and reinforcement) prior to the printing. The resultant composites exhibit unique characteristics and capabilities, and since they are tuneable, the possibilities are immense (Kalsoom, Nesterenko and Paull, 2016; Melo *et al.*, 2019). Most studies on

composites involve the use of thermoplastic matrices (PLA, Polyether ether ketone, ABS) reinforced with either carbon fibre or glass fibre, to improve the tensile properties of the material. Short and continuous fibres have been printed for application in automotive and aerospace sectors using FDM, SLS and other adapted/developed techniques. Using FDM for such applications is limitative in terms of material choice because it needs to have an ideal viscosity to be extruded and still provide structure rigidity to the final part. Thermoplastics are the first choice for this technique, but their mechanical properties are often lower than metals and ceramics. This is counteracted by using reinforcements made of a stronger material. When mechanical properties are in focus, fibres are the first choice. Long and oriented fibres loaded in high percentages (< 40%) contribute positively towards tensile properties, but with their introduction appears porosity. The voids created by the introduction of the reinforcement must be controlled since they deteriorate the fibre-matrix interface, hindering the mechanical performance of the device (Yasa and Ersoy, 2018). Short-fibres tend to be less used but authors such as Zhong et al. observed that by reinforcing ABS with short-glass fibres, tensile strength was favoured but flexibility and handling were reduced. Shofner et al. used vapour grown short carbon nanofibers and observed an increase in brittleness low interlayer and intralayer fusion above 10% loading. Despite this, tensile properties were still enhanced and high enough for the chosen application (Zhong *et al.*, 2001; Shofner *et al.*, 2003). In terms of content, Ning et al. concluded that the best percentage of loading was 5%, and anything above 40% wasn't printable due to nozzle clogging. The use of carbon fibres generally improved the tensile properties but decrease toughness, ductility and yield strength. Higher lengths favoured tensile properties but did not affect the yield strength value. Just like Shofner et al., the results showed an increase in porosity for 10% fibre loading (Ning *et al.*, 2015).

In the medical area, biocomposites are widely studied for musculoskeletal applications, commonly under the form of fixation devices or as scaffolds for bone regeneration (Wang, 2003). Using AM to produce such devices attracted both scientific and industrial community. Commonly printed with binder jetting, these include mixtures of glass powders with CaPs, but don't comprise the needed bioactivity for stimulation of a biological response. An example was Winkel et al. with the addition of HA to control shrinkage and improve stability of the structure during sintering. Polymer-ceramic biocomposites consisting of a thermoplastic polymer and a bioactive ceramic, are in focus once both ductility and strength can be obtained, from polymer and ceramic respectively. Work developed by Baino et al. reported the processing of a scaffolds containing β-TCP and collagen. The scaffolds could not be considered a composite since the ceramic part was fabricated via SLA and the collagen gel

casted onto it. Nonetheless, these structures presented fully interconnected pores and supported cell adhesion and proliferation up to 7 days (Zhang *et al.*, 2012). On a later work the author used CAD/Computer aided manufacturing (CAM) technology to study the cartilage bone transition area to create a biomimetic structure. The author observed defects on the subchondral bone plate which aimed the passage of blood vessels and nutrient into the bone tissue. This enlightened and improved the vision around bone scaffolds design of osteochondral interfaces (Bian *et al.*, 2016). Similar work based on the use of two techniques to produce different parts of the device, and joining them together, is available and reported, however on composites the knowledge remains scarce (Costa *et al.*, 2018).

Composite formulations comprising polymer and bioceramics proved to deliver bioactivity, osteoconductivity and mineralization of bone marrow-derived hMSCs (Kalsoom, Nesterenko and Paull, 2016; Melo *et al.*, 2019). Researchers such as Xiong et al., produced PLLA-TCP biocomposites using Low-Temperature Deposition Manufacturing (LDM) (figure 15). In their work, a slurry made of 15% PLLA, 15% TCP and 70% dioxane was prepared. Room temperature was kept stable to ensure no disturbance of the bioactive properties occurred. The slurry was fed into to the material supply, connected to a screw pump nozzle (0.3 mm diameter). The scaffolds were built in a layer by layer fashion, 0.15 mm layer thickness, under 0 ˚C to freeze the scaffold upon building. The scaffolds were freeze-dried to remove the solvent and to attain solid state at room temperature without losing shape and mechanical integrity (Xiong *et al.*, 2002).

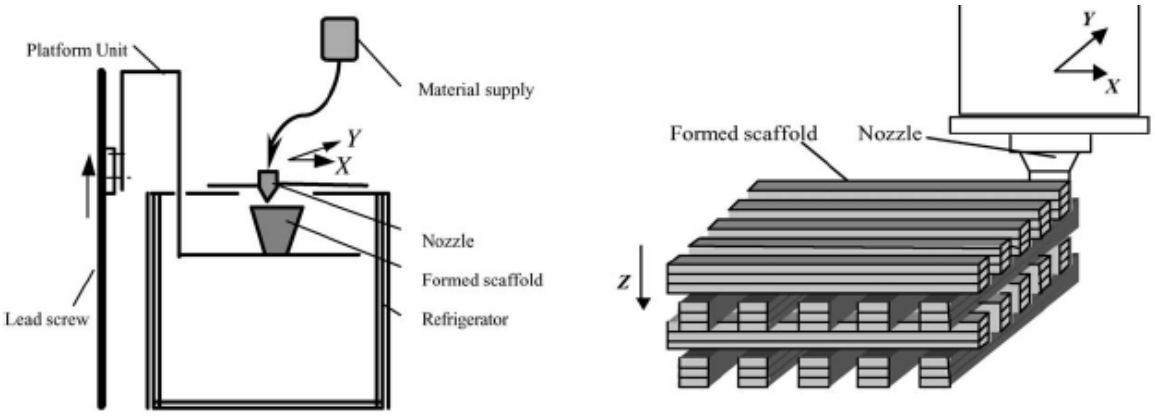

Figure 15 - Schematic of LDM process (left) and geometry of produced scaffolds (right) (Xiong *et al.*, 2002).

The low temperature was attained by refrigerating the vat containing the slurry as demonstrated on figure 15. Woodpile geometry was applied once it encompasses controlled porosity with high mechanical properties under compression. Porosity is key in bone

applications commonly within the range of 400-600 µm. This allows for cell migration, and multiple layer formation without clogging the pore. In this study the average pore size reported was 400 µm for macro-porosity and 5 µm for micro-porosity, with an overall porosity of 89.6%. These values can be tailored by changing layer dimension and distance between each rod of the pile. The scaffolds were implanted in canine radiuses where both new bone and marrow grew. Mechanical properties were low but within the range of spongy bone, 12 MPa and 60 MPa for bend strength and compressive modulus respectively (Xiong *et al.*, 2002).

Another interesting study on AM of biocomposites, consisted on the processing of PLLA and 10 wt% carbonated HA nanospheres using SLS (Zhou *et al.*, 2008). The nanospheres were produced using an emulsion technique and fed into a modified SLS machine. Tetragonal porous scaffolds were produced, using a layer thickness of 0.10 mm and laser power of 11-19 W. The results report an average macro-pore size of 0.6 mm, 0.2 mm smaller than the designed scaffold. On figure 16 fully fused PLLA particles are shown, however, for the composite the fusion level was lower. The author suggest that the particles at the surface prevented the fusion (Zhou *et al.*, 2008). On the same fashion of this technique, Du et al. fabricated graded composites using PCL/HA microspheres. The spheres were fed onto an SLS machine and used to produce multi-layered cylinder-shaped scaffolds. These struts showed excellent results in both *in vitro* and *in* vivo studies, inducing cartilage formation and regeneration of bone in the subchondral area (Du *et al.*, 2017). PCL/HA scaffolds have also been produced using FFF technology with the aim of osteogenic differentiation of hMSCs derived from adipose cells. The cells differentiated in both PCL and composite scaffolds, but with a preference for the composite construct (Endres *et al.*, 2003).

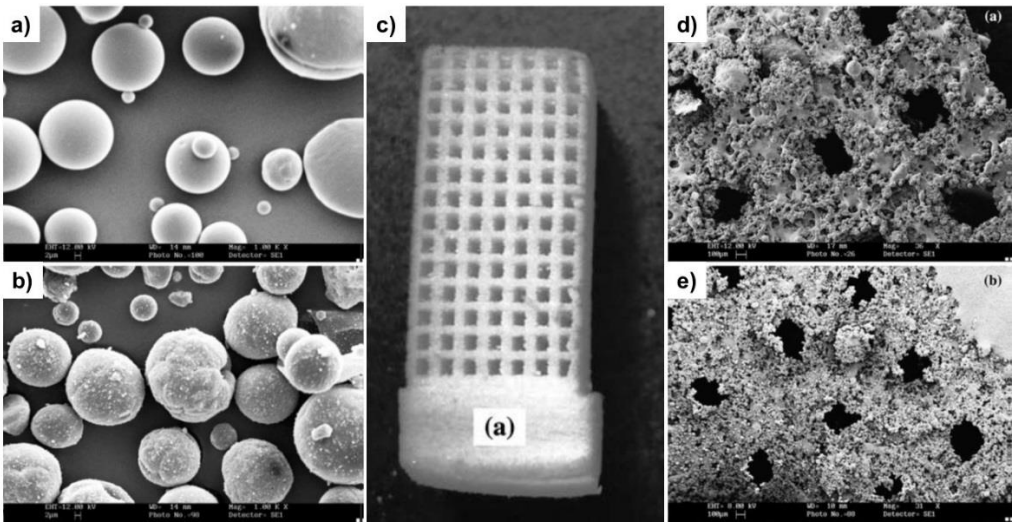

Figure 16 –SEM of microspheres: a) PLLA and b) PLLA/CHA. c) Printed part; f) and e) SEM of printed parts: d) PLLA and e) PLLA/CHA (Zhou *et al.*, 2008).

2.7 Summary of the literature review

The knowledge collected up to date allows to define some key conclusions that work as guidelines for the development of the current experimental work:

- AW bioactive glass-ceramics are a potential solution for load bearing applications in RM. Several *in vivo* and *in vitro* studies show that AW stimulates and promotes bone in-growth into the implant;
- AM techniques allow the fabrication of complex bespoke geometries and offer a variety of materials, getting the research closer to personalisation;
- Binder jetting is a versatile and low-cost process that permits the production of AW bone implants with porous microstructures, without the use of additives;
- Mechanical properties of printed AW implants mimicked the ones in human bone;
- Powder properties are essential for a successful fabrication once they influence manufacturing process, which relies on layer homogeneity and binder absorption;
- Sintering protocols must be defined accordingly to the material and include a de-binding process to allow the safe evaporation of the binder without shape distortion;
- Glass-ceramic crystallization process is important during material processing and is divided in 2 stages, nucleation and crystal growth. Changes in crystallization affect the material sintering and can change the processing properties, namely sintering temperature and dwelling time;
- Impurities can affect the sintering behaviour of glass-ceramic parts;

- Processing of biocomposites using AM is already under study with promising results, however the knowledge on polymer-ceramic printing is still scarce and needs further development;
- PLLA and other known thermoplastics are the focus materials for matrices while and bioactive materials such as HA, TCP and AW have been the chosen ones for reinforcement;
- The addition of bioactive ceramics to polymer matrices can enhance the material osteoconductivity and osteoinductivity. Biocomposites can provide degradability and bioactivity, whilst stimulating osteoconductivity and MSCs mineralization;
- The shape of reinforcement affects the material final properties and its processing route;
- Fibre-reinforced biocomposites are highly studied and show promising results for processing devices with enhanced mechanical properties;
- Fibre orientation and size influence the final tensile properties and ductility. Fibre content provides best results at 5 wt% but above 40 wt% printing ability is poor.

Chapter 3. Materials and Methods

This chapter introduces the materials and methods used in this research project. These are divided in 2 sections: section 3.1 reports on materials and methods with protocols gained from previous work, and section 3.2 reports on protocols which have been developed or further optimised during this project.

3.1 Standard Materials and Methods

3.1.1 AW-based materials

AW was introduced in chapter 2 and was the chosen bioceramic for this project. The AW glass-ceramic precursor was produced via a melting route by Glass Technology Services (Sheffield, UK) and supplied under the form of frit with a density of 3.078 g/cm^3 (Kokubo *et al.*, 1985; Alharbi, 2016). The base batch composition of the glass-ceramic precursor provided in literature consists of $4.6MgO{\cdot}44.7CaO{\cdot}34SiO_2{\cdot}16.2P_2O_5{\cdot}0.5CaF_2$ (in wt%).

The use of this material on this research group is common, being this project a continuation of the works developed by Alharbi. N. and Mancuso, E and Rodrigues, N. throughout their PhD studies, where this AW was used as powder feedstock for binder jetting printing of load bearing devices (Alharbi, 2016; Mancuso, 2016; Rodrigues, 2018). Highlighting this fact is important since the studies developed in the current project allowed to understand why the material changed its thermal behaviour, once passed from Mancuso, E. to Rodrigues, N. In this project it is demonstrated (chapter 4) that this is derived from an Al_2O_3 contamination of the powders.

To better understand the study, the materials were nominated from M1 to M6, being M1 the powder acquired for the studies of Alharbi, N. and Mancuso, E. M2 was later provided to Rodrigues, N. and was the powder used in chapter 5 for the binder jetting process. According to an elemental analysis performed on the materials, the M1 was contaminated with 0.68 wt% Al_2O_3 and M2 with 0.14 wt%. This contamination is thought to be acquired during the milling process, therefore, to be present at the surface of the particles. To be able to understand how the Al_2O_3 affects the material, 3 new AW glasses were created by adding the percentages of Al_2O_3 detected in M1 and M2, to the AW base formulation. A pure AW powder was also created as a control.

The new powders developed consisted of M3, a pure AW with a final percentage of 0.04 wt% Al_2O_3, M5 and M6 with 0.13 wt% and 0.61 wt%. The formulations in detail are demonstrated on table 10, prior to normalisation.

3.1.1.1 Alumina doped AW

The glass making process was performed at Glass Technology Services (Sheffield, UK) and will described in detail. The raw materials were weighted using a pan top balance (KERN 3000-2) and mixed for 5 minutes using a turbular mixer (TURBULA System Schatz T2C), amounting to a total of 500 g for each batch. Once mixed, half the powder was transferred into a silica crucible and placed inside a furnace (Lenton EAF 17/12) at 1400 ˚C for 30 minutes. When molten, the other half was added and left to melt and mix for a further 60 minutes. Finally, the crucible was carefully removed from the furnace and the molten glass poured into a steel mould and left to cool down. This was considered the first melting step and aimed to mix the ingredients and allow the evaporation of CO_2. The cool glass was cracked with a hammer and the resulting pieces placed inside 2 platinum crucibles, with spare pieces used to perform XRF analysis as described in 3.1.3.2. The platinum crucibles were placed in a different furnace (Lenton UAF 17/12) at 1400 ˚C for 1 hour. This was considered the re-melting stage which allowed the glass mixture to become homogeneous. Once fully molten, the glass was poured into a metal vase filled with cold water to create the glass frit. M1 powder batch was obtained as frit and milled with a planetary mill equipped with alumina balls (Pulverisette 6 grinder, Fritsch, Germany) at 400 rpm in two stages of 2 minutes each. Later, it was milled at 410 rpm for 3 minutes to homogenize and attain a smaller particle size. The M2 powder batch was milled with a ball mill (CAPCO 12VS, USA) equipped with porcelain balls for 10 hours. Later, using the previously referred planetary mill, it was processed at 410 rpm for 2 minutes. For M3, M4 and M5 powders, the glass frit was initially milled using the mentioned ball mill, and porcelain balls, for 8 hours. The powder was then sieved through a 200 µm sieve mesh using a sieve shaker (Podmore's Engineering, Stoke-on-Trent, UK), to obtain a particle size below 200µm. At this stage the particle size was not confirmed by mastersizer. Further milling, using the planetary mill at 410 rpm for 3 minutes, allowed the decrease of the particle size to the desired range, 122 µm ± 8.5 µm (mean ± SD). Sieving was performed with an Auto Sieve Shaker SV001 (Impact, UK), with 90 µm, 53 µm and 20 µm sieve meshes for a minimum of 1 week. Finally, the blend was created by mixing the powder from each size range, in is designated percentage, inside a roller mixer (Stuart, SRT6, UK) for 3h.

Material	Alumina role	Composition (wt%)
M1	At particle's surface	$4.6MgO{\cdot}44.7CaO{\cdot}34SiO_2{\cdot}16.2P_2O_5{\cdot}0.5CaF_2 + 0.68Al_2O_3$
M2		$4.6MgO{\cdot}44.7CaO{\cdot}34SiO_2{\cdot}16.2P_2O_5{\cdot}0.5CaF_2 + 0.14Al_2O_3$
M3	NA	$4.6MgO{\cdot}44.7CaO{\cdot}34SiO_2{\cdot}16.2P_2O_5{\cdot}0.5CaF_2$
M4	Dopant	$4.6MgO{\cdot}44.6CaO{\cdot}34SiO_2{\cdot}16.2P_2O_5{\cdot}0.5CaF_2{\cdot}0.14Al_2O_3$
M5		$4.6MgO{\cdot}44.4CaO{\cdot}33.8SiO_2{\cdot}16.1P_2O_5{\cdot}0.5CaF_2{\cdot}0.68Al_2O_3$

Table 10 - Batch composition of all developed glasses, doped with alumina and control (without alumina).

3.1.1.2 Sample preparation for SEM and XRD analysis– uniaxial compression

The powder was processed into a blend with particle size ranging from 20-90 μm, using the method described in 3.1.1.1. Each powder batch was processed into discs with 10 mm diameter and 2 mm thickness, using a uniaxial manual press (Specac IST, Specac Ltd, USA). In order to mould the powder into discs, a paste was prepared containing AW and isopropanol on a 3:1 (w/w) ratio, which translated in 0.35 g of AW and 0.1g of isopropanol per sample. The material was weighted using an analytical balance (Sartorius UC152) and mixed until it attained a paste-like texture and most isopropanol evaporated. The paste was left to dry for 40 s at room temperature and poured into the mould to be pressed at 1 ton for 1 minute. The green parts were sintered (SNOL 1300, TMS Europe, UK) using a 2-step protocol, consisting of a nucleation step and crystal growth phase (Alharbi, 2016; Mancuso *et al.*, 2017). The nucleation step was kept common for all batch types, 779 °C with 1-hour dwell. The crystal growth step dwell time was maintained as 1 hour however, for the sintering temperature, different values were applied. M1 was kept at 1150 ˚C as previously established (Mancuso *et al.*, 2017), and M2 and doped batches sintered at 1250 °C.

3.1.1.3 Preparation of M1 and M2 AW powder

Prior to processing the samples, the AW frit was converted into a powder blend with desired particle size ranges, via milling, sieving and mixing.

Milling and sieving

The AW frit was primary milled for 10 hours using a ball mill containing porcelain/alumina balls (CAPCO 12VS, USA). The obtained powder was sieved through a 200 μm sieve mesh

using a sieve shaker (Podmore's Engineering, Stoke-on-Trent, UK), to obtain a particle size below 200 µm. At this stage the particle size was not confirmed. Further milling, using a planetary mill containing zirconia balls (Pulverisette 6 grinder, Fritsch, Germany) at 410 rpm for 3 minutes, allowed the decrease of the particle size to the desired range, 122 µm ± 8.5 µm (mean ± SD). The sieving was done using an Auto Sieve Shaker SV001 (Impact, UK), with 90 µm, 53 µm and 20 µm sieve meshes for a minimum period of 1 week.

Mixing of powders

The AW powder obtained from different sieve meshes (single or combined with a solid binder), was placed inside a roller mixer (Stuart, SRT6, UK) for 3h.

3.1.2 Binders

3.1.2.1 Maltodextrin – solid binder

Maltodextrin (MD) is a product from starch hydrolysis, and is considered an amorphous thermoplastic polymer with a T_g ranging from 100 °C to 200 °C (Raja *et al.*, 1989). Following previous studies, described in chapter 2, MD (MyProtein, UK) was chosen as the solid binder to create the final powder blend for binder jetting printing. In this study, MD is also used as a solid binder, introduced in the binder jetting blend to act as glue for the AW particles. As part of the blend creation process, the MD was sieved to attain the desired particle size range of 20-53 µm, using the method described on 3.1.1.3.

3.1.2.2 Zb®60 – liquid binder

This product consists of a liquid binder, which will interact with the MD to create a glue that keeps the glass-particles together allowing for the creation of a green part. The clear water-based binder was purchased from EMCO Education Ltd (UK) with a composition of 18% humectant, 4% polymer and 78% water (in wt%).

3.1.3 Base polymer - PLLA

PLLA is an aliphatic polyester, approved by the US Food and Drug Administration (FDA), and commercialized under the medical grade standard. For this project, PLLA (Purasorb PL 38, Corbion - Purac Biomaterials), with a density of 1.24 g/cm^3, was selected and used as a matrix for PLLA/AW biocomposites processed via FFF printing. The material properties are shown in table 11.

Property	Poly(L-lactic-acid)
T_m (ºC)	170
T_g (ºC)	56
Shape	Fibre, Sponge, Film
Tensile strength (MPa)	900 (fibre)
Young's Modulus (GPa)	8.5 (fibre)
Elongation at break ε_B (%)	25 (fibre)
P^d_{wo} (37ºC – period until becomes water in saline water)	3-5 years
P^e_{t50} (37ºC – period until tensile strenght becomes 50% in saline water)	6-12 months

Table 11 - PLLA physicochemical properties (Melo, 2014).

3.1.4 Binder Jetting printing and sintering – production of AW scaffolds

The overall printing process of an AW scaffold is demonstrated in figure 17 and consists of 3 phases: powder preparation, printing and post processing. The first step is the formulation of the powder blend. The powder blend used in this work aimed a faster sintering, and completed the current AW/MD powder blend catalogue (Alharbi, 2016; Rodrigues, 2018).

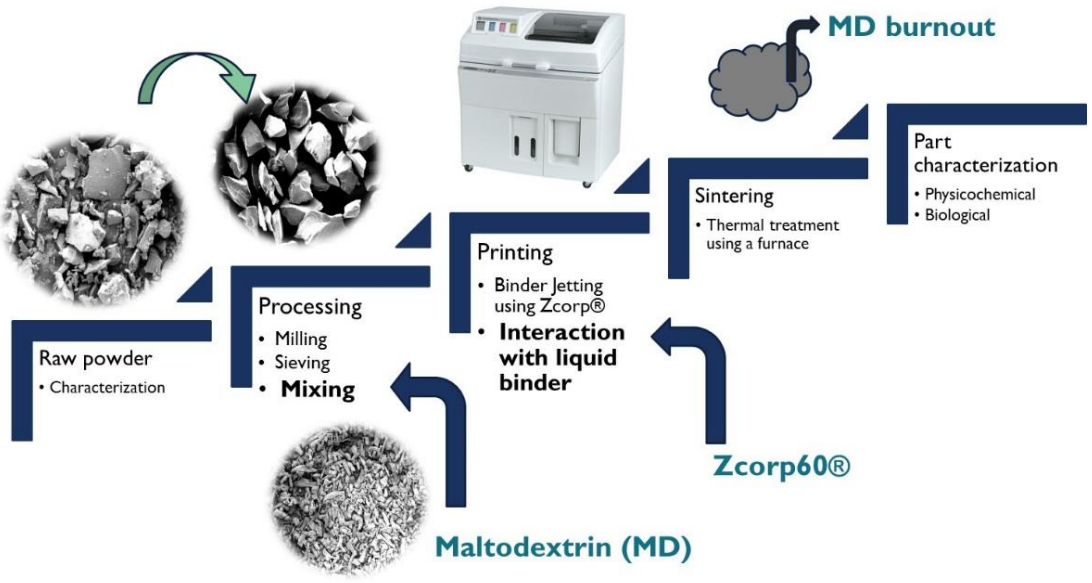

Figure 17 - Overview of printing process using binder jetting and sintering, from raw material preparation to the part characterisation. Process is initiated with powder blend preparation which included the grinding of AW, sieving and mixing of AW with MD, and then the

drying. The printing is performed, and the result is a green part. The green part is sintered using a defined protocol to allow the material to crystallise and attain structural integrity.

For a successful printing, a minimum of 500 g of powder must be used. For this, AW was mixed with MD on a 70% to 30% ratio, respectively. The final blend morphology consisted of:

- MD (20µm-53µm): 30%, 150 g;
- AW (53µm -90µm): 30%, 150 g;
- AW (20µm -53µm): 25%, 125 g;
- AW (< 20 µm): 15%, 75 g.

The powder blend preparation was performed according to the protocol described in 3.1.1.3.

3.1.4.1 Powder bed properties

The characterisation was based on 3 parameters: powder bed density, powder flowability and packing ability. For the powder bed density and degree of compaction, a tap density test was applied (figure 18a). A cylinder was filled with 100 ml, the initial volume (*Vi*) of the powder blend and tapped every second for 3 minutes. The tapping time was estimated by performing a pilot assay. Here the time needed for the powder to stop descending inside the cylinder was measured with a timer (Samsung Galaxy S5). Once no descendent movement was detected the final volume (*Vf*) was recorded. The powder blend mass was also recorded before and after the tapping test to calculate the powder bed density and estimate the amount of air within the mixture. With the obtained values, the Carr index (compressibility of powder), Hausner ratio (flowability) and powder bed density were calculated (equation 10, 11 and 12, respectively).

$$C.index(\%) = \left(\frac{V_i - V_f}{V_i}\right) \times 100 \quad Equation\ (10)$$

$$H.\ ratio = \frac{V_i}{V_f} \quad Equation\ (11)$$

$$\rho_{bed} = \frac{m_f}{V_f} \quad Equation\ (12)$$

The powder flowability was also measured using the funnel test (figure 18b). The procedure consisted on passing the powder blend through a funnel to investigate how powder settled once deposited. The funnel was slowly dislocated upwards to keep a safe distance from the tip of the forming cone, and the powder allowed to flow freely. Once all powder passed through

the funnel, measurements of the cone height (h) and base diameter (d) were taken and used to calculate the angle of repose (θ) (equation 13).

$$\theta = \tan^{-1}\left(\frac{2h}{d}\right) \qquad Eq.(13)$$

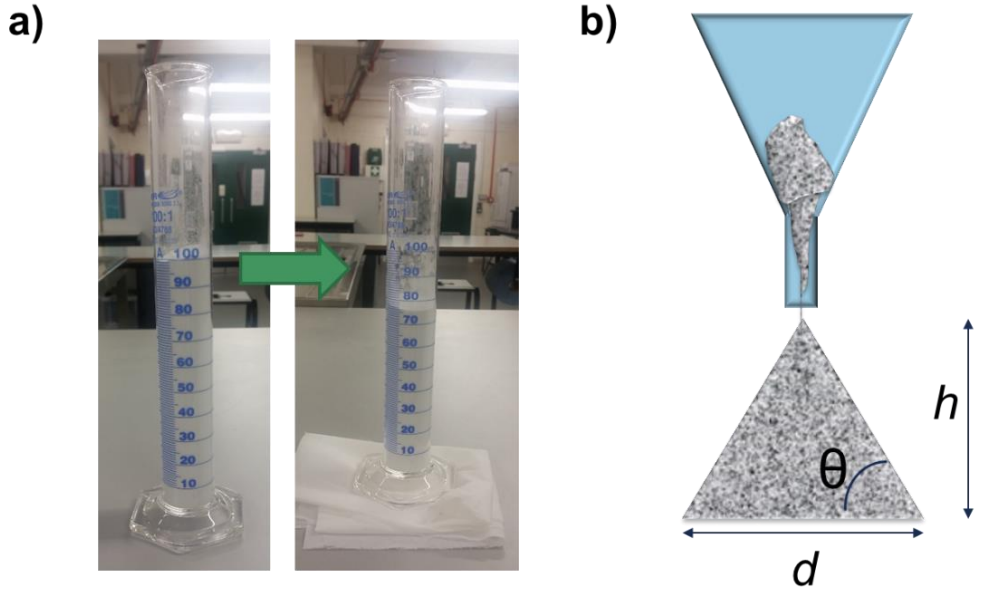

Figure 18 - Powder bed properties. a) Measurement of tap density, before and after 3 minutes tapping. b) Schematics of the funnel test for the flowability of the powder.

3.1.4.2 Binder Jetting printing and sintering

The printing was done on a commercial ZPrinter® 310 Plus (ZCorporation, Rock Hill, SC, USA). The printing process started with the design of the implant. Two types of samples were created using this method, discs (12 x 2 mm) and bars (2 x 30 x 2 mm), as presented in figure 19. Samples were sketched using a CAD software (Autodesk Inventor, Professional 2015, Autodesk Inc.) and converted to an STL file. The file was uploaded into the printing software, and the following printing parameters were defined:

- Layer thickness: 0.1 mm.
- Binder to volume ratio of inner core: 0.1.
- Binder to volume ratio of the shell: 0.21.

The printing process was explained on chapter 2, section 2.5.1. Briefly, a liquid binder is selectively deposited onto a powder bed on a layer by layer fashion. The final part is left to dry for a minimum of 12 hours. The powder surrounding the printing area, which did not get in contact with the liquid binder, was immediately removed to avoid moisture absorption. Once

the parts dried, unbound powder was carefully brushed away and the green body taken for sintering. The sintering process was performed in a state of the art furnace (SNOL 1300, TMS Europe, UK) and the heating protocol divided in 3 steps: de-binding (350 °C, at 2.5 °C/min), crystal nucleation (779 °C, at 5 °C, hold 1 hour) and crystal growth (1250 °C, at 5 °C, hold 1 hour).

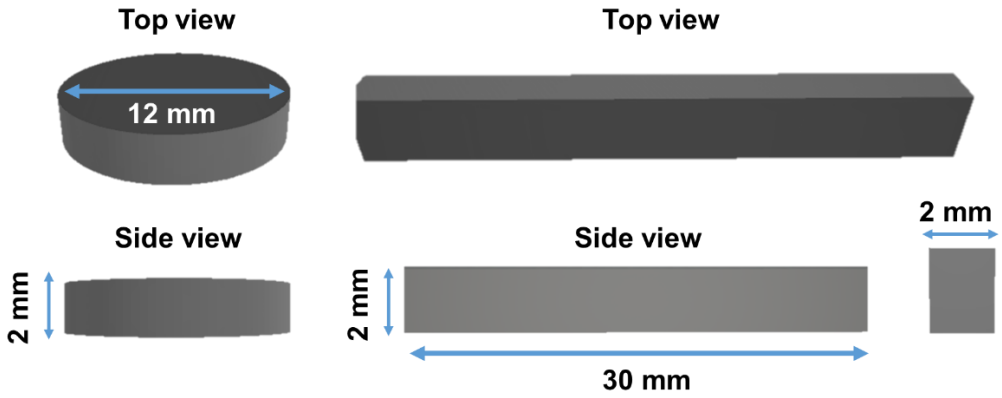

Figure 19 - Design of binder jetting samples using CAD software. Disc samples used for physiochemical and biological characterisation. Bars samples aiming mechanical testing via 3-point bend test.

3.1.4.3 Part density and porosity measurements

The density of samples was measured using an Archimedes kit, mounted onto a precision balance (KERN ABT 220-5DM, ± 0.1 mg, a maximum weight capacity of 220 g, Germany). Firstly, the sample dimensions were taken using a calliper, and used to calculate the bulk volume, as per equation 13, where *h* is the height of the sample and *r* the radius. Firstly, the samples were weighed to obtain the dry mass (*m1*). Then, each sample was immersed in di-ionized water (DI) to obtain the immersed mass (*m2*), and finally gently dried with a paper towel and reweighted to obtain the wet mass (*m3*).

The values were applied to equation 14, equation 15 and equation 16, to calculate the bulk density, total porosity and open porosity, respectively. AW density was defined as 3.078 g/cm^3 (Alharbi, 2016).

$$Volume\ (cm^3) = h\pi r^2 \quad Equation\ (13)$$

$$\rho_{bulk}\left(\frac{g}{cm^3}\right) = \frac{m_1}{Volume} \quad Equation\ (14)$$

$$Total\ porosity\ (\%) = \left(1 - \frac{m_1}{AW density \times sample\ volume}\right) \times 100 \quad Equation\ (15)$$

$$Open\ porosity\ (\%) = \frac{m_3 - m_1}{m_3 - m_2} \times 100 \quad Equation\ (16)$$

The estimation of pore size and size distribution was based on image analysis, using the .tiff files obtained from the XRCT (analysis to be described in 3.1.3.5). To better understand the distribution of the porosity within the samples, 3 samples were scanned, and 3 areas of the sample used for the analysis: top, middle and bottom. From each area, 5 scans were considered, to increase the accuracy of the measurement. Briefly, images were opened on imageJ (NIH) and submitted to a thresholding treatment to isolate the pores (figure 20). Since the pores have irregular shapes, the Feret diameter function was applied and the measurements taken considering the maximum dimension of each pore. The obtained values were statistically treated using the software GraphPad Prism (section 3.1.9).

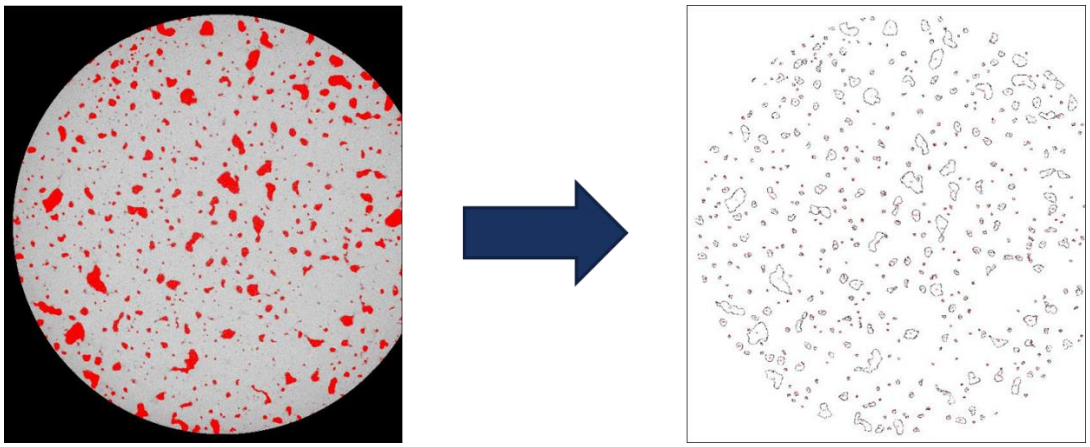

Figure 20 - Pore size analysis using imageJ. Thresholding to obtain pore isolation and pore contouring allowing the calculation of Feret diameter.

3.1.4.4 Shrinkage evaluation

The volumetric shrinkage was assessed on a total of 5-disc shaped samples. Diameter and height, before and after printing, were measured using a calliper then used to calculate the initial and final volumes of the samples. Shrinkage was calculated in volume (equation 17) and linear, the latter for (x,y) plane (equation 18) and in (z) (equation 19). Values were treated as in 3.1.9.

$$Shrinkage\ in\ V\ (\%) = \frac{V_i - V_f}{V_i} \times 100 \quad Equation\ (17)$$

$$Shrinkage\ in\ (x,y)\ (\%) = \frac{r_i - r_f}{r_i} \times 100 \quad Equation\ (18)$$

$$Shrinkage\ in\ (z)(\%) = \frac{z_i - z_f}{z_i} \times 100 \quad Equation\ (19)$$

3.1.5 Methods for physicochemical characterization

3.1.5.1 X-ray diffraction (XRD)

XRD analysis allows the evaluation of the material's crystallinity and structure. The samples were analysed using the PANalytical X'Pert Pro MPD, powered by a Philips PW3040/60 X-ray generator and fitted with an X'Celerator detector. Diffraction data was acquired by exposing the samples to Cu-K_α X-ray radiation, with a characteristic wavelength (λ) of 1.5418 Å. X-rays were generated from a Cu anode supplied with 40 kV and a current of 40 mA. The data was collected over 0-60 2θ range, and the scans analysed using the equipment software PANanalytical X'Pert HighScore Plus©. The patterns compared to the ones within the data bases provided by the supplier (ICDD 1999 and COD 2016).

The AW was examined prior to processing, in raw powder form (glass-ceramic precursor), and post-processing, as a compressed pellet and printed scaffold. The crystallinity of the PLLA was also assessed in all 4 stages of the scaffold processing: 1) granule form (raw); 2) post-melting in hot plate; 3) as extruded filament; 4) as printed scaffold (FFF). Further details on the sample processing for AW and PLLA based composites are described in chapters 4, 5 and 6.

3.1.5.2 X-ray fluorescence (XRF)

This technology measures the secondary X-rays emitted by a sample when excited by a primary X-ray source (Fishcher, 2019). It was used to confirm the elemental composition of produced AW powders as produced. The frit samples were milled into fine powders (< 45 µm) and mixed with a bonding agent (20 wt%, CEROX BM-0002-1, FluxANA, Germany). The resultant paste was pressed into pellets to produce homogenous samples for analysis. The analysis was performed using a wavelength disperser XRF S4 Pionner (BrukerAXS GmbH) with a collimator of 0.46˚, no filter, and in vacuum conditions. The operation was conducted using a fundamental oxides detection mode.

3.1.5.3 Scanning electron microscopy (SEM)

Samples from both physicochemical and biological characterization were imaged with SEM. The samples for physicochemical characterization were mounted on an Al stub and fixed using disc shaped carbon adhesives. The coating was performed with 15 nm gold particles using a sputter coater (Polaron SEM Coating Unit), and then dried overnight. For the imaging of samples seeded with hMSCs, additional preparation steps consisting of sample dehydration and

critical point drying were performed. Dehydration was carried out using, 25%, 50%, and 75% ethanol (30 minutes each) followed by 100% ethanol (2 x 1 hour). A final dehydration step was performed with CO_2 in a Baltec Critical Point Dryer (Leica Geosystems Ltd). Fixed specimens were mounted on an Al stub with Achesons Silver Dag (Agar Scientific) and then dried overnight. The observation of all samples was performed by the TESCAN VEGA LMU SEM, housed within EM Research Services, Newcastle University. The images were collected using the software supplied by TESCAN.

3.1.5.4 Powder morphology analysis

The particle size and size distribution were measured using a laser particle size analyser Mastersizer 3000 (Malvern Instruments Ltd), in dry cell mode. For each sample type, 5 readings were accounted to allow the statistical analysis. The collected data was treated with the equipment's software, which allows for the calculation of particle size and size distribution, per percentage of volume. The size distribution was estimated using the Dx values, Dx10, Dx50 and Dx90 which indicate the amount of sample under a certain size (μm) (Malvern Ltd, 2019).

3.1.5.5 X-ray computer tomography (XRCT)

The microstructure of processed devices was investigated with an XRadia/Zeiss VersaXRM 410 XRCT (Carl Zeiss Vision Inc.), providing 1 μm resolution. AW samples were analysed using a scanning voltage of 140 kV, a current of 71 μA, with a voxel size of 2.6 micro voxels. Approximately 600 slices were obtained, covering the full sample height. The scanned 2D slices were used for the reconstruction of the 3D model using Avizo Fire software (Durham University, UK). For the biocomposite samples, all parameters were maintained except the applied voltage which was 60 kV.

3.1.5.6 Differential Scanning Calorimetry/Thermogravimetric Analysis (DSC/TGA)

The DSC and TGA analysis aimed to detect the temperature at which the main thermal transitions occur, glass-transition (T_g), crystallization (T_c) and melting (T_m). Both T_g and T_m were represented as endotherm transitions while T_c was shown as exothermic (Bottom, 2008; Pooria Moghadam, Tohidi and Ranjbar, 2010). Mass loss from thermal degradation was recorded simultaneously. The DSC/TGA measurement of AW powders was done using a DSC Q600 (TA instruments, USA) and the results treated using TA Universal Analysis software. The samples were placed in a platinum crucible and heated from 25 °C to 1400 °C

at a rate of 10 °C/min. An empty crucible with the same weight was used as reference. Due to equipment restrictions, the DSC analysis of the PLLA was performed on a Mettler Toledo DSC 3 (Mettler-Toledo Ltd, U.K.). The polymer was placed inside an Al pan (12.5 mg) and an empty pan was used as reference. Each sample was heated from room temperature up to 250 °C at a rate of 10 °C/min. The data was collected using the supplier's software, STARe Evolution. The results obtained from both machines were exported into Microsoft Office Excel and plotted as Heat Flow (mW) vs Temperature (°C).

3.1.5.7 Hot Stage Microscopy (HSM)

HSM is highly used for ceramics and glasses to determine their temperatures of softening, melting, flowing and sintering. The result of the data treatment is a plot where several variables can be analysed as a function of temperature (Panna, Wyszomirski and Kohut, 2016). The AW powder (particle size < 20 μm) was mixed with deionised water to form a paste and inserted into a moulding device with cylindrical shape (2 x 3 mm). The AW samples were analysed on a Misura® equipment (Expert System Solutions, Italy), with an isothermal protocol ranging from 25 °C to 1300 °C, at a rate of 10 °C/min. A video camera, placed inside the instrument, allowed the monitoring of changes in the sample silhouette with temperature. These were later processed into images and videos. The data acquired was also converted into graphs using Microsoft® Office Excel.

3.1.5.8 Mechanical testing

The mechanical properties (n=5 per material) were assessed through 3-point bend test and compression, using 1 mm/min crosshead speed, on a standard testing machine (Shimadzu, United Kingdom), with a 5 kN load cell. The effective modulus was calculated from the stress-strain curve, as the slope of the linear part of the curve. The yield point for both flexural and compressive strength was determined at the point where strain occurs without the increase in loading. The data was exported from the equipment software (Trapezium X, Shimadzu, United Kingdom) as a .csv file and treated with Microsoft® Office Excel to obtain the stress-strain curves. The statistical analysis was performed on Graph Pad Prism 7, as described below in 3.1.7. The samples types analysed consisted of:

- AW bars processed using binder jetting (2 x 30 x 2 mm, as in section 3.1.4.2), span length of 26 mm;

- PLLA and PLLA/AW bars processed using FFF (10 x 40 x 3 mm, as in 3.2.2.2), span length of 32 mm;
- PLLA and PLLA/AW squares processed using FFF (10 x 10 x 3 mm, as in 3.2.2.2).

For the AW pellets (8 mm diameter, 2 mm thickness) created with uniaxial compression, the compression test was performed on the same type of testing machine (Shimadzu, United Kingdom), using a 10 kN loading cell, with a crosshead speed of 1 mm/min. For the sample analysis (n=5), a 30 N pre-load was applied, and the strain normalised accordingly.

3.1.6 In vitro degradation assay

3.1.6.1 Mass loss and pH variations

Samples were weighed (n=3 per material) using a precision balance (precision of ≥ 0.001 g, Sartorius, Sartorius AG), placed into individual plastic vials containing Phosphate Buffered Solution (PBS) with an average pH 7.4 (Sigma Aldrich, UK), and incubated at 37 °C. Squared and bar shaped samples were immersed in 5 ml and 25 ml of PBS, respectively. The solution was refreshed weekly and measurements were taken at week 1, 2, 4, 6 and 8. To assess the mass loss, samples were incubated at 37 ˚C for 48h, and re-weighed to obtain the dry weight. Flexural strength was assessed according to the method described in section 3.1.3.8. The pH of the solution was measured using a portable FG2-Kit Five Go™ pH meter (Mettler Toledo Ltd, UK), with a calibration at pH 2 and pH 7, lower and higher range respectively.

3.1.6.2 Ion leaching via inductively coupled plasma mass spectrometry (ICP-MS)

The collected PBS solution was analysed by ICP-MS on a Thermo X-series2 instrument operating in collision cell mode (using 3 mL/min 8% H2 in He as collision gas) for elemental detection. The samples were diluted 5-fold in 2.5% (w/v) high-purity HNO3 (Merck) containing 20 µg/L indium (In) and platinum (Pt) as internal elemental standards. For each sample, magnesium (24Mg), calcium (40Ca), indium (115In), and platinum (195Pt) isotopes were monitored sequentially using the peak-jump method (100 individual reads of 20-30 ms on each isotope). This was performed across 3 channels of 0.02 atomic mass unit separation, each analysed in technical triplicates. Elemental concentrations were determined by comparison with matrix-matched standard solutions (Merck) of known elemental composition (0 – 1,000 µg/L) studied within the same run. The samples were prepared by the author and

the analysis performed by Dr. Kevin Waldron at the Institute for Cell and Molecular Biosciences, Faculty of Medical Sciences, Newcastle University.

3.1.6.3 Diffusion Ordered Nuclear Magnetic Resonance Spectroscopy (DOSY)

Diffusion NMR ^{1}H proton measurements were used to determine polymer chains hydrodynamic radii. These were carried out using a Bruker Avance III 400 MHz nuclear magnetic resonance (NMR) spectrometer, equipped with a 5 mm SMART probe. All measurements were carried out at 298 K using Bruker ICON automation software and processing carried out using Bruker Topspin software (V3.6.1). Samples were analysed using a bipolar gradient pulse and calculations are made using the Stokes Einstein equation (equation 20).

$$D = \frac{K_B T}{6\pi\eta R_H} \quad Eq.(20)$$

Here D is the diffusion, K_B the Boltzmann constant, T the temperature, η the dynamic viscosity and R_H the molecules hydrodynamic radii. Samples were dissolved in deuterated chloroform ($CDCL_3$) (1 mg ml^{-1} concentration) and analysed across 64 magnetic gradient intervals to determine polymer and solvent diffusion (Swift *et al.*, 2017). The relative sample viscosity of the sample was determined via comparison to a $CDCL_3$ blank (D = 2.59 x 10-9 m^2 S^{-1}) with a known solvent viscosity (5.28 x 10^{-4} kg m^{-1} s^{-1}) (Rabinovich, Labashov and Kucheryavyi, 1960). Sample viscosity was determined via changes in solvent diffusion and thus a corrected polymer material hydrodynamic was determined from PLLA ^{1}H proton diffusional shift. The analysis was performed by Bradford University.

3.1.7 Assessment of bioactivity – immersion in SBF

To evaluate the deposition of an HCA layer on top of the prepared scaffolds, a bioactivity assay was performed as demonstrated on figure 21. The SBF was prepared according to the instructions provided by Kokubo and Takadama (Kokubo and Takadama, 2006), with a final ionic concentration of 142Na^{+}, 5K^{+}, 1.5Mg^{2+}, 2.5Ca^{2+}, 147.8Cl^{-}, 4.2HCO_3^{-}, 1HPO_4^{2-} and SO_4^{2-} (in mM), with pH 7.42, at 36.5 °C. The samples were immersed in 5 ml of SBF (n=3 per material), incubated at 37 °C and the solution refreshed weekly. At each time point, samples were removed from the SBF solution and immersed in di-ionised water for 30 s, to remove the precipitated salt, and dried in the incubator at 37 ˚C for 48h. Measurements of the SBF solution

pH were taken at day 1, 7, 14 and 21 and the samples surface observed under SEM (section 3.1.5.3).

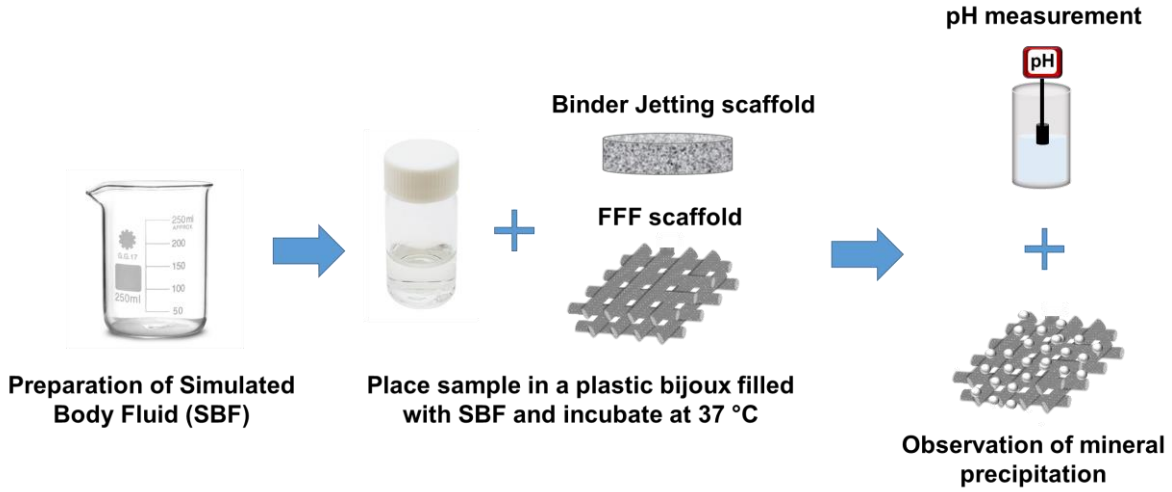

Figure 21 - Overview of bioactivity assessment assay for both bioceramic and biocomposite samples. Process begins with the preparation of SBF solution, where samples are immersed in for a determined amount of time. Analysis of results consisted on the observation of precipitated minerals and reading of the pH solution.

3.1.8 Cell studies

3.1.8.1 Cell culture

TERT hMSCs (hTERT-MSCs) Y201 , an immortalized cell line (James *et al.*, 2015), were cultured up to passage 87 before being used in this study. Cell culture consisted on seeding the Y201 cells into T175 culture flask containing Dulbecco's modified eagle medium, (DMEM) with high glucose, sodium pyruvate, L-glutamine and phenol red (Gibco; Thermo Fisher Scientific). Cell were then incubated at 37 °C in a humidified atmosphere of 5% CO_2. Media change was performed every 2 days until the desired cell density for the assay was attained.

3.1.8.2 Cell seeding method

The scaffolds were firstly sterilised and washed with Dulbecco's PBS (DPBS; Sigma Aldrich, UK) before being placed in 12 well plates. The hTERT MSCs were seeded in triplicate on top of the scaffolds at a density of 50 000 cells/scaffold and then incubated at 37 °C in a humidified atmosphere of 5% CO_2. Cell number was previously defined on a pilot study. Cells were maintained in the culture media mentioned in previous section, refreshed every 2

days. Tissue culture plastic was used as a positive control. Cells were cultured for a total of 21 days with defined time points varying according to the analysis being performed.

3.1.8.3 MTT (3-dimethylthiazol-2,5-diphenyltetrazolium bromide) colorimetric assay

The metabolic activity of cells was measured in triplicated using an MTT kit (Thiazolyl Blue Tetrazolium Bromide; Sigma Aldrich*)* after 1, 3, 7, 14 and 21 days. The MTT solution was prepared according to supplier instructions to reach a final concentration of 0.5 mg/mL. The solution was mixed with serum-free DMEM, deprived of phenol red (Gibco; Thermo Fisher, UK) and incubated for 4 hours, at room temperature and away from light. The media was removed, replaced with 400 µL of isopropanol and the plates agitated for 30 minutes. The absorbance was read with a spectrometer (ELx800; BioTek Instruments, UK) at 570nm. To estimate the cell number, a standard curve was created by seeding hTERT-MSCs in different densities (0, 10 000, 30 000, and from there onwards up to 450 000 with a 50 000 increment).

3.1.8.4 Live and dead staining

Cytotoxicity was assessed at day 1 and day 3, using a live/dead kit (Thermo Fisher, UK). The stock solutions were prepared in accordance to the manufacturer's recommendations, meaning a final concentration of 4 µM of ethidium homodimer-1 and 2 µM of calcein. Briefly, the media was removed from the wells and the samples were washed twice with PBS. The prepared solution was pipetted into the wells, followed by incubation for 30 minutes at room temperature, protected from light. Imaging was done through an inverted confocal microscope (LSM 800; Carl Zeiss Ltd) which required the placement of each sample in a supplied plastic dish (seeding surface facing the lens), and the addition of DPBS to avoid sample drying. For the imaging, predefined laser wavelengths were applied, AF488 (410-546nm) for green (live) and AF546 (576-700nm) for red (dead).

3.1.8.5 Cell fixation and base staining for confocal microscopy

Samples were collected at day 1, 7 and 21 for morphological observation via confocal microscopy. The cellular media was aspirated, and samples were washed with DPBS. A solution of 4% paraformaldehyde (Sigma Aldrich) was added to the wells and incubated for 15 minutes at room temperature. Cells were washed 3 times with a DPBS/0.1%Tween 20 solution, immersed in 3% w/v Goat's serum/DPBS/0.1%Tween 20 and incubated for 30 minutes at room temperature. A primary antibody solution was added, consisting of 3% w/v

Goat's serum/DPBS/0.1%Tween 20 and Vinculin (ABfinity rabbit; Thermo Fisher), on a ratio of 1:200. Samples were then incubated for 1 hour at room temperature, light protected. Further washing with DPBS/0.1%Tween 20 preceded the addition of the secondary antibody (Alexa Fluor 488, donkey anti-mouse antibody; Life Technologies) which was prepared and incubated under the conditions described for the primary antibody. The washing process was repeated and a solution containing phalloidin-tetramethylrhodamine B isothiocyanate peptide (Sigma Aldrich) and DPBS/0.1%Tween 20 (1:1000 ratio) was applied for 30 minutes, at room temperature and light protected. After a washing cycle, the 4′,6-diamidino-2-phenylindole (DAPI; Sigma Aldrich) was added and incubated at room temperature, light-protected, for 1 hour. Finally, samples were washed with DPBS/0.1%Tween 20 once, followed by DPBS wash step.

A second set of samples was stained to detect collagen type 1, the actin filaments and the nucleus. After fixation and washes as in the previous staining, samples immersed in 2%v/v bovine serum albumine/DPBS/0.1%Tween 20 and incubated for 30 minutes at 4°C. A primary antibody solution was added, consisting of DPBS/0.1%Tween 20/anti-collagen 1 antibody (ab34710, Abcam plc) on a ratio of 1:1000. Samples were then incubated for 3 hours at 4°C. Further washing with DPBS/0.1%Tween 20 preceded the addition of the secondary antibody Goat Anti Rabbit IgG H&L Alexa Fluor®488 (ab150077, Abcam plc). Samples were incubated at room temperature protected from light for 1 hour. The washing process was repeated, and the staining of the actin filament and the nucleus proceeded as previously explained. Samples were imaged using confocal microscope (Nikon A1+; Nikon Instruments) with an immersion lens with 40x magnification. Images were acquired using the NIS software and utilising predefined channels, DAPI, Alexa 488 and Alx568 for DAPI, vinculin and collagen type 1, and phalloidin respectively.

3.1.8.6 Cell fixation for SEM

The SEM analysis was performed at day 1, 7 and 21. The cell media was aspirated, specimens washed with DPBS and fixed with a solution of 2% Glutaraldehyde (TAAB Laboratory and Microscopy) for 10 minutes followed by two immersions of 15 minutes in Sorensen's Phosphate Buffer (TAAB Laboratory and Microscopy). Samples were then rinsed in DPBS and submitted to a dehydration process. Observation was performed as in 3.5.1.3.

3.1.8.7 Osteogenic differentiation assessment

Osteogenic differentiation was assessed through the production of Alkaline Phosphatase (ALP). Culture media was removed, samples washed with DPBS and fixed as demonstrated in 3.1.6.5. A double washing step with DPBS was performed followed by alkalinisation with Water/0.1MTris solution (Sigma Aldrich). The alkaline solution was removed and replaced with 1ml of liquid yellow ALP solution (Sigma Life Science). The solution was incubated for 30 minutes at room temperature and light–protected, then 100 µL were taken from each well and pipetted into a 96-well plate (in duplicate) to quantify the ALP activity. The reading was performed at 405 nm, with a standard curve created for calibration by placing different concentrations of 0.1MTris/ALP into a 96-well plate.

3.1.8.8 Alizarin red staining

Samples used for ALP measurement were washed in DPBS twice and stained with 1mL of Alizarin Red (AR) solution (Sigma Aldrich) and incubated at room temperature for 15 minutes. Samples were washed with deionised (DI) water multiple times and dried overnight. Imaging of the samples was performed on a stereomicroscope equipped with a digital colour camera (Leica Microsystems). The images were acquired using the supplier software (LAS; Leica Microsystems). Quantification of Ca deposition at the surface of samples was performed with X-ray Photoelectron Spectroscopy (XPS) (Thermo Scientific K-Alpha XPS spectrometer). The samples were mounted on a clean stainless-steel plate and immobilised using copper clips. The survey scans were acquired with 0.4 eV steps, Pass Energy 150 eV, a dwell time of 10 ms and averaged over 20 scans. The spectra were repeated at three analysis positions on each sample (diameter of 400 µm) with non-overlapping analysis areas. Data analysis was performed with the CasaXPS software.

3.1.8.9 Alcian Blue staining and sulphated glycosaminoglycan quantification (sGAGs)

The alcian blue stock solution was prepared according to standard protocols. First, acetic acid (Sigma Aldrich) was added to DI to attain a concentration of 3% v/v and an acidic pH of 2. Alcian blue powder (Sigma Aldrich) was mixed in it to obtain a final concentration of 1% w/v. Samples were washed in DPBS twice, stained with 1 mL of the prepared alcian blue solution and incubated at room temperature for 20 minutes. Samples were then washed with deionised water multiple times and dried overnight. Imaging was performed as described in 3.1.8.8. Estomation of sGAGs was achieved by immersing the scaffolds in 1 ml of 6 M

guanidine -Hydrochloric acid (HCl) solution (Thermo Fisher), prepared according to supplier instructions. Samples were incubated at room temperature for 3h, and manually shaken every hour for a period of 10 minutes. From each well, 200 µL were pipetted in duplicate onto a 96-well plate, and the reading performed at 630 nm, using the protocol defined in 3.1.6.7. A calibration curve was created to allow the estimation of sGAGs per cell number. The procedure was based on the protocol provided Biocolor Ltd, for the staining using Blyscan Blue. Chondroitin sulphate (Sigma Aldrich) was added to water on a 100 µg/ml to create a stock solution that was then diluted to obtain different concentrations of sGAGs. Briefly, 100 µL of chondroitin sulphate solution from each concentration were pipetted into a 1.5 ml eppendorf and 1 ml of alcian blue (prepared as described above) added. The mixture was manually shaken for 30 minutes and spun in a microcentrifuge (accuSpin Micro 17, Fisher Scientific) for 10 minutes at 1200 rpm. Next, the alcian blue solution was gently poured out, and the excess of alcian blue in the walls removed to avoid overestimation of values. To dilute the alcian blue bound to the sGAGs, 0.5 ml of 6 M guanidine solution were added, incubated for 10 min at room temperature and then centrifuged at 1200 rpm for 5 minutes. For the absorbance reading, 200 µL of the supernatant were pipetted in duplicate into a 96-well. The equipment and protocol for the reading were the same as described above.

3.1.9 Statistical analysis

The collected data was analysed with the software Graph Pad Prism 7 and expressed as a mean with a deviation taken as measure of group variability. Mean values and standard deviations were calculated from 3 samples per time point, including the positive control, with exception of the mechanical properties as printed where n=5. The results analysed using 2-way ANOVA with Tukey post-hoc multiple comparison, for levels of statistical significance of $p< 0.05$ (*), $p< 0.01$ (**), $p< 0.001$ (***) and $p< 0.0001$ (****).

3.2 Developed materials and methods - PLLA/AW biocomposite filament for FFF printing – particle and fibre reinforced

The AW precursor described in 3.1. was used as a filler on a 5 wt%, under particle and fibre form (supplied by GTS under proprietary intellectual property terms). The average ± SD values for powder particle size was14 µm ± 1 µm and the average fibre length was 560 µm ± 236 µm and fibre diameter 87 µm ± 5 µm. As matrix, medical graded PLLA introduced in 3.1 was used.

3.2.1 Material blending and filament fabrication

The material processing is shown in figure 22 (Melo *et al.*, 2019). The PLLA granules and AW were mixed inside an Al mould to form rods measuring 200 x 3 x 4 mm. The rods were then pelletized to created granules that were fed into a twin-screw extruder (Rondol Technology Ltd, United Kingdom) to produce a homogeneous filament. For the extrusion process, a maximum temperature of 190 °C was applied, then reduce to 160 °C at the die. The extruded material was inserted in a haul-off machine at 0.7 mm/s, at a feeding speed of 20 ± 5 rpm and an extrusion speed of 60 ± 10 rpm. The resultant filament diameter was 1.6 mm ± 0.2 mm.

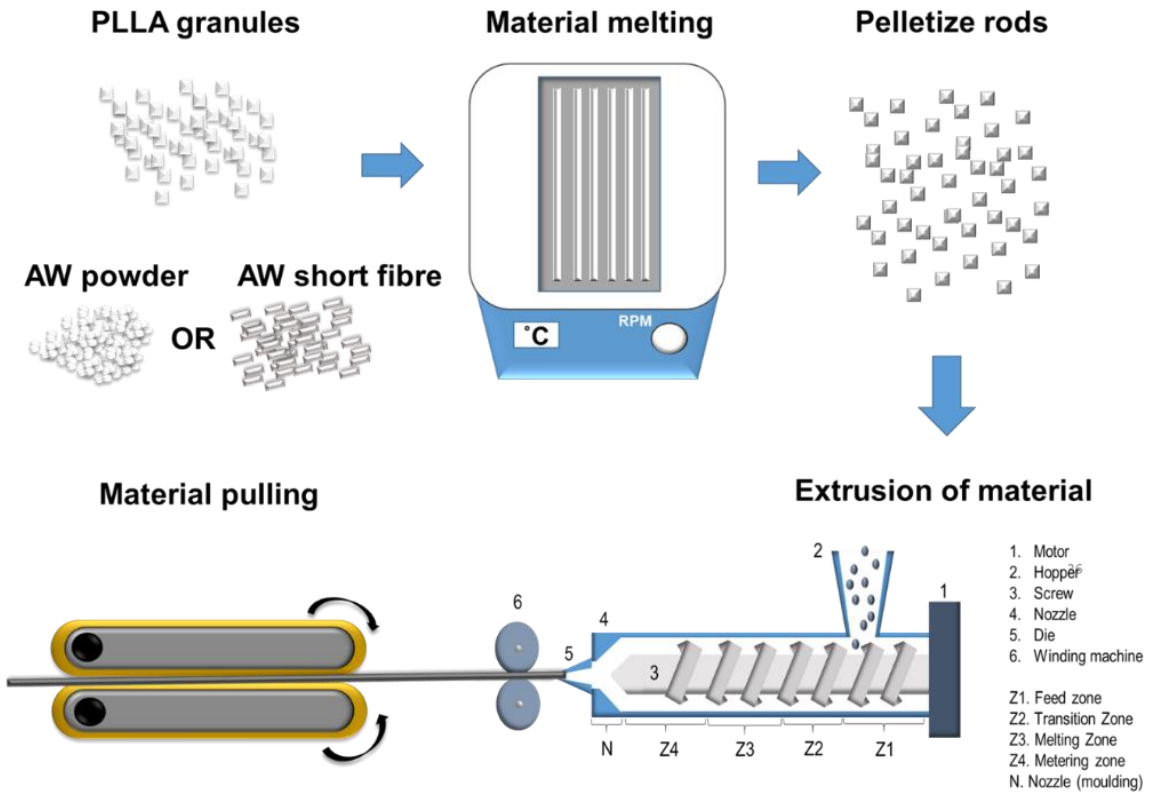

Figure 22 – PLLA and biocomposite filament preparation. Raw materials are blended inside a mould to produce biocomposite rods. The rods are pelletized and used as feedstock of a twin-screw extruder to process the final biocomposite filament. Material is pulled by a haul-off machine to tailor the filament diameter.

3.2.2 Sample preparation: FFF

As previously explained on chapter 2, section 2.6, the AM process starts with the drawing of the part using CAD. The CAD file is then converted into a .stl file and transferred to the

printer software where it can be read by the 3D printer. The FFF process is represented on figure 23 alongside the scaffolds design and dimensions. Briefly, the scaffolds were designed as woodpile structures using Autodesk Inventor (©Autodesk Inc.), using a 0/90 laydown pattern. Two types of samples were created, squared for structural, chemical and biological characterisation, and bar shaped for 3-point bend, before and after degradation. Both sample types contained a pore size of 1 mm, the same for the beam size. Squared samples measurements were 10 x 10 x 2 mm (correspondent to width, length, height). Bar shaped samples measured 10 x 40 x 3 mm. The .stl file of the scaffolds was then exported into the printer's slicing software (CraftWare, CraftUnique Ltd) and the printing parameters defined as 0.7 ±0.1 mm extrusion width, 0.2 mm layer height and 30 mm/s of draw speed. The filament prepared in 3.2.2.1 was fed into the printer (Craftbot 2, CraftUnique, Hungary) and pushed into a nozzle heated to 230 ˚C. The molten filament was selectively deposited onto a building platform, heated at 60 ˚C, on a layer by layer fashion. Each part was printed individually to avoid failure from filament discrepancies and no post processing or supports were needed.

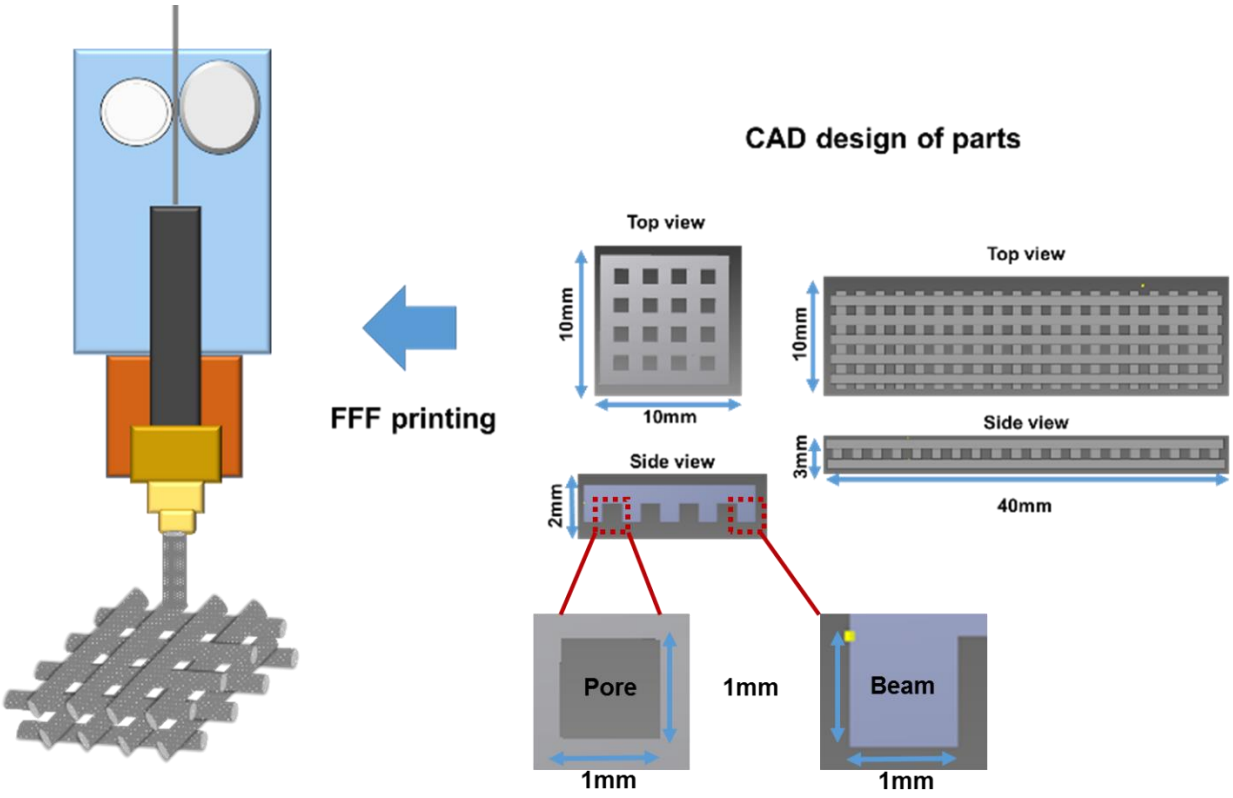

Figure 23 - Scaffold design and processing via FFF printing. Biocomposite filament is selectively deposited onto a heated building platform on a layer –by-layer fashion. Two types of samples were created, with a design consisting of on 1 mm pores and 1 mm beams. Beams were deposited on a 0/90 laydown pattern, favourable to attain a plate shaped structure.

Chapter 4. Design of alumina doped apatite-wollastonite powders: effects in processing, microstructure and mechanical properties of pellets

The aim of this work was to evaluate the effects of alumina (Al_2O_3) on the crystallization process of AW, and its implications on the sintering of green parts. To study the effects of alumina in the crystallization, five types of AW formulation have been investigated, two surface doped AW powders with 0.68% (M1) and 0.14% (M2) alumina respectively, a pure AW (M3), and two bulk-doped with alumina on a percentage of 0.2 wt% (M4) and 0.61 wt% (M5).

4.1 Results

4.1.1 Elemental analysis of AW batches

The XRF analysis is represented on table 12. All main components of AW powder are present, with some minor contaminants such as potassium oxide (K_2O), ferric oxide (Fe_2O_3), strontium oxide (SrO), and zirconia oxide (ZrO_2). Alumina was also detected for both M1 and M2 batches, however with an amount 5 times higher for M1 batch, compared to M2. As expected for the doped batches, the percentage of alumina was within the target range planned for the initial composition. Fluorine (F) was not detected in this analysis despite its inclusion in all batches.

Compound	M1	M2	M3	M4	M5
MgO	3.72	3.68	4.09	5.23	4.24
Al_2O_3	0.68	0.14	0.04	0.20	0.61
SiO_2	33.12	35.49	41.02	46.71	40.78
P_2O_5	13.79	15.47	12.57	9.93	12.99
K_2O	0.03	-	-	-	-
CaO	48.42	44.81	42.21	37.86	41.29
Fe_2O_3	0.09	0.10	0.06	0.06	0.07
SrO	0.02	0.02	0.01	0.01	0.02
ZrO_2	0.01	-	-	-	-
F	-	0.19	-	-	-

Table 12 - XRF results for AW powder batches. All values represented as wt%.

4.1.2 Powder morphology – particle size, shape and size distribution

The particle size of a representative AW sample was assessed by mastersizer (table 13) and SEM (figure 24), following the protocol described in chapter 3.1. Since samples were processed using the same methods, the powder morphology was similar: particles with sharp edges and irregular shape, typical of a glass powder.

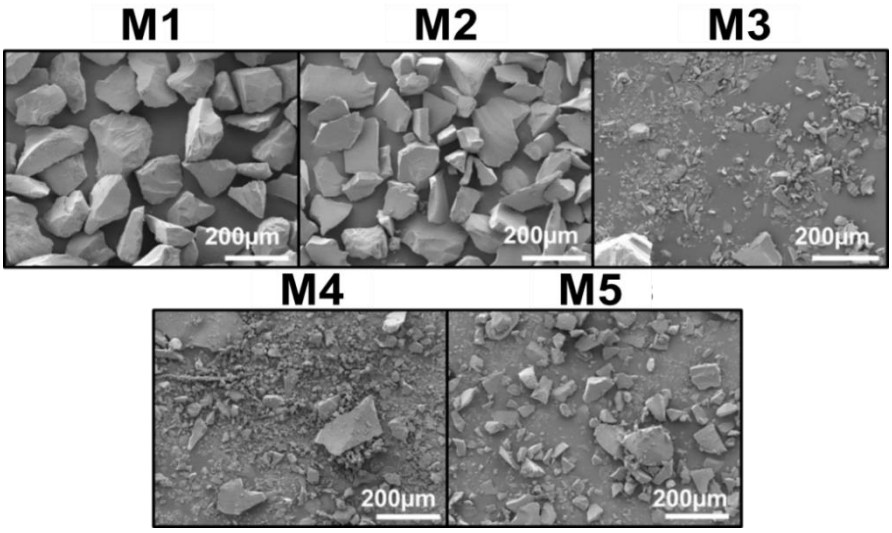

Figure 24 - SEM micrograph of AW powders as received.

According to the results of particle size and size distribution (table 13), obtained for the M1 powder used in HSM, 90% of the particles are below 74 µm, a value higher than the sieve mesh aperture (20 µm). This was attributed to defects on the mesh and to the elongated shape of glass particles. These can be smaller than 20 µm in width but bigger in length. This variety in sizes and shapes for each sieve mesh, is observable in figure 25, where some particles collected from the 20 µm sieve appear to be ≈ 50 µm in width. The long "blade-like" shaped particles are also visible and are pointed by arrows on the represented micrograph. Remaining powders were sieved using the same procedure.

Analysis	Dx10	Dx50	Dx90
M1	3.14±0.5	24.7±3.36	74±8.65

Table 13 - Representative analysis of particle size of M1 powder used for HSM analysis (n=5). Values as mean ± SD.

A powder blend with a maximum particle size of 90 µm was used for the uniaxial compression process (figure 25). Irregular size and shapes were observed on the SEM micrographs, but no measurements were taken.

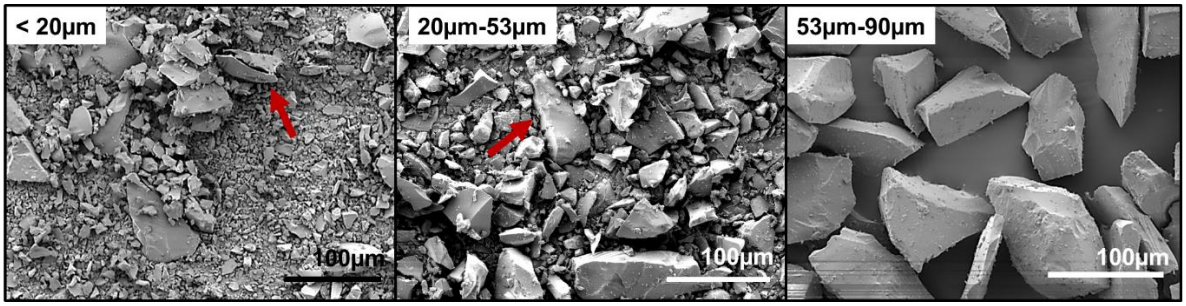

Figure 25 - Representative analysis of powder morphology evaluated with SEM. Micrographs demonstrate the variety of sizes and shapes obtained from each sieve mesh (20 µm, 53 µm and 90 µm). Red arrows pointing the elongated particles capable of passing through sieves with smaller aperture than their major dimension.

4.1.3 Thermal properties

The DSC-TGA graphs are demonstrated in figure 26, with all thermal transitions highlighted, and an example of how the temperatures were taken. Two crystallization peaks were identified for M1 and M2, however for the remaining materials only the second peak was seen. The first peak is related to apatite and the second to wollastonite (A and W), since apatite crystallizes prior do wollastonite (Kokubo *et al.*, 1985; Emad and Van Noort, 2011). Two peaks were also observed for melting in all samples. The temperature corresponding to each thermal transition is shown on table 14. The T_c was present in the form of two peaks therefore the highest temperature was chosen as the centre of each peak for this transition, in the case of M1 and M2, of the second peak (Figure 26e). According to the collected values, similar transition temperatures were obtained for all batches, with T_g, ranging from 748 ˚C to 758 ˚C, T_c from 927 ˚C to 949 ˚C, and T_m from 1258 ˚C to 1270˚C (irrespective of their alumina content). The weight loss with temperature was not significant, lower than 1% for all powders.

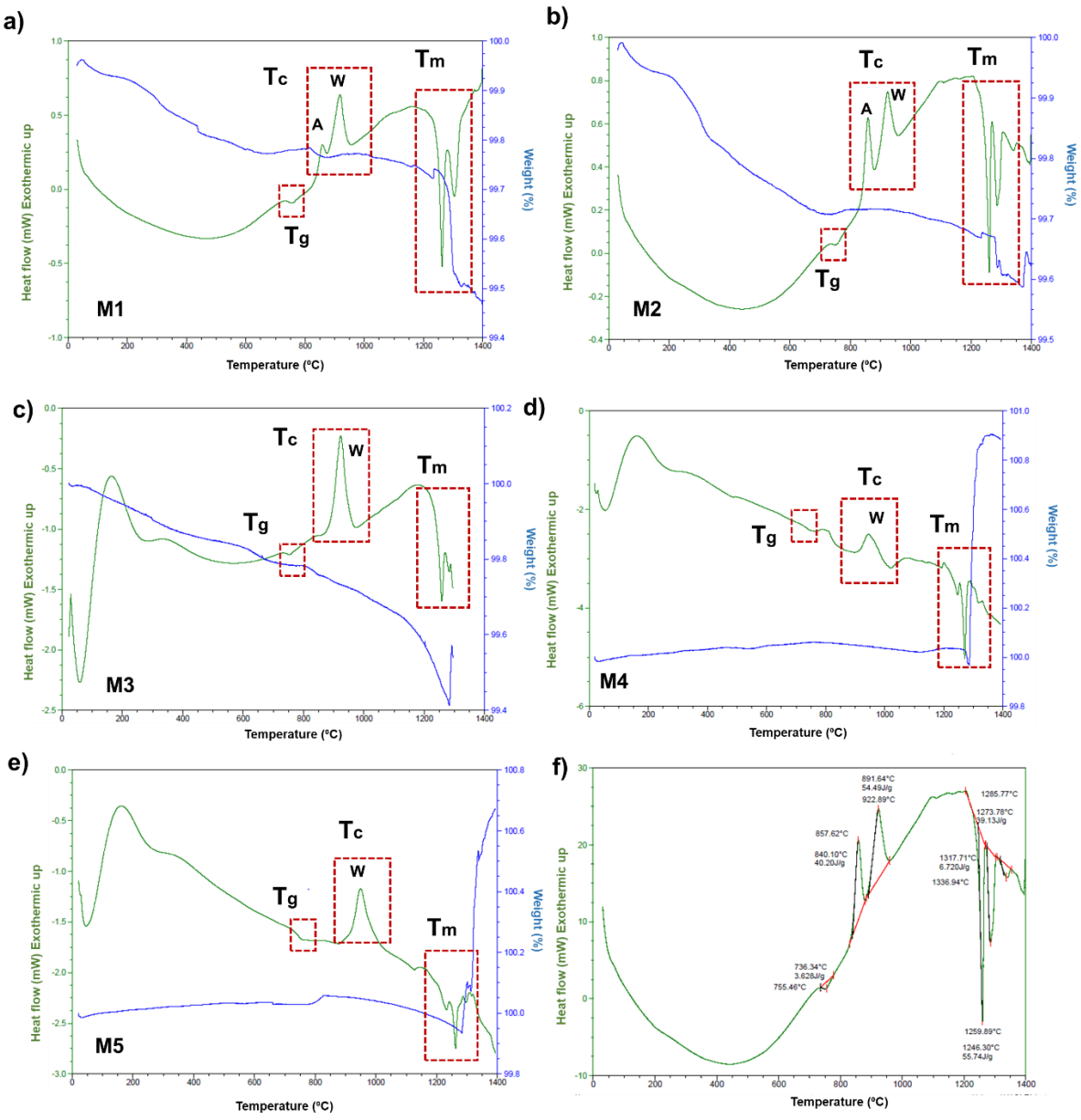

Figure 26 - DSC-TGA analysis of analysed AW powders. a) M1; b) M2; c) M3; d) M4; e) M5; f) method to register transition values on equipment's' software. T_g: glass transition temperature; T_c: crystallisation temperature; T_m: melting temperature.

Batch	T_g (°C)	T_c (°C)	T_m (°C)
M1	756	936	1267
M2	758	927	1270
M3	748	928	1258
M4	752	945	1270
M5	754	949	1262

Table 14 - Thermal transition of AW batches according to the DSC analysis.

Two approaches are taken for the results interpretation, based on the values registered in table 15: 1) when alumina is at the surface of the particle (M1 is compared M2); 2) influence of alumina as a dopant in the glass formulation (M3 is compared to M4 and M5). As the sample's mass was different the analysis was directed towards the H value alone, for a better understanding of these variations. When M1 is compared to M2, the influence on the T_g is not significant, with samples reporting the same value, 0.1 J. The reverse happens for the doped batches where, between M3 and the doped batches (M4 and M5), it increases 3 times with alumina content, going from 0.1 J (M3) to 0.3 J (M4). No difference was seen between M4 and M5. Regarding the T_c, M1 reported an H ≈ 2-fold higher (5.5 J) than M2 (3 J). This tendency was seen for M5, 2 times higher than M3 and M4 (which did not diverge between each other). The energy associated with the melting follows the same trend in both types of comparison: H increases with alumina content, but with a smaller effect than for the T_c.

Sample	**M1**		**M2**		**M3**		**M4**		**M5**	
	ΔH (J/g*)	**H (J)**	**ΔH (J/g*)**	**H (J)**	**ΔH (J/g*)**	**H (J)**	**ΔH (J/g*)**	**H (J)**	**ΔH (J/g*)**	**H (J)**
Tg	1.655	0.061	3.628	0.12	6.32	0.11	13.32	0.32	9.105	0.31
Tc	147.5	5.46	94.79	3.03	178.5	3.03	150	3.6	192.2	6.5
Tm	134.4	4.97	101.59	3.25	58.5	0.99	171.4	4.11	139.9	4.76

*Sample mass: M1: 0.037 g; M2: 0.033 g; M3: 0.017 g; M4: 0.024 g; M5: 0.034 g.

Table 15 - Enthalpy of each thermal transition for studied AW batches H meaning enthalpy.

4.1.4 Sintering behaviour of AW powders

The HSM analysis is represented in figure 27 and highlights the first shrinkage (FS) and maximum shrinkage (MS) points, alongside the thermal transitions obtained from figure 26. The melting temperature was placed at the end of the graph as a representative point because due to equipment restrictions, attaining this temperature range leads to sample spreading and possible damage of the sensors. All batches behave differently (figure 27a), with the minimum and maximum values of sintering percentage attained for M2 (~ 5%) and M1 (~ 20%), respectively. An expansion of 12% is also detected on M1, starting around 1250 °C, within the melting temperature range, absent for M2. M3 reported ~ 17%, similar to M4 and M5, 13% and 14%, respectively. From the data collected from the changes in area (figure

27b), M1 shows an area reduction of ~ 60%, but M2 only ~ 12%. Both M4 and M5 registered ~ 40%, and M3 ~ 60%, higher than the alumina doped batches. The shrinkage mechanism was also studied through the detection and placement of FS and MS points. These transformations happened at the same temperature range for all powders, however the percentage of sintering achieved at that point varied. On figure 27a, all powder batches attain MS prior to a second crystallization, with exception of M2 that later experiences a smaller contraction. This is replicated on figure 27b, where all batches attain their maximum area contraction after the second crystallization, but M2 shows no area reduction past this point.

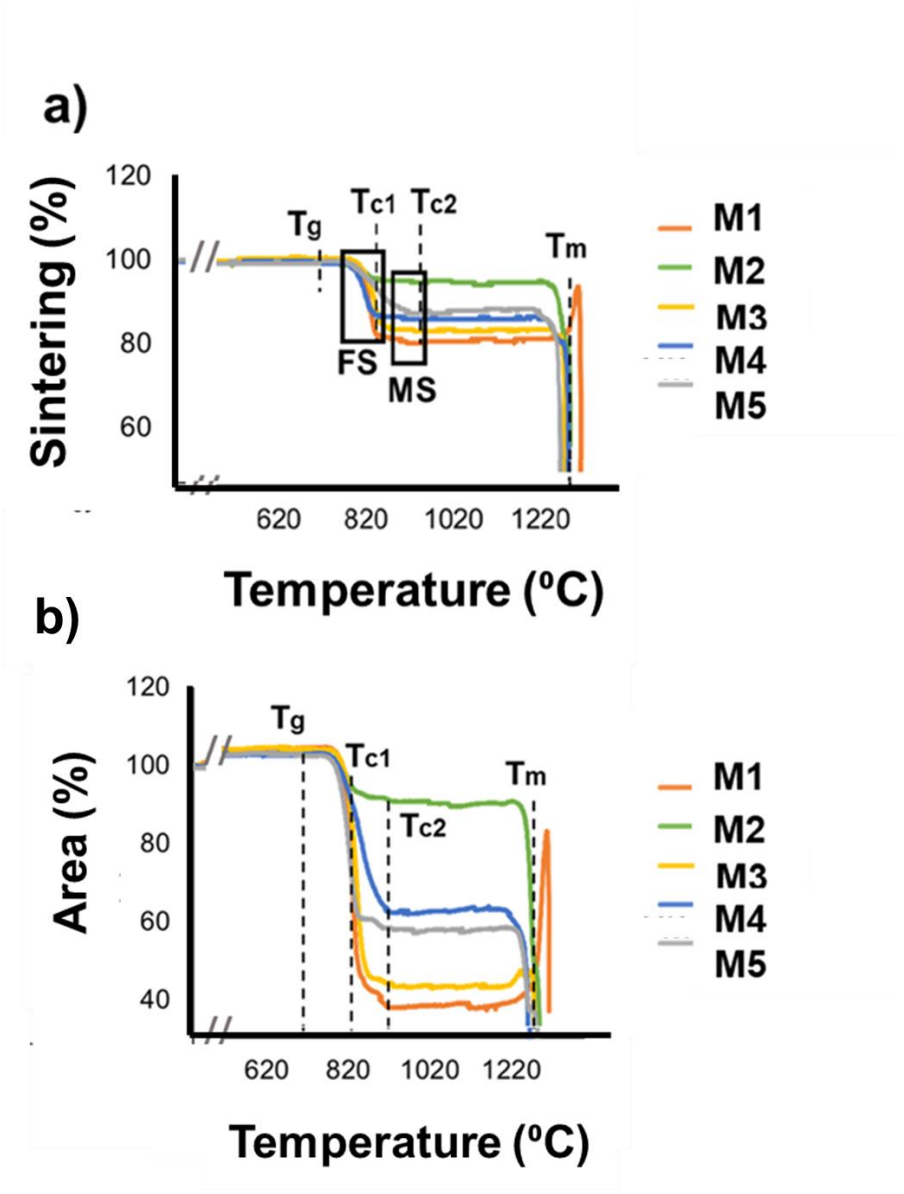

Figure 27 - Sintering analysis of AW batches with particle size range < 20 µm. a) Sintering percentage for each batch and representation of their densification mechanism. Detection of first shrinkage (FS) and maximum shrinkage (MS). b) Variation in area of the sample during sintering. Thermal transitions relatively positioned according to DSC analysis (T_g, T_{c1} and T_{c2} and T_m).

Gathering the data collected on the DSC analysis and the HSM, several important parameters (described in section 2.4.2.2) were studied. Crystallisation tendency (δ), glass forming ability (K_{gl}), and sinterability (S_c) were calculated using equation 7, 8 and 9 (Hrubý, 1972; Lara *et al.*, 2004) (table 16). Briefly:

- the smaller the δ, the higher the ability to crystallise;
- for values below 0.1 the glass forming ability (K_{gl}) decreases, meaning the material is less stable in glassy state;
- higher sinterability, implies that crystallisation is less dependent from sintering.

The values presented in table 16 show that M1, compared to M2, has lower crystallization ability (113.7), higher stability in the glassy state (0.29), and its crystallization kinetics is highly dependent on the sintering process (-45.56). In contrast, M2 has a higher crystallization ability (71.61), being less stable in the glassy state (0.17), with crystallization kinetics highly independent from the sintering (97.69). M3, M4 and M5 did not differ significantly from each other. Most parameters were similar, with exception of sinterability that was -31.52 for M3, -11.68 for M4 and -4 for M5.

	δ	**K_{gl}**	**Sc**
M1	113.70	0.29	-45.56
M2	71.60	0.17	-97.69
M3	134.60	0.37	-31.52
M4	161.30	0.45	-11.68
M5	160.30	0.46	-4.00
Bioglass 45S5*	64.00	0.25	<0.00

Table 16 - Calculated values for crystallisation tendency, glass stability and sinterability. *(Lara *et al.*, 2004)

4.1.5 Crystallinity of powder and sintered samples

The XRD analysis was used to identify the presence of any crystalline phases on the raw material and sintered pellets. According to results showed on figure 28a, all powders, except M1, are amorphous prior to sintering, and no evident crystalline phases can be found. M1 possesses a residual phase which could be associated with its making process. A broad peak centred at 30 ° was observable for all powders (Rodrigues, 2018). For the sintered pellets (figure 28b), according to the used database, three main phases were observed: wollastonite

(▲), whitlockite (*) and diopside (●). M1 presented the weak diffraction of peaks for all phases, and absence of others related to whitlockite (10° and 21°, 2θ), and wollastonite (14°, 2θ). Higher intensities were obtained for the remaining samples with a predominant phase being whitlockite, followed by wollastonite. M2 comprised the highest intensity peaks for the wollastonite, whilst M4 showed the best development of diopside. All phases were collected ICDD Powder Diffraction File 2 Database (2004), ICDD44 Powder Diffraction File 4 - Minerals (2014) and the Crystallography Open Database.

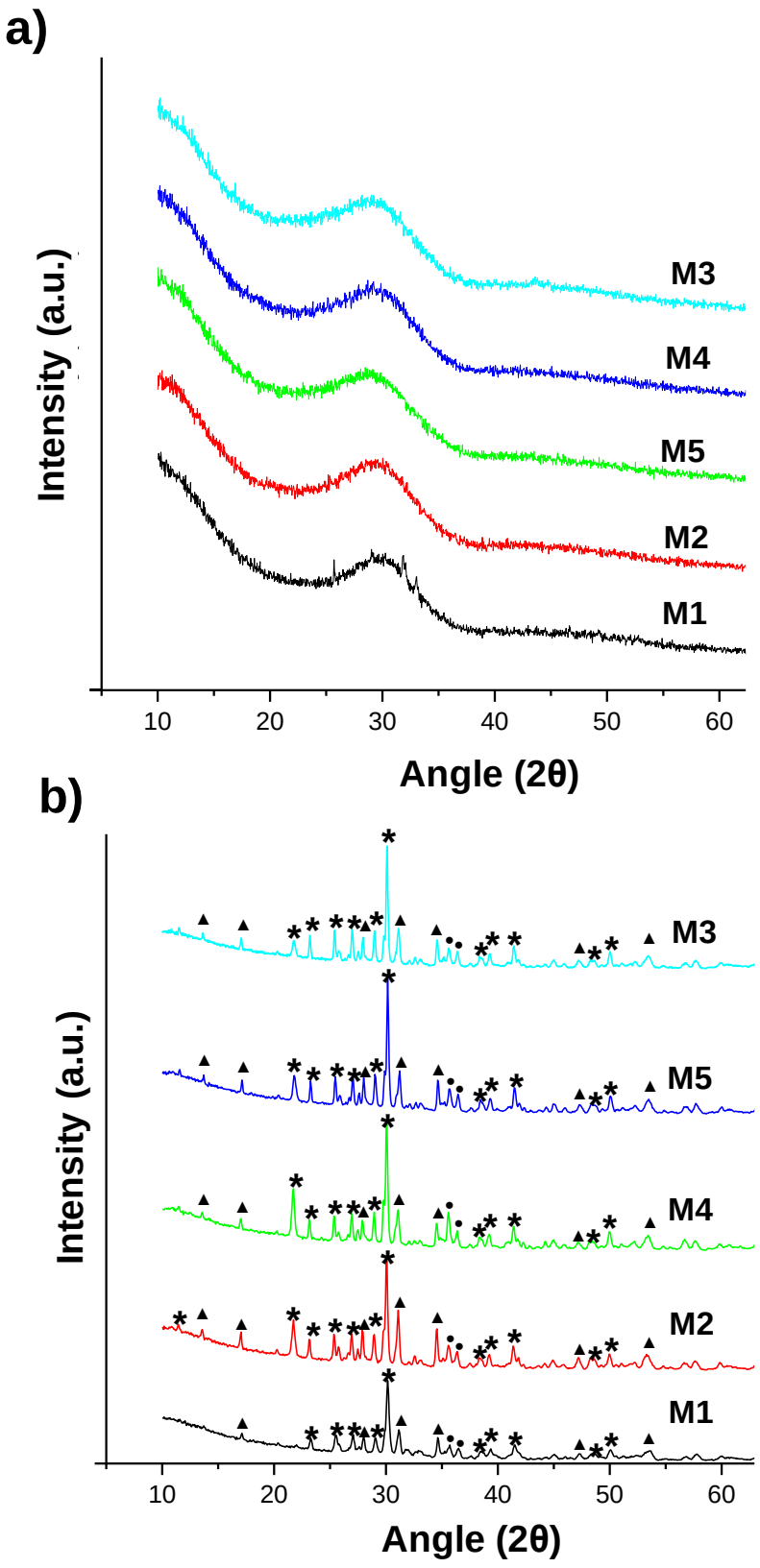

Figure 28 - XRD analysis of AW batches. a) powders; b) sintered pellets. Crystalline phases identified represented with symbols: * for whitlockite, ▲ wollastonite and ● for diopside.

4.1.6 Microstructure of sintered parts

The microstructure developed for each material after sintering was analysed with SEM (figure 29). With exception of M1, all materials produced a crystalline microstructure, consisting of randomly oriented crystals. The crystal size and shape varied, with most crystals presenting either a cubic or pillar shape. The crystal size was not possible to measure due to the uncertainty created by their random orientation, but most appear to be smaller than 10 µm. M2, like M3 presents a crystalline structure, with presence of gaps between crystals. Glassy phase was detected for M5 samples, distributed amongst the crystals and bound to them. A higher degree of necking is observable for M4, compared to M3.

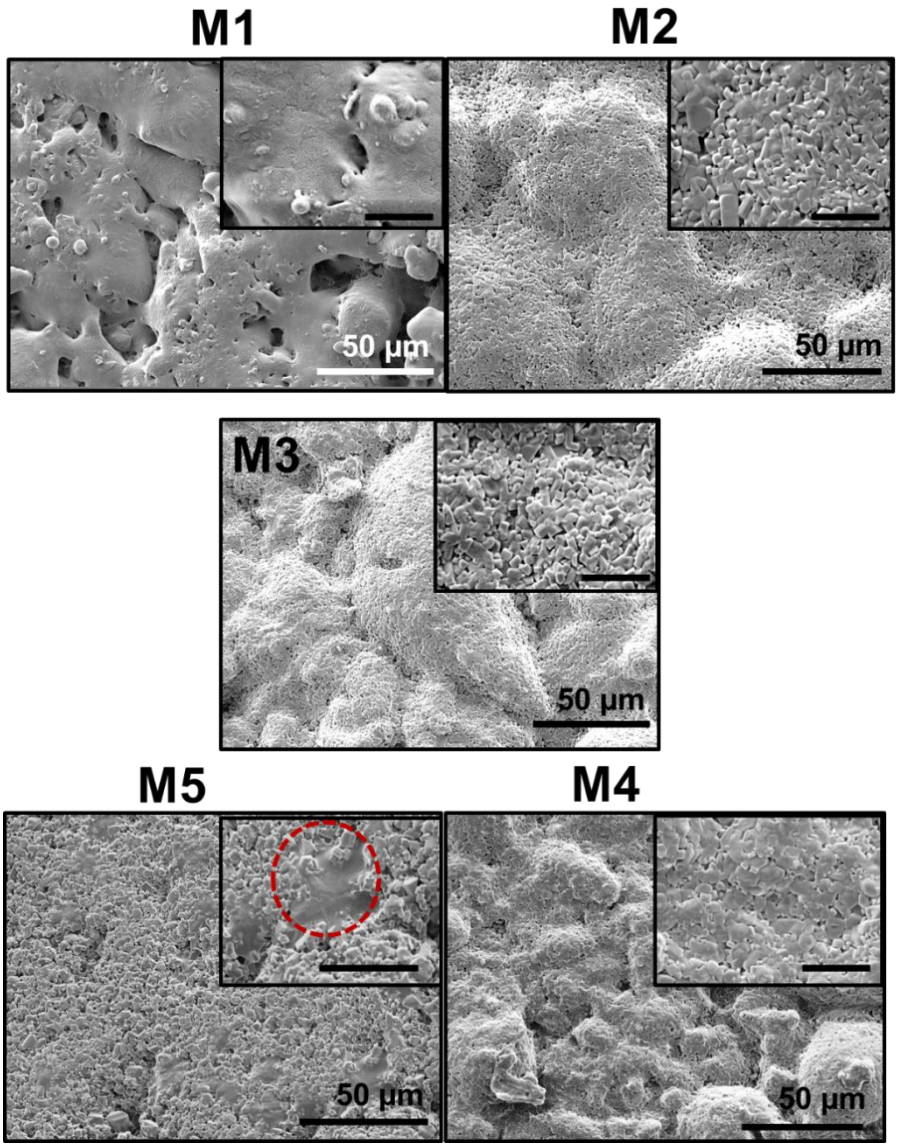

Figure 29 - Micrographs of sintered pellets produced via uniaxial compression. Scale bar on zoomed pictures = 10 µm. Red dashed circle indicating presence of glassy phase.

The density and total porosity of the parts were also calculated and displayed in table 17. According to the results sample bulk density (equation 14) was identical, between 0.57 g/cm^3 and 0.68 g/cm^3. These values are 5 times lower than the ones registered for AW, without accounting for porosity. Total porosity was also similar, with values ranging the 78-81%. From this data it is possible to see that the densest pellet was made with M4, and the least dense with M5. Porosity matches the tendency, with the most porous being the M5.

Material	**Theoretical density (g/cm^3)**	**Total porosity (%)**
M1	0.67 ± 0.02	78.12 ± 0.57
M2	0.65 ± 0.01	78.95 ± 0.32
M3	0.65 ± 0.02	78.81 ± 0.52
M4	0.68 ± 0.02	78.00 ± 0.53
M5	0.57 ± 0.05	81.32 ± 1.75
AW (Alharbi *et al.*, 2015)	3.078	N/A

Table 17 - Calculated density and total porosity of produced pellets.

4.1.7 Mechanical properties

All batches were tested under compression, with for 5 samples of each. The results (figure 30b) show a similar effective modulus between M1 (~ 0.9 GPa) and M2 (~ 1.1 GPa), but a higher compressive strength (figure 30a) for M2 (~ 354 MPa) compared to M1 (~ 145 MPa). M3 and M4 did not differ in modulus but M4 presented a higher strength, ~ 234 MPa versus ~ 96 MPa for M3. Compared to M5 (~ 61 MPa), M3 has a higher value for maximum stress point but the same effective modulus. M4 and M5 were similar in terms of modulus, with M4 presenting ~ 1.3 GPa and M5 ~ 0.7 GPa.

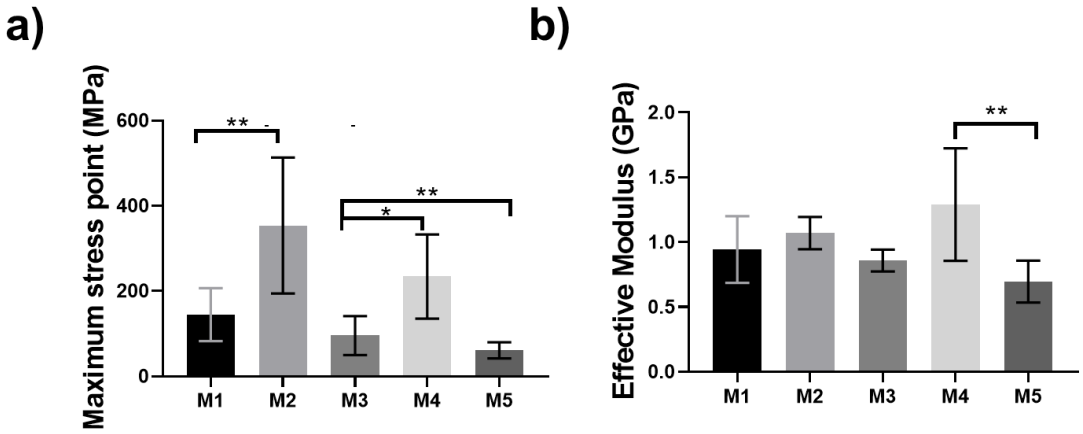

Figure 30 - Mechanical behaviour of samples under compression. a) Maximum stress point in MPa. b) Effective modulus in GPa. Analysis performed for n=5. *denotes significance p < 0.05, ** p< 0.01, *** P< 0.001 and **** p< 0.0001.

4.2 Discussion

The AW powder batches were characterised in terms of thermal, structural and chemical properties. In the raw state, all powders are amorphous (figure 28a) therefore, present no crystalline phases. The particles shape was similar, irregular with sharp edges, typical of glass powders (Lee, 1996; Ganguli and Chatterjee, 1997; Juhasz *et al.*, 2004). The particle size and size distribution were defined prior to analysis to ensure consistency was present, as particle size has proven to influence the sintering process of materials (Butscher *et al.*, 2012; Gomes *et al.*, 2014; Alharbi, 2016; Rodrigues, 2018). According to table 14, the thermal transitions for all powders are within the same temperature range but the enthalpy associated with these differed. To facilitate the discussion, the analysis will be firstly performed separately: i) powders containing alumina at the particle's surface (M1 vs M2); ii) powders containing alumina in their base composition (M4 vs M5) compared to pure AW (M3).

4.2.1 Influence of alumina at the particle's surface

The crystallization process is an exothermic transition where energy is being released from the material and provided to the surroundings. This permits the diffusion of matter and consequently the reorganization of the material's microstructure (Pooria Moghadam, Tohidi and Ranjbar, 2010). As observed in table 15, twice the amount of energy is needed to crystallize M1, when compared to M2. It can be stated that the crystallization process can occur within the same temperature range, but the degree of crystallization attained can differ. This change in crystallization, and amount of each crystalline phase, was visible on the XRD

analysis (figure 28b). Both batches presented peaks referring to the respective crystalline phases, but with higher diffraction for M2. The crystalline character of M1 was confirmed with XRD, but unlike M2, these were not observable with SEM. The absence of a visible crystalline microstructure can infer that these crystals are possibly at the nanoscale. This means that the nucleation happened (perhaps at a smaller level) but the crystal's growth was lower, comparatively to M2. Another factor influencing the disparities in crystal formation is associated with the sintering temperature. J. Park et al. (Park *et al.*, 2010) studied the influence of the sintering temperature in the crystallisation of AW doped with Al_2O_3, and noticed the conversion of apatite crystals into whitlockite above 1000 ˚C. It was also observed that the amount of precipitated β-wollastonite was directly proportional to the sintering temperature. Both phenomena are clearly seen from the XRD spectra of the analysed powders (figure 28b), where apatite was never detected, only whitlockite, also reported for samples sintered at 1200 ˚C. (Chang, Mao and Wu, 2000b). Moreover, the peaks relating to whitlockite and β-wollastonite on M1, sintered at 1150 ˚C, are smaller than for the remaining batches, sintered at 1250 ˚C.

Focusing on the results in table 16, M1 has lower crystallization ability, higher stability in the glassy state, and its crystallization kinetics is more dependent on the sintering. In contrast, M2 has a higher crystallization ability, therefore is less stable in the glassy state, and its crystallization kinetics is independent of the sintering, permitting a faster and abundant crystallisation, before this temperature is reached. This data is in accordance to the DSC analysis where a lower energy is needed to crystallize M2, and to melt it, indicating is less stable in glassy state, searching a natural state of organization.

A study by Baino et al. (Baino *et al.*, 2016) highlights the role of Al_2O_3 and boron oxide on the densification of different bioactive glasses. According to the results, Al_2O_3 doped glasses show a 1-step densification mechanism whilst boron doped glasses present a multi-step densification. The densification of Al_2O_3 doped glasses occurred prior to crystallization, causing a slight increase in the sintering temperature, compared to the one registered in the plateau for MS. The multi-step densification process prevented a maximum densification prior to sintering, leading to an increase in temperature of 100 ˚C, significantly higher than the previously analysed. Based on the HSM data (figure 27a), M2 is crystallizing prior to MS, characteristic of the multi-step densification, whilst M1 seems to follow the 1-step densification route. Al_2O_3 is a glass stabilizer widely used to enhance densification and improving glass stability. In this study, it is assumed that the Al_2O_3 particles derived from ball milling adhere to the surface of the AW particles via impact. Being the crystallization of AW a surface process, it is hypothesised that the Al_2O_3 particles are occupying nucleation sites,

limiting the crystallization process. As a result, the material's ability to crystallize decreases, and it becomes more stable in the glassy state, consequently easier to sinter at lower temperatures. The amount of Al_2O_3 is reduced by a factor of 5 on M2, compared to M1. This translates into a high crystallization ability, and as a result an enhanced crystallinity. During sintering, the early crystallization decreases the number of necking sites available, hindering the densification process, i.e. contraction of the structure. This phenomenon is commonly observed in the clusters model where impurities at the surface of the powder particles can crystallize and decrease overall densification (Oscar, Bellini and Dutra, 2012; Duminis, Shahid and Hill, 2017). The results plotted in 27b show that effect, with M1 reporting an area reduction of 60% and M2 of 20%. Throughout sintering, crystallization induces a stabilisation of the structure, resulting in a more viscous flow. This prevents matter diffusion at the initially determined sintering temperature, demanding a higher input of energy to excite the atoms and lower the viscosity to promote matter diffusion (Baino *et al.*, 2016). This culminates in the increase of sintering temperature, which in this work was translated by a change in the protocol from 1150 ˚C (M1) to 1250 ˚C (M2) (100 ˚C adjustment). The processing route of the material affects the crystallinity, which is important for stress distribution within the structure, principally the presence of defects. The amount, size and orientation of crystals dictates the quantity of stress points, and how cracks spread and grow, known as fracture toughness. The microstructure also relies on the manufacturing methods and post-treatment of the part, therefore several parameters must be accounted for the analysis (Freiman and Hench, 1972; El-Kheshen *et al.*, 2008). Glass-ceramics are brittle materials, and their main strength relies on the quality of their surface. When subjected to loading conditions, micro cracks spread, weakening the part and leading to failure (Emad and Van Noort, 2011). Here, the influence of Al_2O_3 at the surface wasn't crucial for the effective modulus of the created discs, instead its effects manifested on the maximum stress point attained. Despite the similar effective modulus, the compressive strength was higher for M2 compared to M1. Previous studies on $Li_2Si_2O_5$ glass-ceramics reported that the flexural strength of material is dependent of the nucleation time and amount of crystallization attained, whilst the elastic modulus depended only on the crystallization degree (Freiman and Hench, 1972). The increase of the flexural strength was directly proportional to the amount of crystal fraction, provided the proper nucleation time was applied. For insufficient time, the opposite was observed. The nucleation time was identical, but both size and amount of crystals was lower, resulting in a higher amount of glassy phase. The flaws occurred in the glassy phase of the material rather than in the crystalline phases, since cracks propagate freely through the microstructure. M2 presented more crystals when observed on SEM (figure 29), which

limited the amount of free ways for the cracks to propagate. This allowed the material to withstand higher loads before failing (Freiman and Hench, 1972). The type of crystallised phase is also crucial. Previously, the effects of the sintering temperature in the development of crystalline phases on Al_2O_3 doped AW were evaluated (Park *et al.*, 2010). Below 900 ˚C, only apatite developed whilst at that given temperature and above, β-wollastonite was present. Wollastonite is the phase responsible for the improved mechanical properties, which is attributed to the crystal growth and shape. Column shaped crystals appear at the surface and grow inwards, acting as filler to the glass matrix, reinforcing it. At 1100 ˚C, another phenomenon was detected, the presence of whitlockite and increase of β-wollastonite, derived from the conversion process of apatite into whitlockite, which start at 1000 ˚C. Above 1100 ˚C the conversion is considered to continue, and the amount of β-wollastonite is assumed to increase. Here, M1 sintered at 1150 ˚C presented already whitlockite, different from previous studies, where it was sintered at lower temperatures, developing only apatite and β-wollastonite (Kokubo *et al.*, 1982; Alharbi, 2016; Mancuso, 2016; Mancuso *et al.*, 2017; Rodrigues, 2018). M2, sintered at 1250 ˚C presented also both phases, but in higher intesity, reflecting the effects of temperature already described above. This improvement in wollastonite content derived from the higher temperature adopted reflected on the strength values attained, which were significantly higher for M2 ($p< 0.01$). The effective modulus of both materials was similar, even though the materials microstructure was different. This is associated with the high porosity measured (~ 76% to 80%). Here, low densities were attained, (< 0.6 g/cm^3) compared to the one of pure AW, ~ 3.078 g/cm^3 which is 5 times higher. The values obtained are comparable to others in literature (Ahmetoglu *et al.*, 2009; Mancuso, 2016).

4.2.2. Influence of alumina within batch composition

When assessing the thermal properties of the doped AW powders, a direct relation was observed between the amount of Al_2O_3 and the crystallization enthalpy. High content of Al_2O_3 leads to an increase of the crystallization enthalpy, meaning this material is more stable in the glassy phase, therefore needs more energy to promote rearrangement of its structure. The amount of energy involved in the crystallization of M5 is noticeably higher, compared to M3 and M4.

The HSM analysis of the powders (figure 27a) confirmed that the amount of Al_2O_3 did not influence the material sintering ability. Identical sintering percentages were obtained for all doped batches, and M3. For the area reduction the 20% difference was seen between doped batches and M3. This could be related to the presence of glassy phase since it contracts

differently from the crystalline phases, resulting in a different densification of the structure (Freiman and Hench, 1972). Focusing on the sinterability, the doped powders present the highest degree of dependence when relating the crystallization and sintering, supporting the stabilization effect. This stabilization effect did not suppress the crystallization but altered the microstructure of the material. According to the XRD analysis (figure 28b) and the SEM micrographs of the sintered parts of M3, M4 and M5 (figure 29), the microstructure observed relates to a crystalline material, with all phases present in similar amounts. A higher level of necking was observable for M4 when compared to M3, indicating a higher level of matter diffusion, possibly promoted by the Al_2O_3. The presence of Al_2O_3 promotes the formation of liquid phase, which enhances sintering and contributes for the development of crystals (Lee, 1996; Oscar, Bellini and Dutra, 2012). Above 0.14 wt%, Al_2O_3 doesn't promote crystallization but also doesn't hinder it, instead it allows for a higher degree of melting, visible by the presence of glassy phase (figure 29, dashed circle). The effect in the microstructure and part crystallinity directly influenced the mechanical properties, showing a benefit when added on 0.14 wt%, where the MSP was significantly higher than for M4 compared to M3. For M5, the effect was the opposite, and the modulus decreased. This tendency was already observed on 4.2.1, where the amount of glassy phase influences the part's strength, due to its lower density compared to the crystalline phase. Since M3, M4 and M5 were processed using the same temperature, the effects of it on the development of crystalline phases were neglected. The modulus was attributed to the high porosity of the pellets, mimicking the discussion performed in 4.2.1. The values were not statistically different between M3 and M4, however, the values obtained for M4 were higher than M5. This could be associated with the existence of higher among of glassy phase in M5, which leads to a lower density of the material, translating into a lower modulus.

According to the results presented, M4 was the batch with best mechanical properties ($p< 0.01$ for M5 and $p< 0.05$ for M3), whilst keeping the crystallinity of the material. From an industrial point of view, doping AW with alumina could be an advantage compared to inducing a surface contamination. The doping process of glass is repeatable and can be monitored easily, ensuring the quality standards demanded by industry. This type of process is also upscalable, meaning the production can be increased. This would reflect in higher productivity, and wider range of supply, lowering operation costs. Changes in the protocol aren't needed, but the possibility of exploring the processability further is appealing.

4.3 Conclusion

The kinetics and formation processes of glasses and glass-ceramics are complex. It can be influenced by multiple factors such as impurities, temperature, pressure, particle size, shape and size distribution. All these are key to establish the processing parameters and final properties of the manufactured part, influencing its application range (Butscher *et al.*, 2011, 2013). The study of initial batch composition and its sintering behaviour is imperative when making glass, especially when attempting to dope or change their properties. For glass-ceramics, factors such as the crystallisation temperature and dwell times, are crucial to allow crystal growth (Jones and Hench, 2006; Gerhardt and Boccaccini, 2010; Oscar, Bellini and Dutra, 2012), which then reflect in the final microstructure, and consequently in the mechanical properties of the device. When present at the surfaces of the particles, the alumina acted has a crystallisation suppressor by occupying the nucleation sites of the AW precursor particles. When included in the initial batch composition, Al_2O3 decelerated the material contraction whilst allowing for crystallisation. The knowledge acquired in this study led to the conclusion that Al_2O3 can influence the sintering behaviour in different ways, depending on how it is inserted in the process, altering the mechanical performance of parts. When at the surfaces of the particle it benefits the sintering process, allowing the process to happen at lower temperature, leading to less energy expenditure and accelerating the production time. Based on the results, Al_2O3 could be used as dopant for the AW glass, to promote a higher degree of crystallisation whilst maintaining the mechanical properties. Such effects could be explored further to evaluate how the dopant could contribute for the control of crystal growth, and its influence on the material mechanical properties and bioactivity. Furthermore, processing parameters could be investigated in higher depth for doped powder to assess the possibilities to sinter these at lower temperatures whilst maintaining the mechanical strength and crystallinity.

Chapter 5. Binder Jetting of AW implants for bone repair

Based on previous studies, in this chapter it is investigated the influence of crystallization on the physicochemical and biological properties of AW parts, produced with binder jetting printing, and sintering. A powder blend consisting of 70% AW precursor particles and 30% MD was created, focusing on smaller particle size ranges, to promote matter diffusion during sintering. Here we evaluate the influence of the powder blend properties in the printing process, and the resulting green parts. Post-sintering, sample's microstructure and mechanical properties were characterized, alongside the bioactive character. Finally, a biological assay was performed to evaluate the osteoinductive and osteoconductive character of the implants and their influence on of hTERT-MSCs behavior.

5.1 Results

5.1.1 Elemental analysis of AW powder

The initial composition of the AW used matched the one developed for M3, however, after XRF analysis (Table 18) it could be seen it suffered changes. Table 18 and shows all elements present in the AW powder provided for the binder jetting process. The result showed that this powder is similar to M2, studied in the previous chapter, and therefore is expected to behave in the same way. The elements found match the ones in the initial formulation, with exception of alumina with 0.13 wt%. Minor contaminants such as potassium oxide (K_2O), ferric oxide (Fe_2O_3) and strontium oxide (SrO) are also present but in percentages smaller than 0.1 wt%.

Compound formula	AW
MgO	3.59
Al_2O_3	0.13
SiO_2	35.19
P_2O_5	16.59
K_2O	0.02
CaO	44.31
Fe_2O_3	0.09
SrO	0.02
F	0.18

Table 18 - XRF analysis of AW used to print binder jetting implants. Values presented as wt%.

5.1.2 Thermal properties and weight loss

The thermal transitions of the AW powder were obtained by DSC analysis (figure 31a) and their values shown in table 19, alongside the calculated ΔH and H. The values obtained were: 754 ˚C for the T_g, 928 ˚C for the highest T_c, and 1266 ˚C for the T_m. The enthalpy associated to the described thermal transitions demonstrates that crystallisation is the process involving more energy, with a total of 3.65 J (both peaks summed). For the T_g and the T_m, the values calculated were lower, 0.27 J and 2.32 J, respectively. The values obtained for the thermal transitions replicate the ones obtained in chapter 4. Concurrently the weight loss was analysed and recorded as less than 1% (figure 31b).

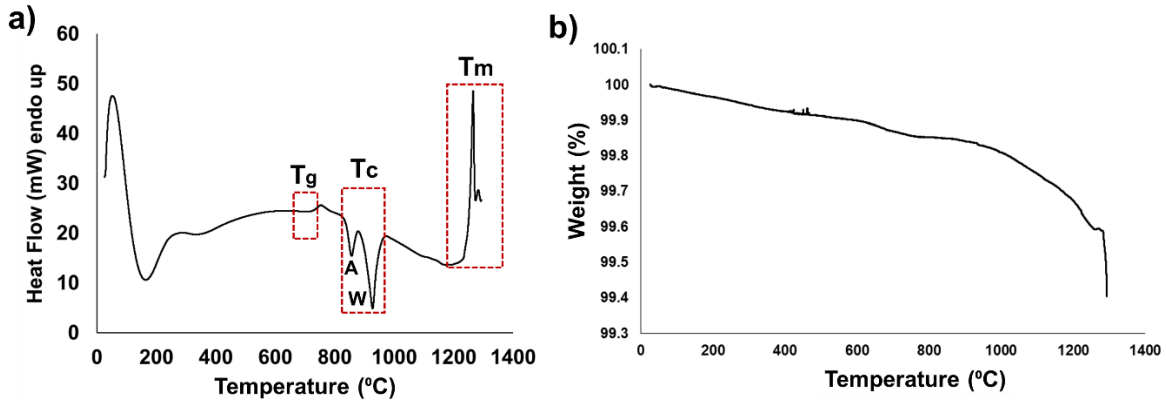

Figure 31 a)Differential scanning calorimetry of AW powder. b) TGA analysis.

	T_g	T_c		T_m
Temperature (˚C)	754.00	857.00	928.00	1266.00
H (J/g)	8.85	25.02	92.26	75.36
H (J)	0.27	0.78	2.87	2.34

Table 19 - Thermal transition and energy associated with them based on the DSC analysis. Enthalpy (H) calculated using sample mass (J x g): 0.031g.

5.1.3 Powder blend morphology – particle size, shape and size distribution

The analysis of the powder blend morphology was assessed using mastersizer and SEM. Particle shape, size, and size distribution were evaluated for both AW and MD powders, in order to ensure the final blend contained the desired morphology. According to figure 32, and as previously investigated in chapter 4, AW particles have sharp edges, and display an overall irregular shape. MD particles are also irregular in shape but with rounder edges. The particle size of each interval defined for the blend was recorded in table 20.

The analysis shows that most particles are within the desired size range, with only 10% being above ~ 100 µm (Dx90), and 10% below ~ 1.10 µm (Dx10). This could derive from the particles elongated shape and potential sieve mesh defects (also seen in chapter 4).

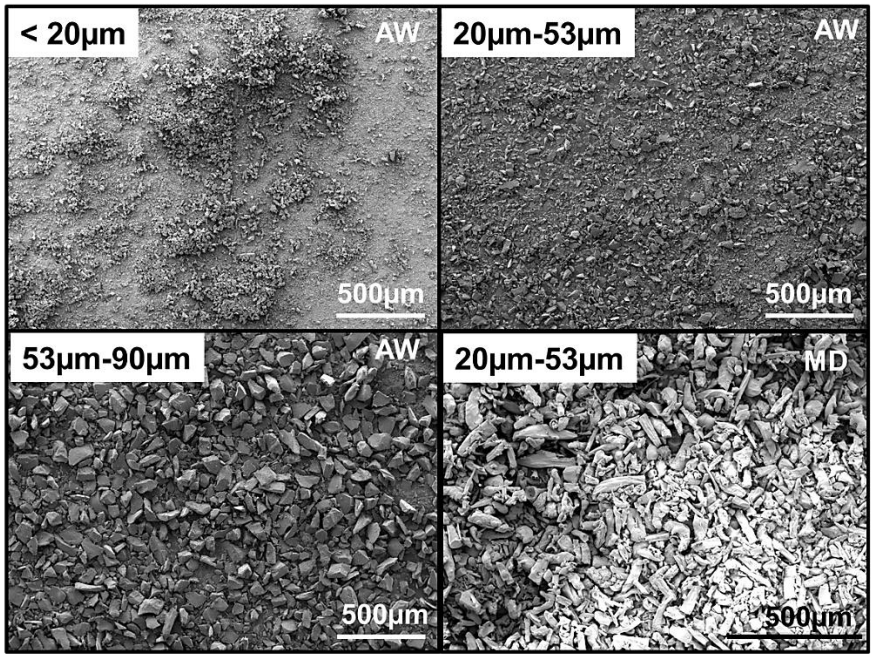

Figure 32 - Representative analysis of AW and MD powder morphology evaluated with SEM. Powder collected from each sieve (20 µm, 53 µm and 90 µm).

Analysis	Dx10 (mean ±SD)	Dx50 (mean ±SD)	Dx90 (mean ±SD)
> 20 µm	1.10±0.98	14.30±0.96	53.80±1.75
20 µm - 53 µm	12.90±0.13	47.60±0.21	103.00±0.34
53 µm - 90 µm	48.20±0.72	87.50±0.80	144.00±0.83
MD 20 µm - 53 µm	21.50±0.84	49.80±1.73	100.00±5.11

Table 20 - Particle size analysis of raw materials composing the powder blend. Particle size intervals for AW and MD analysed individually (n=5). The size distribution was estimated using the Dx values, Dx10, Dx50 and Dx90 which indicate the amount of sample under a certain size (µm) (Malvern Ltd, 2019).

5.1.4 Powder blend sinterability and volumetric changes

The sintering ability of the powder blend was evaluated for each size interval separately. Also known as softening analysis, both sintering percentage and area variation were collected to assess how the material expands and contract with heating. The maximum sintering percentage and area reduction percentage (figure 33) were achieved for particles within the 20-53 µm size range, **~** 20% and **~** 40%, respectively. The lowest value for both sintering and area reduction was recorded for particles within the 50- 90 µm, **~** 5 % and **~** 10% respectively. From both figures it is also observable that first shrinkage happens at similar temperatures for < 20 µm and 20-53 µm intervals, and later for 53-90 µm. The same is translated for the maximum shrinkage, which was associated with T_{c1} for the lower size intervals, and attained only after T_{c2} for the higher range, 53-90 µm (figure 33, right).

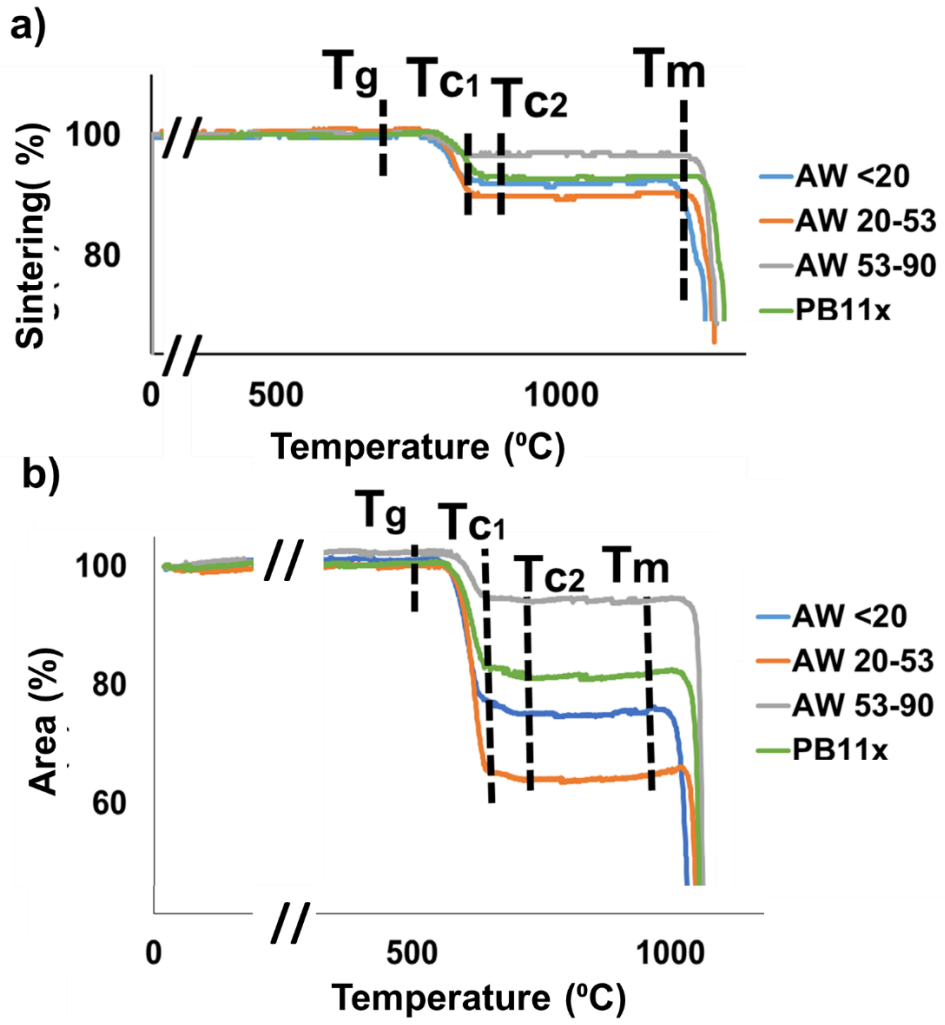

Figure 33 - Sintering analysis of powder blend by size range. Left: sintering percentage. Right: area variation. Thermal transitions collected from DSC analysis indicated in graph.

5.1.5 Powder bed properties – density, packing and flowability

The powder blend printability was evaluated using 4 parameters: Carr index, Hausner ratio, angle of repose and bed density (table 21). The Carr index obtained for this powder blend was 27%. This is corroborated by the Hausner ratio value of 1.37, which reflects a fair flowability. The AOR is also within the fair flow range, which was expected from the previous parameters (Huang *et al.*, 2013). The bed density was determined as 1.31 g/cm^3, closely one third of the value registered for AW particles, 3.078 g/cm^3.

Carr index (%)	Hausner ratio	Angle of repose (˚)	Bed density (g/cm³)
27.00±2.00	1.37±0.04	35.40±5.60	1.31±0.07

Table 21 - Powder bed properties determined for a total of 5 samples. Results displayed as mean ±SD.

5.1.6 Printing quality and part dimension accuracy

The printed structures presented a rough surface and were mechanically weak (figure 34a). This made them difficult to handle, and take measurements using callipers. Instead, samples were placed on a flat surface and a ruler used as reference. Sintered discs (figure 34b) were easy to handle, with parts presenting a good structural integrity and firm when manually pressed. To allow a degree of comparison, these samples were also placed on a flat surface, and measured with a ruler. According to the CAD file (previously shown in section 3.1.2.2), the discs diameter was 12 mm, which after printing appears to be ~ 10 mm. After sintering, the parts shrank to ~ 8 mm.

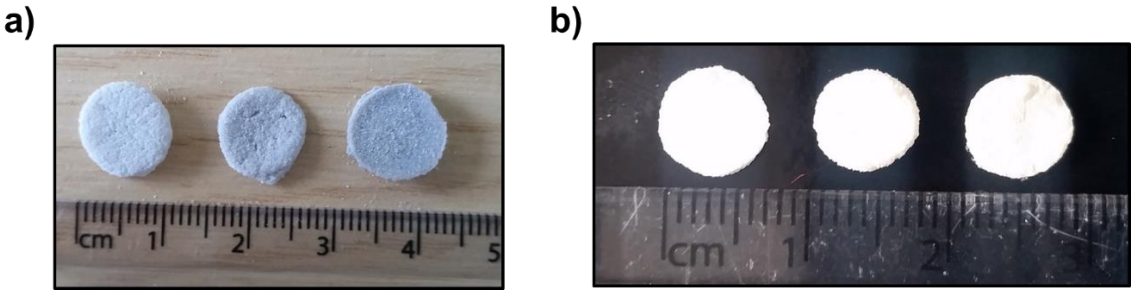

Figure 34 - Printed and sintered AW discs. a) Green parts. b) Sintered parts. Ruler spacing: 1 mm.

On figure 35, are presented examples of failed green parts (prior to sintering). The bars were broken during handling, a result of weak structure integrity (figure 35a). The discs are an example of layer dragging, which caused the top layer to slide towards the end of the building platform, pulling the previous layer laterally (figure 35b).

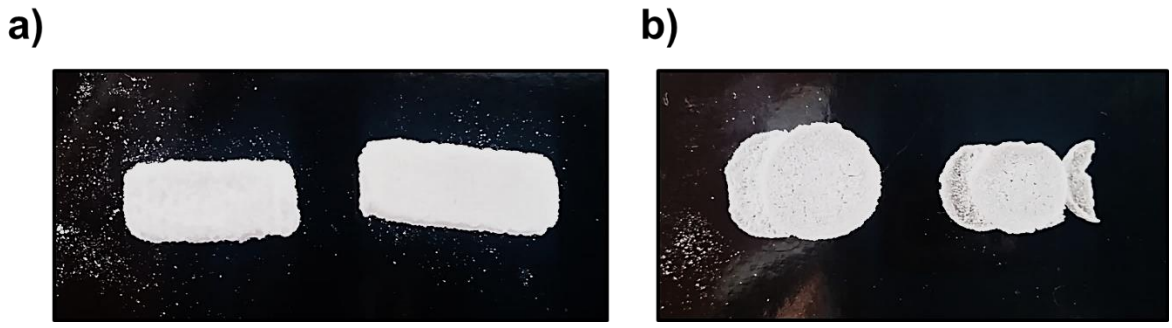

Figure 35 - Representative failed prints. a) Broken bar showing poor structural integrity. b) Discs reporting the results of layer dragging.

5.1.7 Structural properties of printed parts

The printed parts were firstly evaluated in terms of shrinkage, density and porosity (table 22). The mean bulk density of the discs was 2.1 g/cm^3, nearly double the powder bed density and 1.5 lower than AW's density (3.078 g/cm^3). Volumetric and linear shrinkage were also evaluated, (x,y) for the diameter and (z) for the height. Volumetric shrinkage was ~ 59%, which is within the value registered for the < 20 µm and 20-53 µm particle size ranges (figure 33, right). It is realised that samples shrink more in (x,y) than in (z), ~ 28 % and ~ 21 %, respectively. The part mean total porosity was ~ 32%, and the open porosity ~ 4.6% (Archimedes). Pore size was and size distribution were studied and plotted in figure 36. The sample was divided in 3 areas (figure 36a) to ensure an even distribution of the pore size calculation throughout the samples. The values obtained (figure 36b) show a mean pore size of ~ 84 µm, ~ 89 µm, ~ 77 µm, for top, middle and bottom, respectively. Statistically, no significant differences were found.

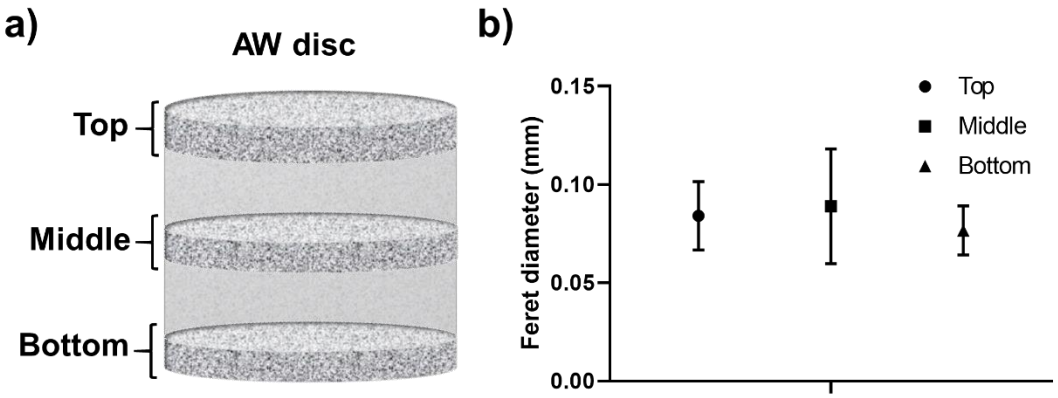

Figure 36 - Pore size measurement schematics and results obtained, for sintered AW discs. No statistical difference found. a) Illustration of measurement areas classified as Top, Middle and Bottom, each based on 5 images. b) Measurement of pore size via Feret diameter, obtained using imageJ.

Bulk density (g/cm^3)	Volumetric shrinkage (%)	Linear shrinkage (x,y) (%)	Linear shrinkage (z) (%)	Open porosity (%)	Total porosity (%)
2.1±0.1	59.2±3.0	27.9±3.9	21.4±4.2	4.6±1.5	32.3±4.0

Table 22 - Properties of the parts after printing and sintering. Results expressed as mean ±SD for n=5.

To visualize the sample microstructure, including the porosity, SEM micrographs were taken (figure 37). The first evaluation compares the part microstructure in the green state and after sintering. The top of the samples is identical, which corroborates the values obtained for the open porosity (table 22). The part cross-section shows that internally, the green part is more porous, but the sintered part shows a higher degree of interconnection. Large holes can also be spotted prior to sintering. Most pores observed for the sintered part appear to be smaller than 200 µm, which agrees with the information obtained from the image treatment (figure 36b). Developed crystals with different sizes are observed on the sintered part, most of them with a size below 5 µm. No crystals are observed on the green part.

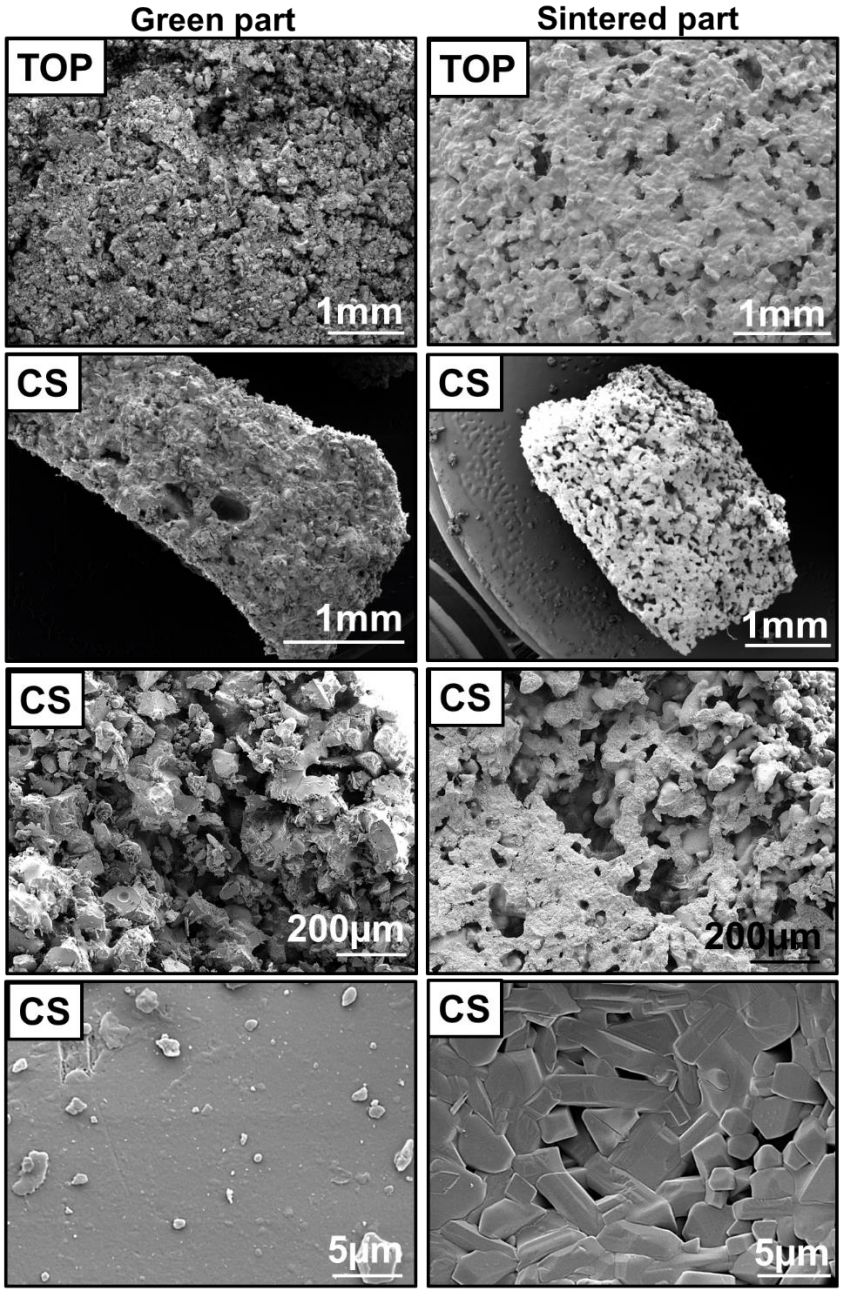

Figure 37 - Micrograph of printed bar on green state (prior to sintering) and sintered. Images of top and part cross-section show an overview of the open porosity and total porosity. Zoomed micrographs report the absence of crystals on the green part, and their presence on the sintered part.

5.1.8 Mechanical properties of sintered AW bars

The mechanical properties of the printed parts were evaluated using 3-point bend test using the bar shaped samples demonstrated in figure 38a. The resultant plot displays the stress vs strain relationship (figure 38b), where different failure points can be seen for all tested samples. The calculated values were collected and reported in figure 38c. The mean value for maximum strength was 18.8 MPa, with the maximum value attained being ~ 27.8 MPa. These

are lower compared to cortical bone (50 MPa) (Hench, 1991). The elastic modulus reported for the bars was ~ 1.4 GPa, which is within the range for cancellous bone (< 0.8 GPa), but significantly lower than cortical bone (> 7 GPa).

a)

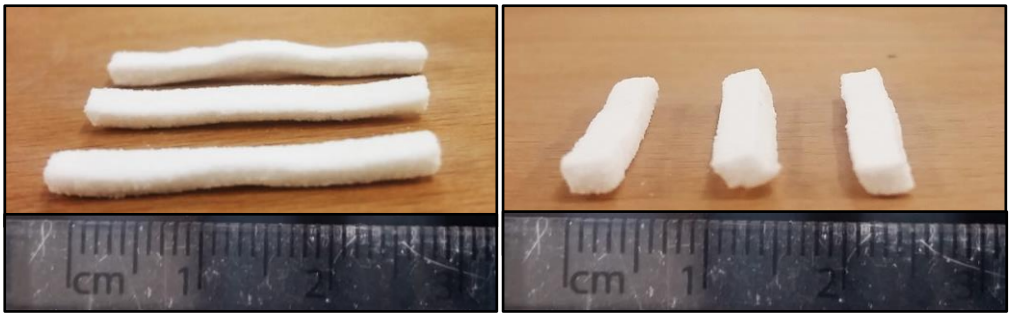

b)

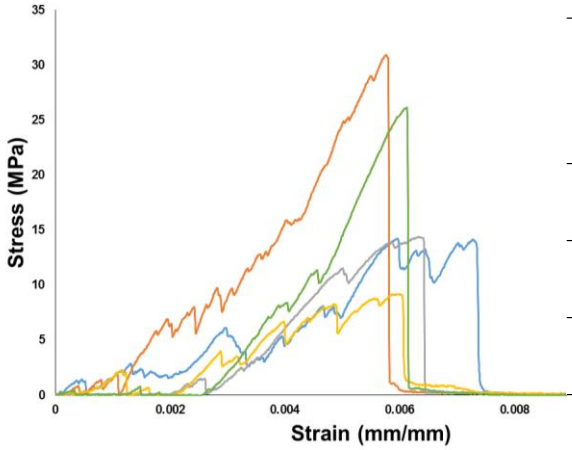

c)

Bending Mean±SD	Maximum Strength (MPa)	Effective Modulus (GPa)
Bars (30x2mm)	18.8±9	1.4±1
Cortical bone	50-150	7-25
Cancellous bone	NA	0.7-0.8

Figure 38 - Mechanical behaviour of samples under bending. a) Successfully printed and sintered bars used for 3-point bend test. Ruler displaying the dimensions in (x,y). Ruler spacing: 1 mm. b) Stress-strain evaluation containing all 5 samples tested. c) Table of values obtained for maximum strength and effective modulus of measured samples.

5.1.9 Bioactivity and CaP ratio determination

The bioactive character of the AW samples was studied via immersion in SBF. The data was retrieved at day 1, 7, 14 and 21 and the results displayed in figure 39. The pH significantly increases at day 7, and then decreases by day 14 (figure 39a). No further alterations were recorded up to day 21. The change in pH can be related to the difference in mineral nucleation between day 1 and day 7 (figure 39b). At day one, residual nucleation is observed, whilst at day 7, a fully developed layer of apatite globes is shown. Past day 7, up to day 21, full coverage of the sample is attained, with typical cracking of the layer noticeable at day 14. The CaP evolution was estimated with EDS and added in figure 39a. During the first week the

apatite coating evolves from Ca deposits to an amorphous layer, with a CaP decreasing from 5 to 2.5, the latter typical of Ca deficient apatite (Mekmene *et al.*, 2009). By day 14 the CaP was 1.9, closer to bone apatite (1.67) (Mekmene *et al.*, 2009), unchanged by day 21. The shape of the mineral progresses, becoming more defined with time and mainly presenting the flake-like morphology, typically found in bone apatite. The apatite clusters diameter appears to be within the 2 µm range at day 7, increasing to ~ 5 µm by day 21.

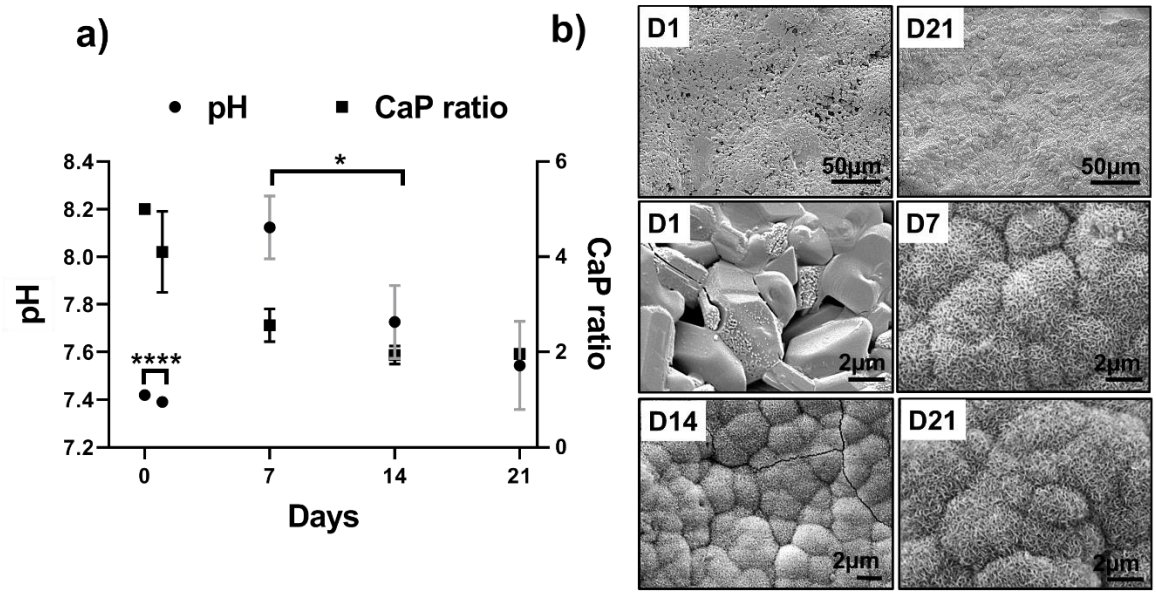

Figure 39- Study of the bioactive character of samples using immersion in SBF. a) pH variation of the SBF solution throughout the study. b) Micrographs of sample surface at each time point. ****denotes significance at p< 0.001, and *p< 0.05 for pH values only.

5.1.10 Study of hTERT MSCs behaviour when seeded onto AW discs

5.1.10.1 Cell viability, growth and proliferation

The metabolic activity of cells on the AW scaffolds and TCP control was measured using the absorbance of diluted formazan crystals, produced by cells during MTT assay (figure 40a). According to the results, cell metabolic activity was not significantly different between the AW samples and the TCP controls, with exception of day 21 where it was significantly higher for AW scaffolds in comparison to the TCP control. The cell viability was demonstrated via live/dead staining, but only for the scaffolds (figure 40b). At day 1 cells appear attached, with most of them stained green, meaning they were alive. Some dead cells can be observed (stained red), but at much lower number. By day 3 the number of dead cells was negligible, and an evident increase in cell density was observed.

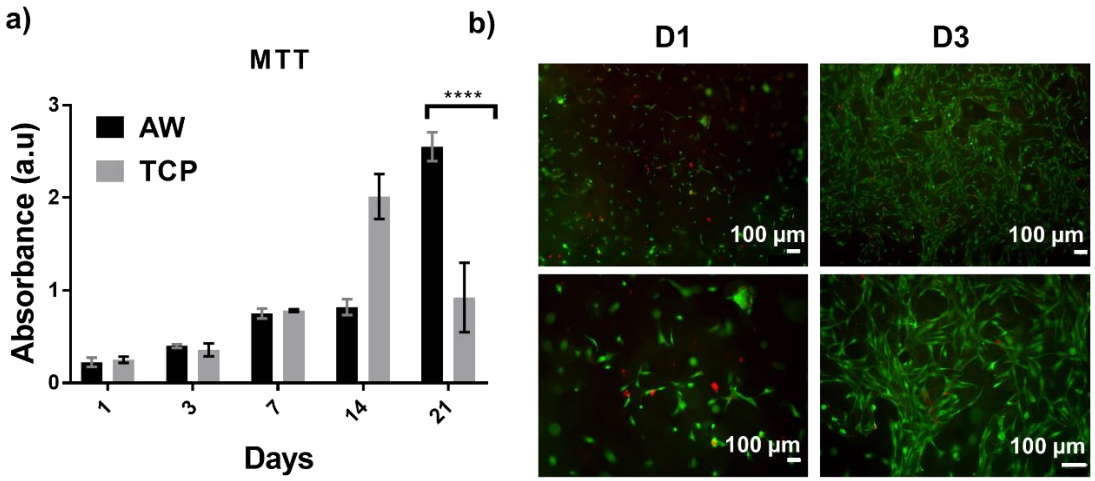

Figure 40 - Cell metabolic activity and vitality measured using MTT and Live/Dead assays. a) Cell metabolic activity based on MTT absorbance values and pre-made calibration curve. ****denotes significance p<0.0001. b) Cell viability and attachment measured at day 1 and day 3, after seeding. Green staining applied for live cells, and red for dead.

Cell shape and morphology were observed with SEM and confocal microscopy (figure 41). From the SEM micrographs, an increase in cell density is noticeable. Cell number progressively increased to form a consistent tissue-like layer, visible at day 21. It is also possible to see that cells colonized the pores of the samples and migrated through them. The successful migration was reported on the cross-section image, showing a cell in the centre of the sample, translated into 1 mm of cell travel. In terms of shape, cells appear fibroblastic at day 1, which is common for the hMSCs, evolving into spindle-like by day 7, commonly seen for pre-osteoblasts (Krishnan *et al.*, 2010). At day 21 a shape could not be distinguished due to the dense tissue formation. The confocal microscopy shows the evolution on both cell shape and adherence. At day 1 cells appear fibroblastic and stained green for the vinculin, meaning they started the focal adhesion process, based on the actin filament nucleation. This continues at day 7, where cell appear prolonged, with spindle-like shape, and grouped. By day 21, a dense tissue structure (Stein, Lian and Owen, 1990; Marion and Mao, 2006) can be seen, with vinculin still being produced.

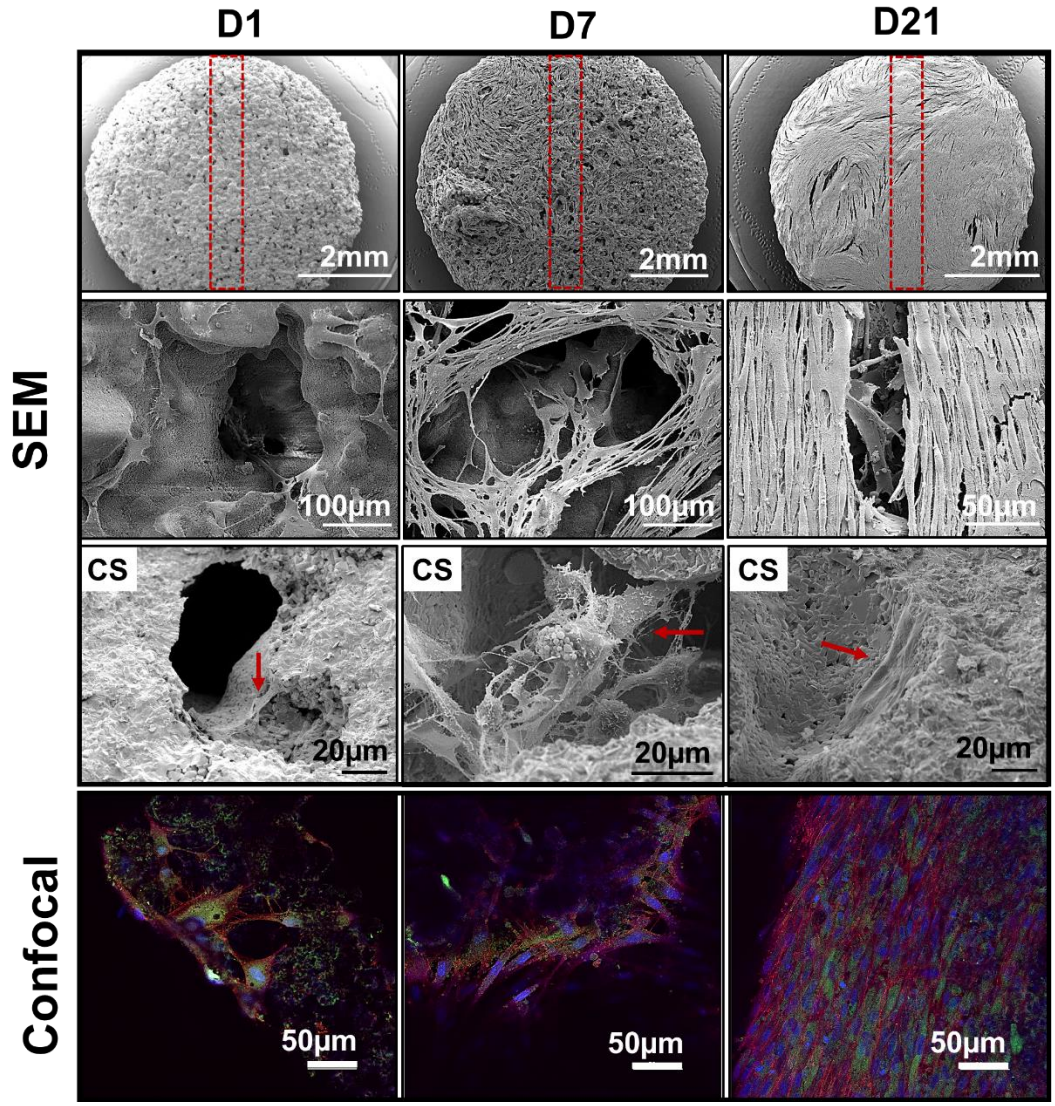

Figure 41 - Cell morphology and attachment on AW scaffolds along the 21 days of study. SEM micrographs taken from the top of the sample, and the cross section (CS) indicate the presence of cell in these areas. Confocal images presenting cell shape evolution, from fibroblastic to spindle-like between day 1 and day 7, culminating in tissue formation at day 21. For confocal, blue staining for targeted the nucleus (DAPI), red the cell body (Phalloidin) and green the actin filaments representing adherence (Vinculin).

5.1.10.2 Osteogenesis and biomineralisation

The ALP levels were significantly different between the AW scaffolds and the TCP at day 7 and day 21 (figure 42a). At day 1 the TCP showed no production of ALP whilst the AW scaffolds did, ~ 3.21 x 10^7 nM/n.cells. One-week post-seeding, the TCP showed significantly higher levels of ALP, with ~ 2.6 x 10^6 nM/n.cells, which then stabilised up to day 21. For the AW scaffolds, no ALP was detected further on, until day 21. The micrographs on figure 42b display the presence of mineral deposits on top of the cells from day 1. The amount of deposits increases with time, and by day 7, plate-like structures are observable, with a crystal

shape resembling the apatite of figure 39b. The CaP ratio (figure 42c) at day 1 was ~ 2, but by day 21 it decreased to ~ 1.5. There is a progressive change from day 1 to day 21, from the Ca deficient apatite range to the bone apatite (1.67).

a)

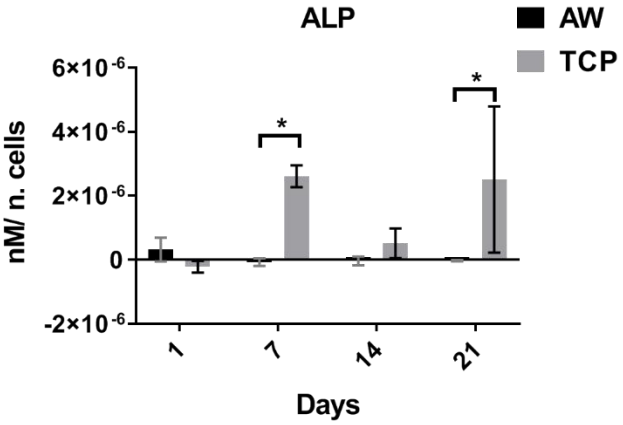

b)

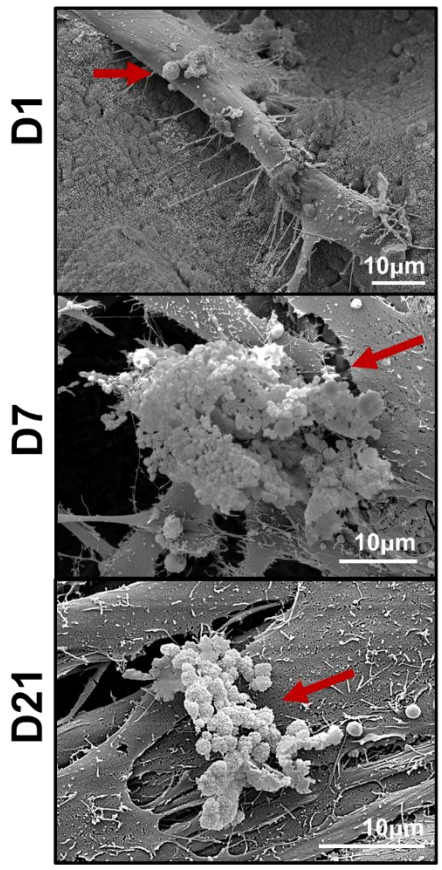

c)

Ca:P Ratio (n=3)		
Days	Mean	SD
1	2.02	0.47
7	1.89	0.22
14	2.08	0.18
21	1.49	0.19

Figure 42 - Evolution of cell differentiation and assessment of biomineralization. a) Evaluation of Alkaline Phosphatase activity as a marker for osteogenesis * denotes $p < 0.05$. b) SEM images of cell containing mineral deposits taken at day 1, 7 and 21. The detected deposits (red arrows) evolved into a more defined structure, presenting a crystal shape like bone apatite by day 21. c) CaP ratio estimation obtained from the EDS analysis.

5.2 Discussion

5.2.1 Powder blend formulation influence and printability

Here, a polydisperse blend of irregularly shaped particles was created, maximum size of1 µm to 144 µm (table 20). These were added in different percentages, aiming to improve the sintering process, and to evaluate the influence of the blend morphology in the printing. When manufacturing the AW scaffolds, the layer spreading was the first parameter evaluated. The Carr index is related to compressibility of the powder, which directly impacts the flow of

particles. According to literature, the limit value for free flow is 21% (Ganesan, Rosentrater and Muthukumarappan, 2008), which is lower than the one obtained for the powder blend, 27%. Other studies consider this value within the fair flowing range (Huang *et al.*, 2013), and this is corroborated by the Hausner ratio value of 1.37, which reflects a fair flowability. The bed density was within the range needed for a good layer deposition using a binder jetting machine (Zocca *et al.*, 2014). Altogether, these values should translate into a successful printing with a defect-free layer deposition (Hausner, 1981; Zocca *et al.*, 2014). In this case, problems with layer dragging were reported, initially associated with the small particle size of the blend. However, it was noted that the dragging effect occurred merely towards the end of the batch, where insufficient material in the feeding platform led to a poor layer spreading. The lack of material in defective layers caused a soaking effect when the binder was deposited. This instigated the particles from the subsequent layer to adhere to the roller, and consequently to lateral layer dragging. Due to limited amount of raw material, a maximum of 500 g was produced each time, limiting the number of experiments that could be performed. Another hindrance was the irregular shape of the powder, which caused particle anchoring, also contributing for the failure of the print at that point (Hausner, 1981; Ganesan, Rosentrater and Muthukumarappan, 2008). It was concluded that below 200 g, printing was no longer possible without major defects in the layers. Despite the poor flowability, caused mainly by lack of material, all initial prints were successful. Parts were easily manufactured but were very weak in green state, impeding the measurement using callipers.

5.2.2 Powder blend influence in the final part structure

After sintering, the sample microstructure slightly changed from a porous bulk of AW particles and dissolved MD, into structure with an interconnected pore network. The total porosity did not exceed 30%, with the open porosity accounting for only ~ 5%. The amount of porosity was low compared to scaffolds targeting cancellous bone (~ 80%) (Hutmacher, 2000; Zeng *et al.*, 2018) but is within the acceptable range of values for implantable materials (Sobieszczyk, 2010). The pore size was smaller than the desired for bone repair applications, being the biggest pores ~ 89 µm (figure 36b). According to literature, the ideal pore size for cell migration and nutrient infiltration is within the range of 200-400 µm (Hutmacher, 2000; Lee, Kim and Knowles, 2014). Although the microporosity is important for scaffolds osteoconductivity, previous studies have reported bone ingrowth in pores smaller than 10 µm (Chan *et al.*, 2012). According to Bignon et al. (Bignon *et al.*, 2003), the macroporosity is important for cell penetration, but microporosity is key on the cell migration since it favours

the adherence of the cytoplasmic microextensions. The successful migration of cells was reported by SEM (figure 41), where their presence in the centre of the sample by day 7 is observable and maintained up to day 21. This suggests that the low open porosity did not hinder their migration into the implant, but it could have contributed for the low number of cells that succeeded to do so.

5.2.3 Factors affecting the mechanical properties

The results for the 3-point bend test indicated that samples maximum strength was identical to the previously studied ones, for similar density values (Ahmetoglu *et al.*, 2009). The values are also within the range attained in chapter 4, expected from the material similarities with M2, and in previously processed AW pellets, using traditional manufacturing (Mancuso, 2016). Compared to dense AW (~ 200 MPa) (Kokubo, 1991), since the samples are ~ 30% porous, values of ~ 70 MPa would be expected, instead of the registered ~ 20 MPa. This is not uncommon, and similar values were reported, with changes relating to the tested device or manufacturing process (Fujita *et al.*, 2000; Xiao *et al.*, 2008). For the effective modulus, samples processed via binder jetting and other manufacturing techniques (Kokubo *et al.*, 1982; Fujita *et al.*, 2000; Alharbi, 2016; Mancuso *et al.*, 2017), presented results up to 10 times higher for the elastic modulus. Differences in powder material processing, sample manufacturing and material composition, don't allow for a direct comparison, but rather serve as references of the versatility and wide range of properties that are attainable with AW. An example is the flexural strength obtained previously with M1 bars (produced also with binder jetting) (Alharbi, 2016; Mancuso *et al.*, 2017), ~ 35 MPa, matching the values obtained here, but with significantly higher modulus. Several reasons can lead to these disparities in results, such as processing and microstructure of the part (Zhang *et al.*, 2007; Ahmetoglu *et al.*, 2009; Park *et al.*, 2010; Willie *et al.*, 2010; Alharbi, 2016; Mancuso *et al.*, 2017).

5.2.3.1 Influence of part processing

Part structural defects, derived from poor spreading of the layers, lead to an heterogenous distribution of the loads, causing the part to fail prematurely (Butscher *et al.*, 2011, 2012; Gomes *et al.*, 2014). Here, several defects were detected with relation to the powder blend flowability and high tendency to compact. Layer dragging caused powder dislocation at each passage of the roller causing a heterogeneity in the final part integrity. Another factor is the sample size and accuracy of the dimensional measurements. Sample warping during sintering, can cause the measurements to be overestimated, leading to a drop on the mechanical properties calculated. Finally, during the sintering process, different compositions will attain

different degrees of interconnection within the structure. The amount of necking is essential not only for the homogeneity of the part, but for the distribution of the loads. Highly crystalline structures do not allow for the same amount of matter diffusion, leading to lower necking between particles and to a higher degree of anisotropy. This is directly reflected on the mechanical properties of the parts, which are weaker and contain a higher amount of stress points (Lee, 1996; Ahmetoglu *et al.*, 2009; Park *et al.*, 2010).

5.2.3.2. Influence of microstructure

Variances in microstructure are also a common cause. Briefly, crystalline materials tend to have superior mechanical performance under loading due to their organized atomic structure (Freiman and Hench, 1972), however, these concepts cannot be fully translated into all material classes. Glass-ceramics mainly consist of a crystal phase trapped within an amorphous glass matrix. These two components have different properties and therefore influence the final part in various ways (Emad and Van Noort, 2011). When organized and homogenous, crystallisation promotes the mechanical strength. When the structure is composed of disoriented and irregularly sized crystals, stress points are generated, hindering the mechanical performance of the part (Freiman and Hench, 1972; Li, Wang and Chen, 2015). Ceramics are naturally stronger under compression, but under bending their performance is highly dependent on a consistent microstructure with fine grain boundaries and no defects (pores inclusive) (Lee, 1996). Samples produced previously with M1 powder were deprived of such developed crystals (present possibly at the nanoscale). This was connected to the presence of alumina at the surface of the particle. The printed structures made with this M2 equivalent, possess crystals visible at the microscale, oriented randomly. Such complex microstructure could translate into more stress points in the microstructure, hindering the flexural properties. Another factor associated with the crystallisation of the part, is the difference between the created crystalline phases, with emphasis on their thermal expansions coefficient (TEC). Different phases have different TEC, meaning they will not contract and dilate identically (Freiman and Hench, 1972). The results discussed in chapter 4 indicate that the AW powders sinter through different mechanisms, and therefore area reduction also changes. This is supported by the amount of crystalline phase present for the M1 and M2 sintered samples (figure 28b). M2 samples, possessed higher intensity peaks for both whitlockite and wollastonite, and diopside, compared to M1. This means that the crystallinity is further developed, enhancing the effect of TEC in the final properties. This difference in expansion and contraction of phases adds stress to the structure and needs to be

removed either by doping the material with a stabiliser, by introducing an annealing step, or both (Freiman and Hench, 1972).

5.2.4 Impact of crystallisation in bioactivity

The concept of bioactivity and the mechanism by which it occurs were introduced in chapter 2. Several studies have shown that, changes smaller than 2 wt% in a glass composition can affect both bioactivity and degradation rate (Abou Neel *et al.*, 2009; Murphy *et al.*, 2009; Miola *et al.*, 2014). Filho et al. as shown how the increase in crystallisation can retard the development of the HCA layer (Filho, La Torre and Hench, 1996; Massera *et al.*, 2015). The AW used in this work has a high tendency for crystallisation (chapter 4), therefore concerns regarding the loss of bioactivity were raised. As the results show (figure 39b), the material remained bioactive even after crystallising, with apatite nucleation starting after 1 day of immersion in SBF. The CaP evolved with time, resulting on a mean CaP of 1.96 at day 21, close to bone apatite, reported as 1.67 (Mekmene *et al.*, 2009). These results ensured the bioactive character of the material, therefore its potential use in implantable devices.

5.2.5 MSCs growth, differentiation and biomineralisation

AW is a biocompatible material, and this translated into the cell viability shown on figure 40. Cells were alive and adhered by day 1 and proliferated along the 21 days. At day 21, the number of cells estimated for the AW scaffold was significantly higher than for the TCP which could be associated to the higher surface area of the scaffolds, promoted by the porosity (Hutmacher, 2000; Joshi *et al.*, 2013). Another possibility is the limited area of the TCP well that can lead over confluency, causing cell death. Silicate-based bioactive glasses and glass-ceramics have proved to enhance the bond between implant and tissue, which provides a more stable environment for bone healing. Another advantage of these materials is the ion leaching profile. Some ions can induce a specific response, e.g. osteogenic differentiation, up-regulation and activation of genes related to osteoprogenitor cells, and angiogenesis (Baino *et al.*, 2016). The addition of stabilizers such as alumina can reduce the glass solubility, inhibiting its bonding to bone (El-Kheshen *et al.*, 2008). The AW used had a minor contamination of alumina at its surface, however, the effects reflected only in the crystallisation behaviour of the material (chapter 4). The bioactivity was maintained implying that the ion release remained unchanged, therefore the cell response should also be positive. By seeding the scaffolds with hMSCs, their ability to induce osteogenesis was explored. The

ALP measurement for the AW scaffolds (figure 42) showed a common behaviour for these cells, a higher peak at day 1 followed by a decrease, and later absence of ALP (James *et al.*, 2015). The abrupt decrease in ALP is commonly associate with the transition between differentiation and mineralisation stages (Stein, Lian and Owen, 1990; Loty *et al.*, 2000). ALP is produced when differentiated cells need phosphorus to make apatite (Štefková, Procházková and Pacherník, 2015). When the P is available, and the mineral is present, the ALP levels naturally decrease (Endres *et al.*, 2003; Marion and Mao, 2006). The transition between differentiation and mineralisation appears to take place between day 1 and day 7, but in between these ALP values were not monitored impeding the quantification. The biomineralisation was assessed with SEM and EDS (figure 42b), by observing the Ca deposits on top of the cells and estimating their CaP ratio with EDS (figure 42c). Visibly developed crystals arranged in clusters are shown (figure 42b), smaller than 5 µm each. The EDS analysis confirmed the CaP ratio as ~ 1.5 by day 21, meaning the cell started to mineralise. The ALP values on TCP increased and remained stable after day 7, implying that differentiation occurred. SEM and EDS analysis were not performed for TCP due to equipment restrictions.

5.3 Conclusion

A polydisperse blend consisting of 70% AW and 30% MD was successfully formulated and characterised in terms of printability. In terms of part processing, it was observed that a successful manufacturing of the AW scaffolds depends on both powder blend properties, and machine set-up/limitations. Despite the labelling of the blend as “fair flowing”, it was concluded that a minimum amount of powder must be available to avoid layer dragging and excessive binder saturation. For the part characterisation, the main observation relied on the relation between porosity and mechanical properties. It was determined that, for glass-ceramics, the mechanical properties depend on both structural and crystalline properties of the material. For the same amount of porosity, and the same material base composition, the difference in crystallinity, namely crystal size and orientation, proved to play a crucial part in the overall TEC. Allied to the layer defects, this led to the appearance and random distribution of stress-points in the sintered microstructure, causing it to fail prematurely. With this, it is concluded that the material processing must be finely controlled for the application in view. Bioactivity of the material remained unchanged as well as the response to hMSCs, proving that the addition of crystallisation only influences the mechanical performance of the device, without adding any valuable features. If no further alterations of the process are performed,

the scaffolds could be used in areas with lower loading, in small defects or as tissue regeneration platforms. For load bearing application, optimisation of the process and blend must be done, alongside the addition of stabilisers and changing of the sintering process to include an annealing step. The work developed on chapter 4 contributes for these findings, where it is suggested the intentional doping of the AW powder with alumina, to control and suppress the crystallisation, could lead to the improvement of mechanical properties, obtained in previous studies.

Chapter 6. Fused Filament Fabrication of biocomposite scaffolds for bone repair

The work reported in this chapter considers the use of AW as a bioactive filler within a medical grade PLLA matrix. A composite filament was created to allow the manufacturing of scaffolds using FFF. Three types of porous woodpile samples were created, PLLA, PLLA reinforced with AW particles and PLLA with AW fibres. These aimed to assess the influence of both AW fillers on mechanical properties, degradation profile and impact on hMSC differentiation and mineralisation.

6.1 Results

6.1.1 Characterisation of raw materials: PLLA, AW fibres and AW particles

The material chosen for the matrix of the composite consisted of medical graded PLLA. Since the polymer must undergo several melting processes, an initial assessment of the thermal transitions was performed and used for process optimisation. The DSC analysis (figure 43a and 50c) demonstrated only a T_g and T_m, located at 76 °c and 195 °C, respectively. For the AW precursor particles, the analysis has been performed on chapter 5, figure 37. The AW fibres DSC (figure 49b and 49c) showed 2 T_c peaks (905 °C and 922 °C) and a T_m (1256 °C), but no T_g.

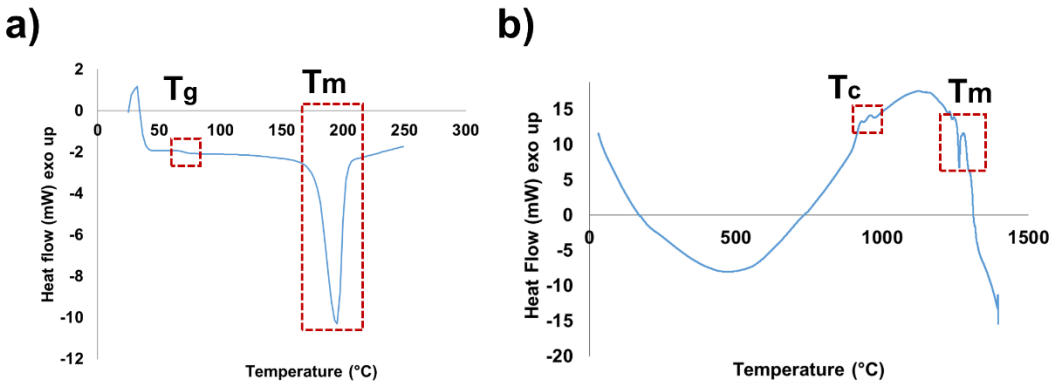

c)

Thermal transition	Temperature (°C)	
	PLLA	AW fibre
Glass transition (Tg)	76	NA
Crystallization (Tc)	NA	905 and 922
Melting (Tm)	195	1256

Figure 43 - DSC analysis of PLLA and AW fibres with thermal transitions. Tg and Tm meaning glass transition and melting temperatures, respectively. a) PLLA; b) AW fibre; c) thermal transitions collected from software analysis.

XRD of PLLA granules shows the presence of peaks typical from semi-crystalline PLLA alongside both structural phases, α and α' (Cocca *et al.*, 2011) (figure 44a). The AW fibres as produced, presented a spectrum typical of an amorphous material (figure 44b), mimicking the one obtained for AW powder (figure 28a).The spectrum of the printed part is typical of an amorphous structure, with only a residual peak of α phase (figure 44c). For the composite scaffolds the same peaks as in the PLLA scaffold were displayed (figure 44d).

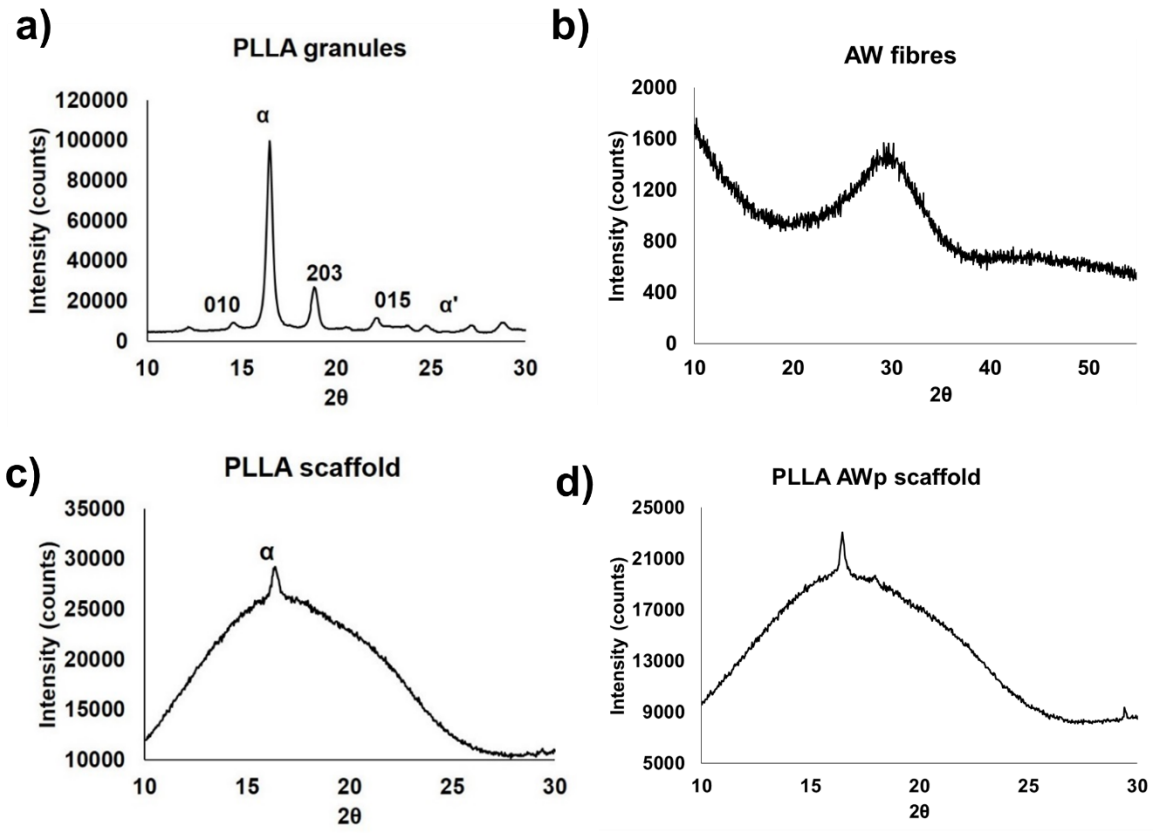

Figure 44 - XRD pattern of PLLA granules (a), AW fibres as produced (b), printed PLLA scaffold (c) PLLA/AWp scaffold (d).

6.1.2 Primary analysis of printed parts

Photographs of the parts were taken, using a ruler as mean of measurement. According to the images (figure 45a), the parts dimensions in (x,y) and (z) planes were identical to the CAD file (chapter 3, section 3.2). The woodpile design was also fully replicated, with no incongruences in the print. The printed structures presented a smooth surface and were easy to handle. The SEM (figure 45b) report a part with consistently adhered layers, but a few inaccuracies in the size of the beam were found.

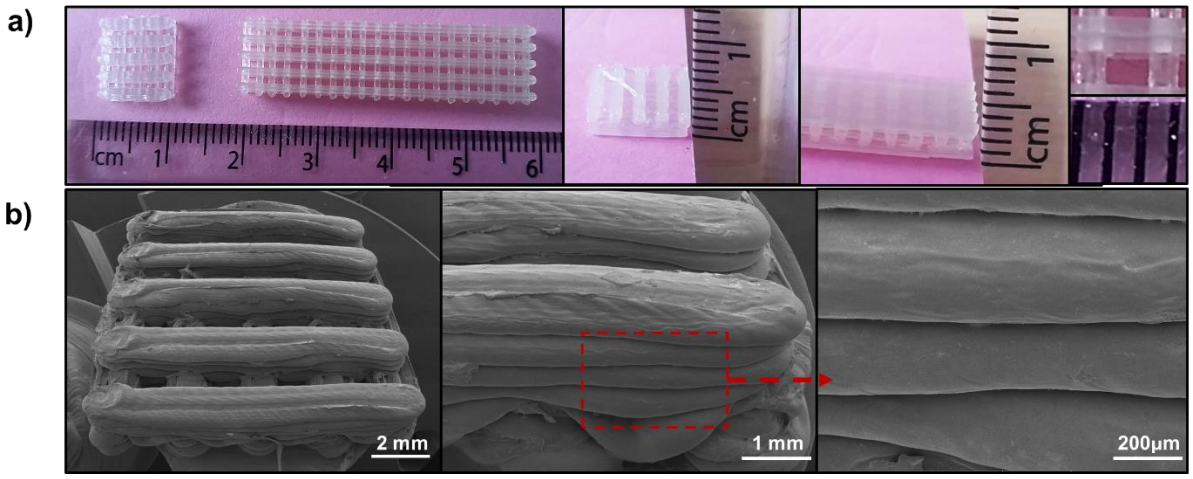

Figure 45 - Structure of parts as printed and illustrative dimensions. a) Photograph of printed PLLA parts, with dimensions illustrated by a ruler. From left to right: parts top view, square and bar from front view (z), and pore (distance between ruler lines is 1 mm). b) SEM of scaffolds after printed. From left to right: Overview of the scaffold, side view of the part to observe layer deposition and, zoomed set of layers exemplifying the adherence and dimension of deposited beams.

6.1.3 Structural characterisation of printed parts

SEM studies, shown in figure 46, display clearly the presence of AW particles and AW fibres in each of the composites (PLLA/AWp and PLLA/AWf) while PLLA parts were smooth and absent of inclusions. The SEM micrographs show the lack of bond between filler and matrix on biocomposite filaments, demonstrated by the clear separation between filler edges and matrix (pointed by arrows). After 8 weeks of immersion in PBS no changes in the structure were detected. The µCT micrographs of printed parts show how the filler is homogeneously distributed within the polymer matrix, with visible fibres close to the surface, also seen on SEM.

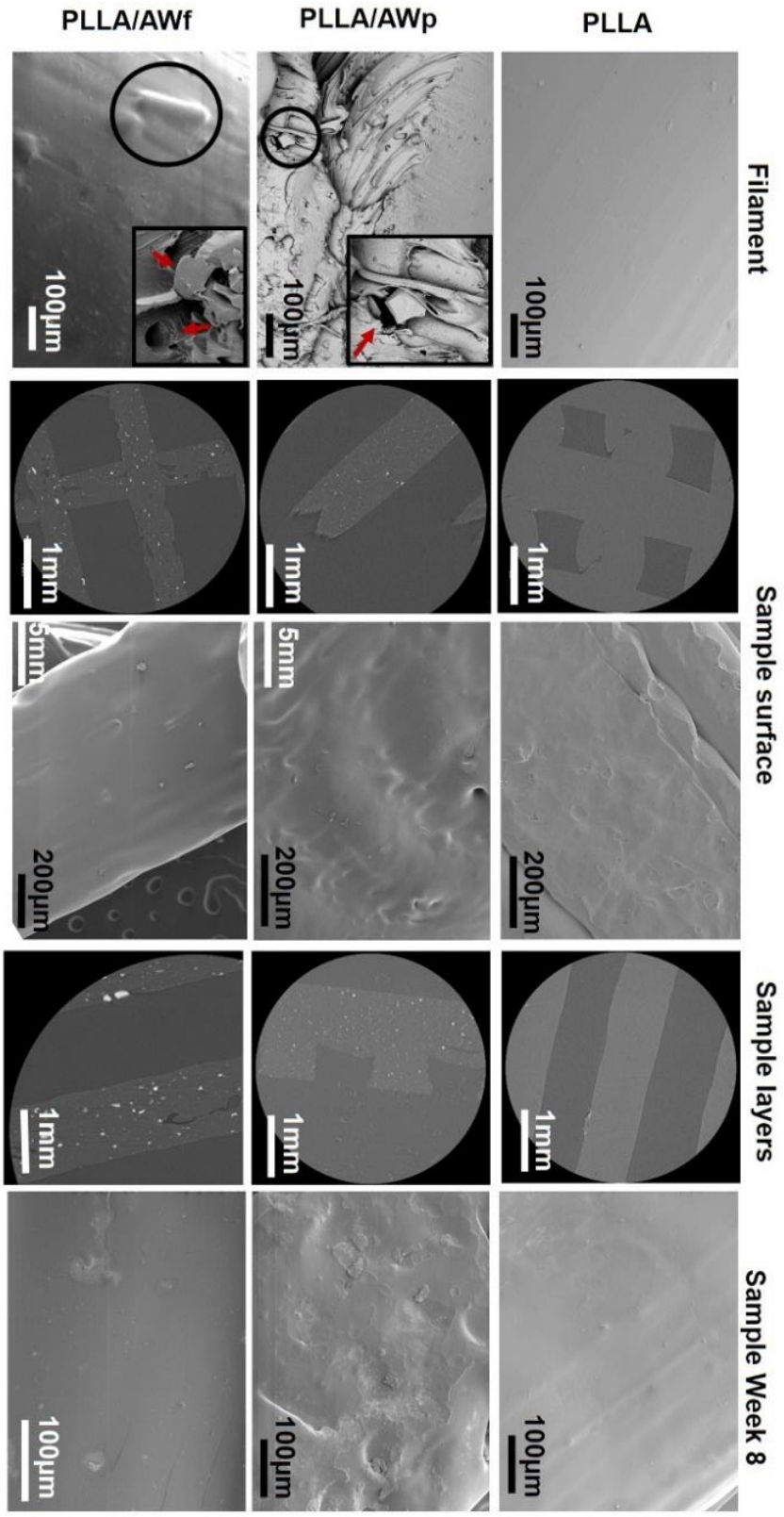

Figure 46 - SEM and µCT images corresponding toboth filament and printed samples, before and after 8 weeks of degradation in PBS. SEM of printed parts, supported by µCT, showing a homogenous distribution of filler. Circled area displaying a particle and a fibre of AW inside the respective composite filaments. Arrows on SEM pointing the interface between filler and matrix.

The polymer size and hydrodynamic radii were assessed with ^{1}H NMR DOSY, but no differences were found amidst all processed polymer materials (figure 47). A decrease on polymer size, compared the raw unprocessed material (R_H $CDCL_3$ 2.2 nm), was found for samples in dilute solutions (figure 47a). Throughout the degradation period, the results for processed PLLA R_H $CDCL_3$ 1.45 ± 0.10 nm, indicate that the polymer material is stable and undergoes little degradation over the 8 weeks (figure 47b).

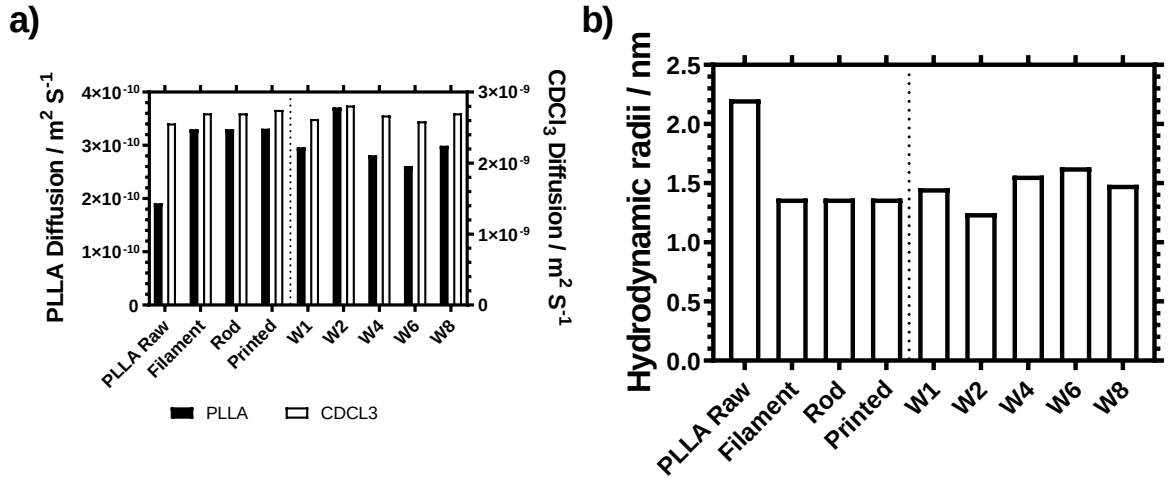

Figure 47 - Diffusion analysis of polymer samples in dilute CDCl3 solution. a) Measured diffusion (m^2 S^{-1}) of PLLA and solvent proton peaks. b) Calculated average polymer hydrodynamic radii.

The mechanical properties as printed were obtained from 3-point bend test and were noted in table 23. As printed, the flexural strength of the composites differed, with PLLA/AWf attaining a significantly higher effective modulus, **~** 1.5 GPa, compared to PLLA and PLLA/AWp which reported **~** 0.9 GPa and **~**1 GPa ($p< 0.001$ and $p< 0.01$ respectively).

Mechanical properties	**3-point bend test**	
	Yield point (MPa)	Effective modulus (GPa)
PLLA	16.6 ±10.4	0.9±0.3
PLLA/AWp	22.8 ±4.5	1 ±0.1
PLLA/AWf	29.4 ±5.3	1.5±0.2

Table 23 - Mechanical properties of scaffolds as printed expressed in terms of mean ± SD for n=5.

6.1.4 Physicochemical changes and Ion leaching

Samples were immersed in PBS for 8 weeks and their weight, mechanical properties and ion leaching profile were studied. No changes were found for the flexural strength and modulus throughout the study (figure 48a and 48b, respectively), and no mass loss was detected (omitted for brevity). The PBS solution pH was different at determined time points, varying between 7.2 and 7.6. No trend was found for the changes (figure 48c), but values are similar to the ones of physiological conditions (~ 7.4) (Cüneyt Tas, 2000a). The ion leaching analysis (figure 48d and 48e) showed major observations for week 1 and week 2. An increase in Ca (figure 48d) and Mg (figure 48e) was readily detected at week 1 for PLLA/AWf, with Ca and Mg concentrations of 86 and 23 µM, respectively. This value was significantly higher compared to the PLLA sample (11 µM Ca and 4.5 µM Mg) but identical to that of the PLLA/AWp sample (78 µM Ca and 12 µM Mg). At week 2 the same trend was observed, with PLLA/AWf showing the highest values (51 µM Ca and 12 µM Mg), PLLA/AWp showing lesser concentrations (23 µM Ca and 4.3 µM Mg), followed by PLLA (5.7 µM Ca and 1.7 µM Mg). Past week 2, all values remained basal and stable and no significant differences between samples were found.

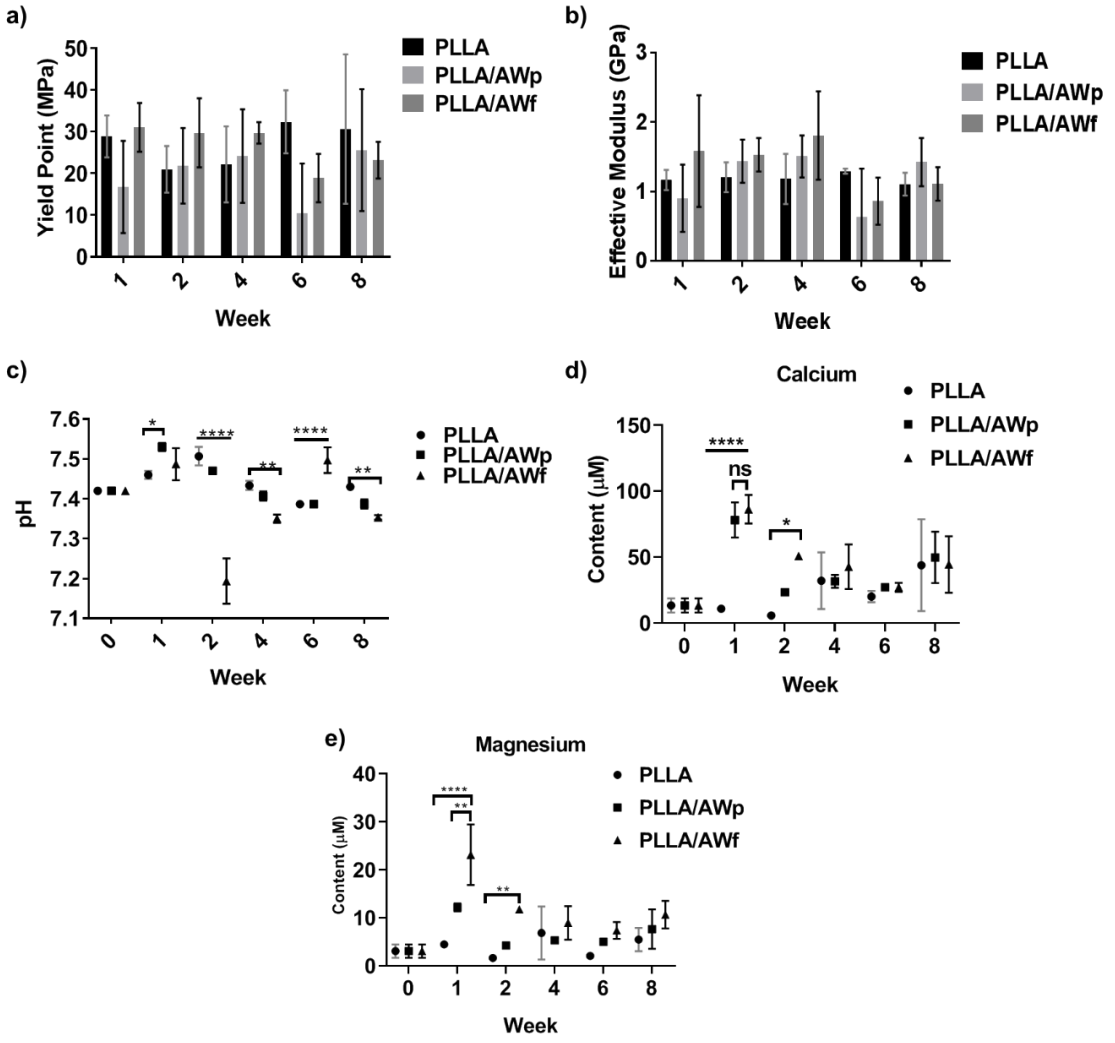

Figure 48 - Flexural properties of scaffolds and ion leaching into PBS (week 1, 2, 4, 6 and 8 after degradation in PBS). a) Yield point; b) Effective modulus; c) pH variation of PBS solution; d) e) content of Ca and Mg, respectively. $p<0.05$ (*), $p<0.01$ (**), $p<0.001$ (***) and $p<0.0001$ (****).

6.1.5 Bioactivity assessment - apatite deposition, morphology and CaP ratio

Bioactivity (figure 49) was only observed for composite samples, whereas PLLA reported a clean surface at all time points. Mineralised deposits at the surface from day 1 to day 21 are visible, and their elemental composition was estimated with EDS (table 24). The Ca and P ratio of the precipitates increases during the first week for both samples, with PLLA/AWp evolving from 0 to ≈ 1.6, and PLLA/AWf from 1.5 to 2. The pH of the solution was similar for all samples with exception of day 7 when the PLLA/AWp had a higher pH than the PLLA. This was not considered significant therefore results were not added. The mineral shape consisted mainly of irregular clusters, unlike the typical cauliflower shape (Kokubo and Takadama, 2006).

CaP (mean±SD)	PLLA	PLLA/AWp	PLLA/AWf
Day 1	0.0±0.0	0.0±0.0	1.5±0.5
Day 7	0.0±0.0	1.6±0.1	2.0±0.1
Day 14	0.0±0.0	1.0±0.7	0.8±1.1
Day 21	0.0±0.0	1.6±0.5	1.5±0.5

Table 24 - CaP ratio of deposits detected at the surface of biocomposite samples. No deposits found for PLLA, with values registered as 0.

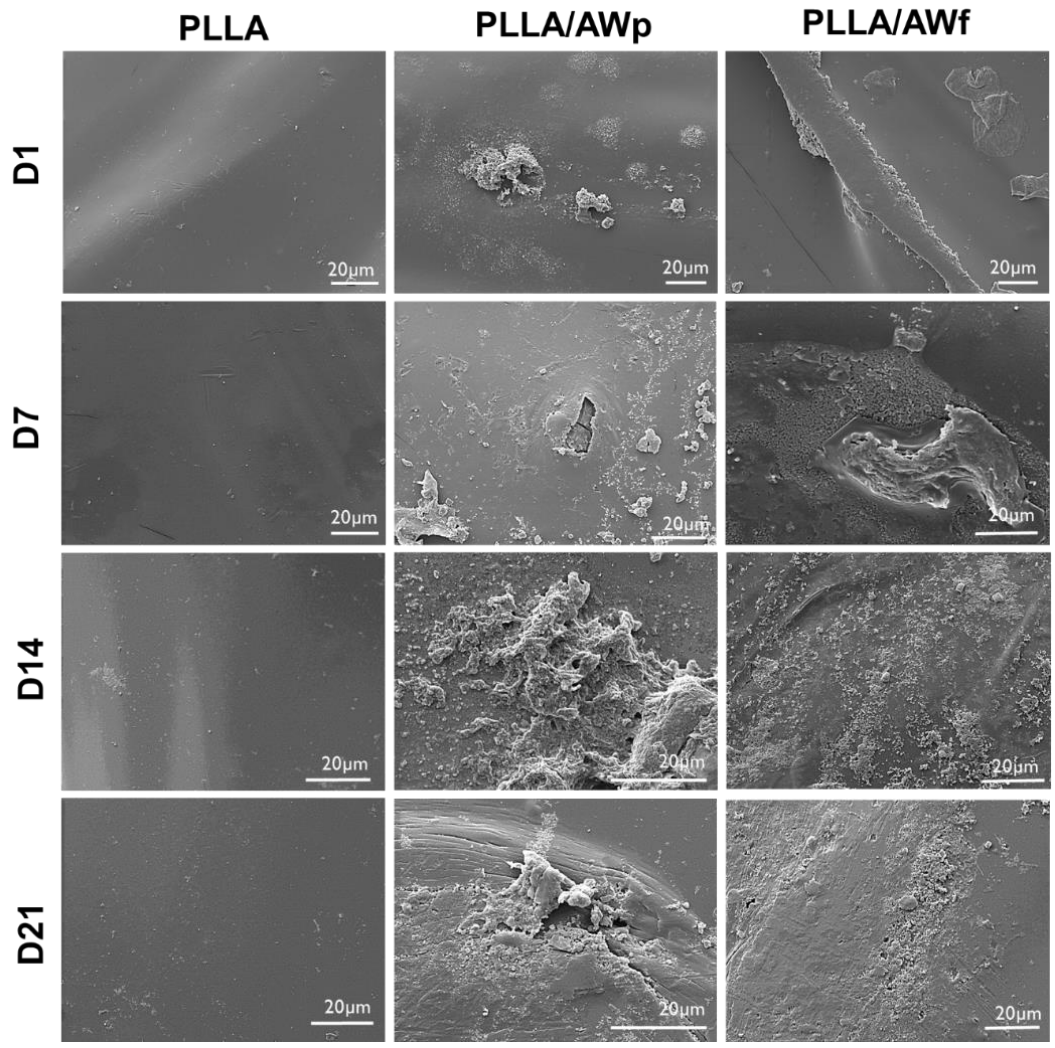

Figure 49 - SEM analysis of samples and SBF solution after immersion for 21 days. Micrographs of composite samples show deposits of material at the surface.

6.1.6 Biological assay – Cell viability, osteogenesis and mineralisation

The production of formazan by the cells increased up to day 14 for all samples, followed by a stabilisation (figure 50a). The same trend was observed for the cell number for all samples (figure 50b). PLLA/AWf and TCP samples showed significantly higher values for day 7, 14 and 21 ($p < 0.0001$) compared to PLLA/AWp and PLLA (ns). Cell viability was similar for all scaffolds at day 1 and day 3, as observed on figure 50c. Live cells seem attached from day 1 and back to normal morphology by day 3.

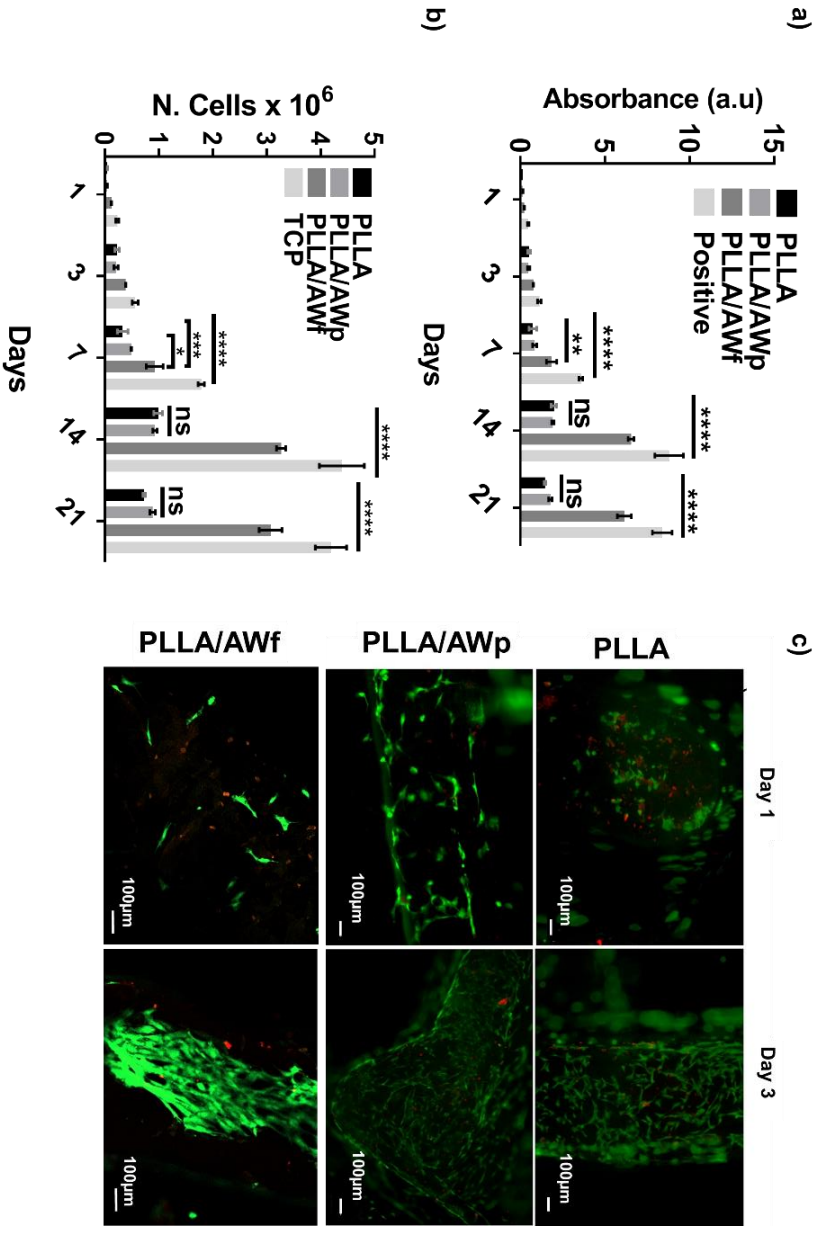

Figure 50 - Proliferation of cells seeded on PLLA and PLLA/AW scaffolds compared to tissue culture plastic via MTT assay, and cell viability using Live/dead. a) Absorbance reading of dissolved formazan crystals. b) Estimation of cell number using MTT absorbance values and a pre-made standard curve (chapter 3). ***denotes significance at $p < 0.001$, and ****$p < 0.0001$. c) Cell attachment and viability at day 1 and day 3. Green indicating living cells and red dead cell.

The micrographs in figure 51 report the cell behaviour along the 21 days. Cell adherence after 24h, and tissue formation after 21 days were reported, with PLLA/AWf demonstrating a multilayer formation and an apparent higher cell density, supported by figure 50b and 50c. In terms of morphology, at day 1 cells are grouped and have a fibroblastic shape (James *et al.*, 2015). The morphology evolved to spindle-shape at day 7, a finalised as cobblestone-like, at day 21 (Hatakeyma *et al.*, 2013). Dense tissue formation at day 1 prevented a finer observation.

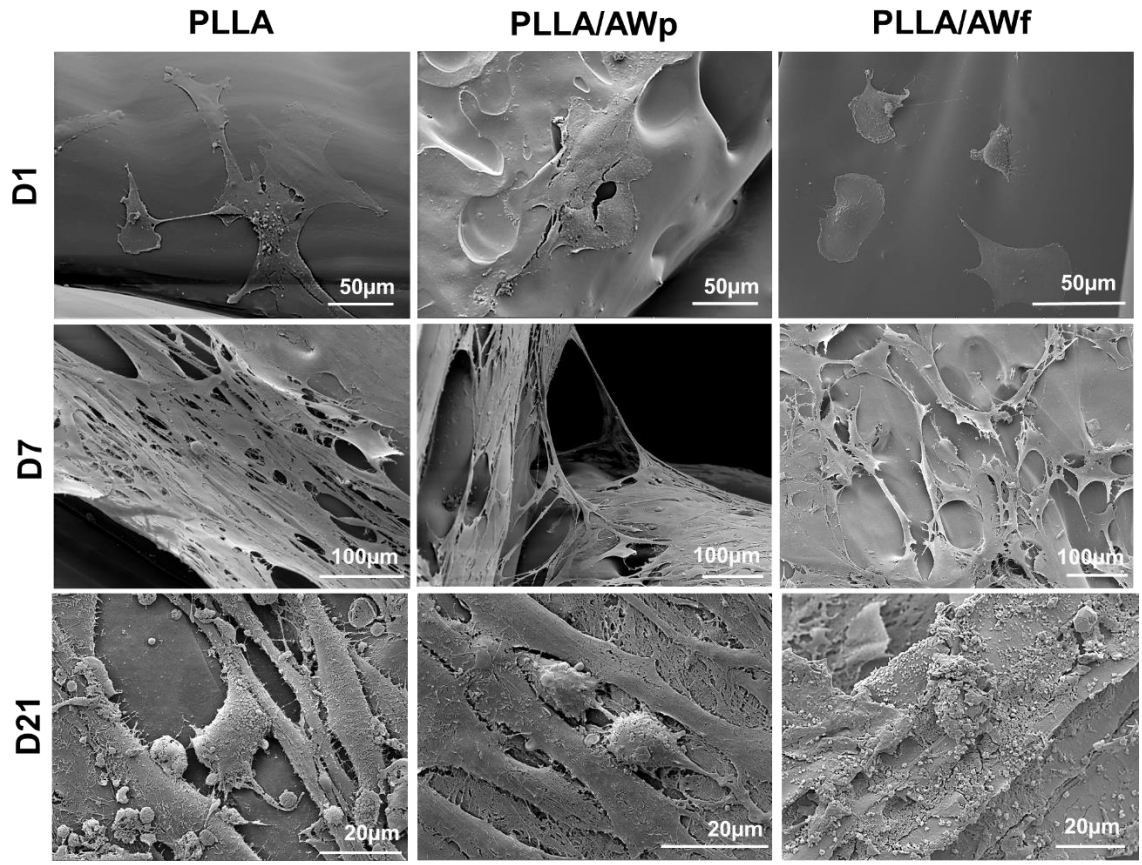

Figure 51 - Evolution in cell morphology and attachment on the studied samples. SEM images in grey scale, on the right for each type of sample.

6.1.7 Osteogenic differentiation and cell mineralisation

The ALP activity (figure 52a) did not differ between samples aside from day 1 where PLLA and PLLA/AWp had significantly higher production than PLLA/AWf and TCP. From day 7 onwards samples did not diverge between each other. When analysed individually, the ALP values for each sample did not change with time, with exception of PLLA which experiences a significant drop between day 7 and day 14. Figure 52b shows the presence of mineralisation on top of the cells in both composite scaffolds, and for PLLA/AWp octacalcium phosphate apatite (flake-like form) (Venugopal *et al.*, 2010; Zhang *et al.*, 2014). XPS analysis of the

samples surface (figure 52c) confirms the presence of Ca for composite samples only, with PLLA presenting a residual value due to equipment artefact. Ca content was not significantly different between composites at any time point. XPS and EDS analysis were not performed on TCP samples due to the equipment limitations.

The visual presence of mineralisation was shown by alizarin red staining (figure 52d) at day 21. All samples presented red staining, but not the TCP. Presence of Ca and P was confirmed by EDS analysis (table 25), however only for the composite samples. The measurements were taken at sites where deposits were found on top of the cells to separate them from what could be HCA layer from the samples. Mineralisation wasn't detected on cells at day 1, inferring that these values are associated with the sample rather than the cells. PLLA samples presented an atomic % of 0 (zero), while the composites reported values within the range of Ca deficient apatite, close to bone apatite (CaP of ~1.6) in the case of several samples. For the TCP, stereomicroscope images reported the absence of staining, consequently these were not included in the analysis.

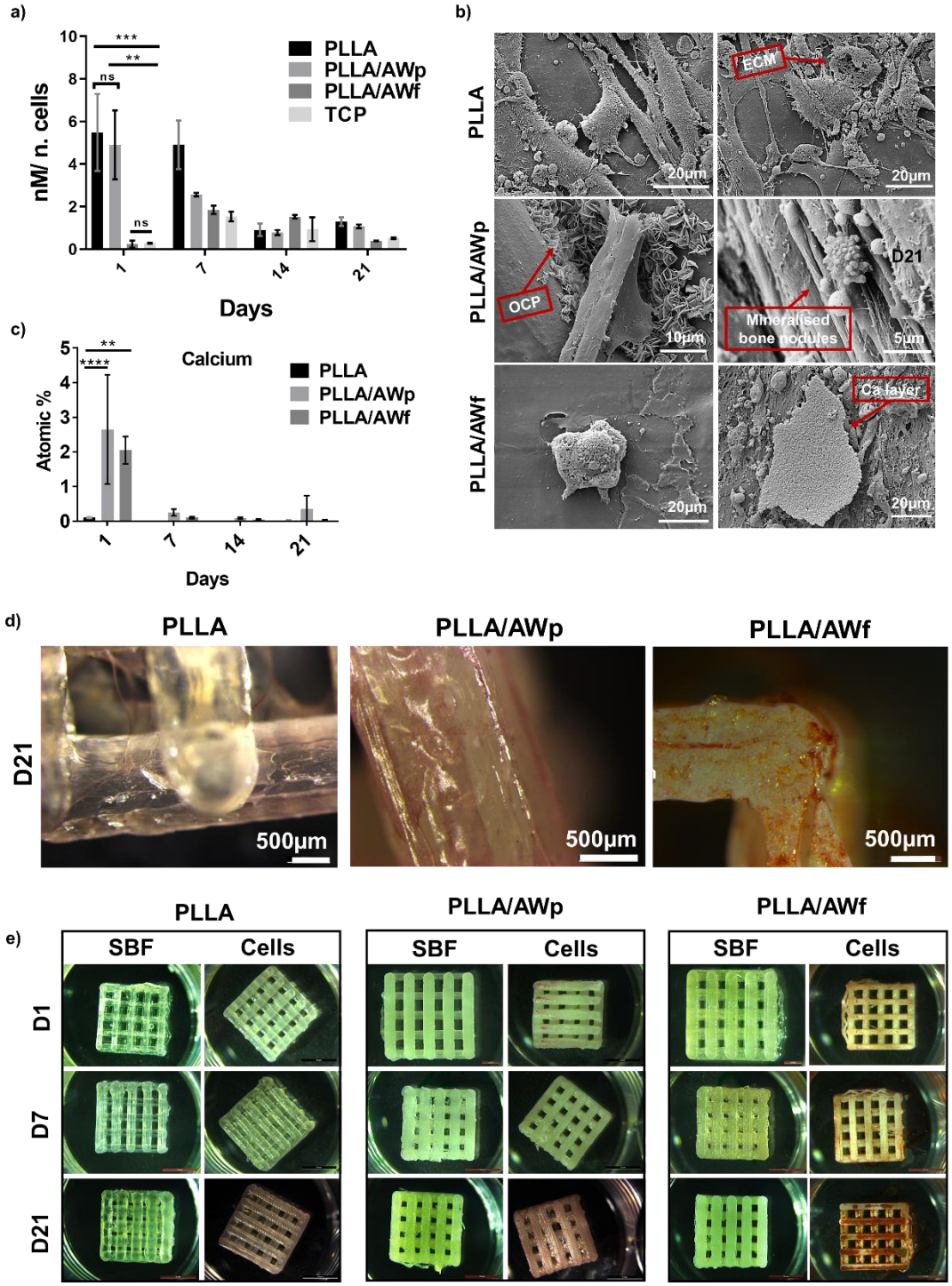

Figure 52 - Osteogenic differentiation of seeded cells for polymer and composite samples. A) Alkaline Phosphatase activity measurement as osteogenesis indicator. b) SEM images of samples at day 21. Presence of octacalcium phosphate indicated by OCP on PLLA/AWp alongside cell with mineralised bone nodules indicating mineralisation. Ca layer on PLLA/AWf. c) XPS analysis of Ca content. d) Alizarin red staining of cell-seeded PLLA, PLLA/AWp and PLLA/AWf scaffolds Micrographs of samples collected at day 21. Red stain indicated presence of Ca at the sample surface (bar 5mm). e) Comparison of samples immersed in SBF and samples seeded with cells. Statistical analysis between samples at each time point, $p < 0.01$ (**), $p < 0.001$ (***) and $p < 0.0001$ (****).

CaP (mean±SD)	PLLA	PLLA/AWp	PLLA/AWf
Day 1	0.0±0.0	1.7±1.6	0.7±0.8
Day 7	0.0±0.0	0.8±1.0	0.9±0.2
Day 14	0.0±0.0	1.2±0.6	0.4±0.3
Day 21	0.0±0.0	1.1±0.6	0.6±0.7

Table 25 - CaP ratio of samples per time point. Values presented as mean ±SD for n=3.

The confocal analysis (figure 53) corroborates the data relating to cell differentiation, up to day 21 where the thick tissue does not allow a clear observation of morphology. The staining of collagen type 1 also acted as a marker for cell differentiation into osteoblasts. The increasing concentrations of collagen type 1 with time (stained green) suggest that cells are differentiating into osteoblasts in all tested samples (Astachov, Nevo and Vago, 2012a). This information is corroborated by the cell shape, already described in figure 51, where the evolution from fibroblastic to spindle-like can be seen between day 1 and 7. The presence of vinculin ensures the cell adherence, with the actin filaments allowing for their stabilisation and facilitating their migration.

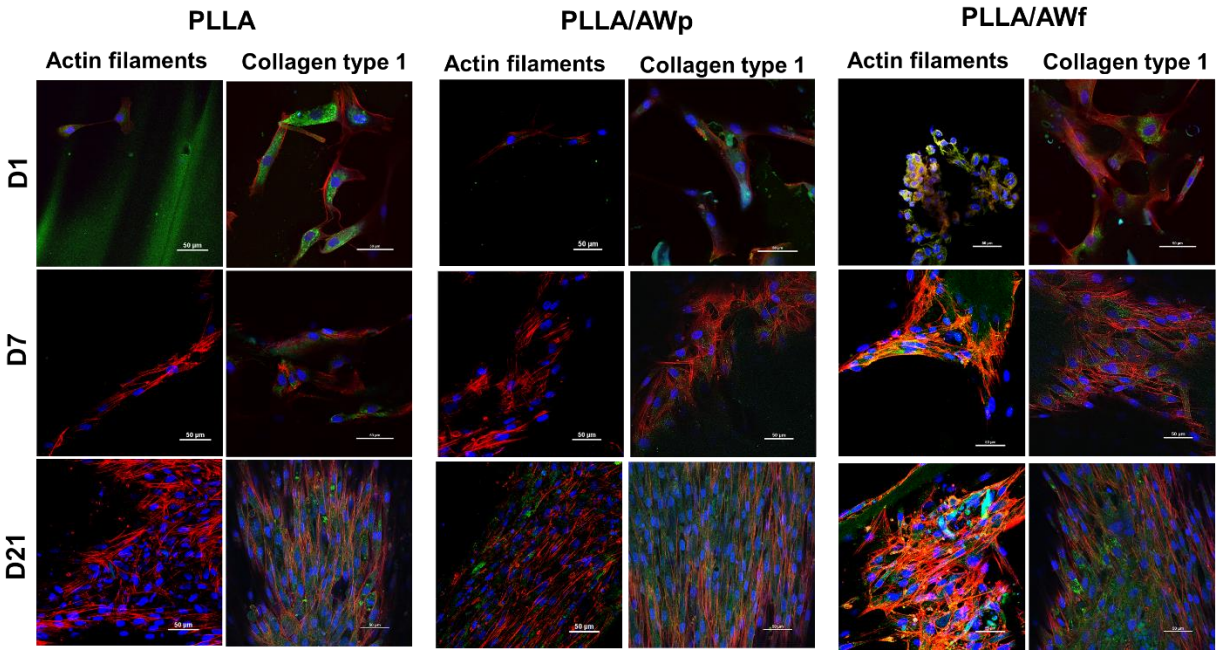

Figure 53 - Confocal images, using blue staining for nucleus (DAPI), red for cell body (Phalloidin) and green the actin filaments representing adherence (Vinculin) and collagen type 1.

6.1.8 Estimation of sulphated proteoglycan production to study ECM deposition

The presence of sulphated proteoglycans was imaged and quantified to understand the production of ECM by the cells throughout the 21 days of study. The concentration of sGAGs was estimated using a calibration curve (figure 54a) and plotted on figure 54b. The results show identical values for PLLA and PLLA/AWp, however these are significantly higher than the ones of PLLA/AWf. Samples were not significantly different for the remaining time points, and all experience a significant decrease between day 1 and day 7. Visually, this effect is not as obvious. The alcian blue staining (figure 54c) of samples shows a similar amount of blue at day 1, for all samples. At day 7, the presence of sGAGs is also obvious in all types of scaffolds, and is enhanced at day 21, where it covers the whole structure. It must be clarified that the GAGs concentration plotted is an estimation as the calibration curve obtained was not as good as expected.

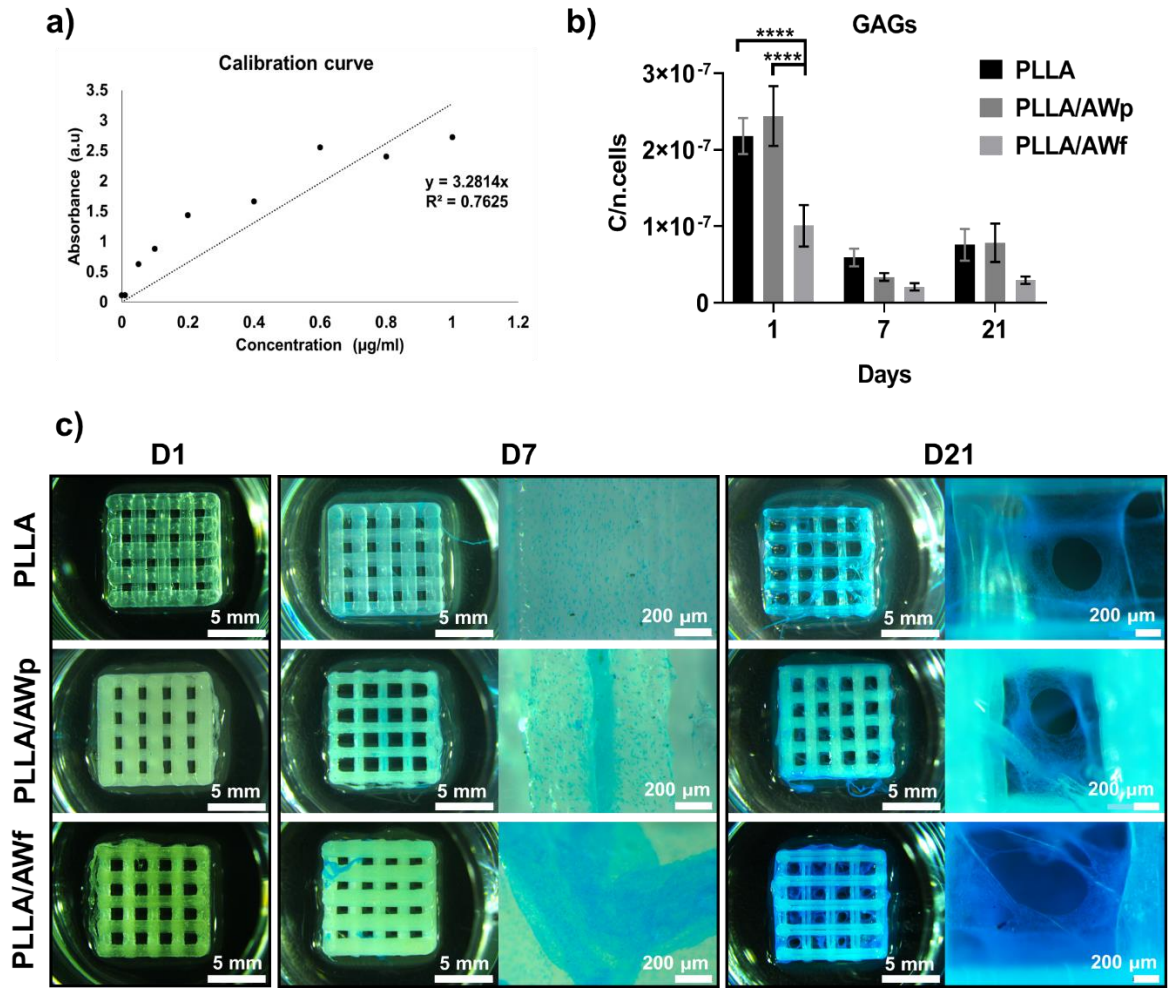

Figure 54 - Production of ECM through observation and estimation of the sGAGs. a) Calibration curve created using different concentrations of chondroitin sulphate. b) Estimation of the concentration of sGAGs per cell number at day 1, 7 and 21. c) Alcian blue staining of sample to visually evaluate the presence of sGAGs and relative amount in each sample. Statistical analysis between samples at each time point with $p < 0.0001$ (****).

6.2 Discussion

6.2.1 Processing of composite: from filament production to printing

In this study we demonstrate the successful optimisation of both filament and sample processing methods, regarding particle and short fibre reinforced composites. The homogenous distribution of the filler was attained from the initial blending of the material and its mixing inside the extruder (Wang, 2003). On the processing of PLLA/AWf, fibre alignment in the printing direction was observed. This was expected due to shear forces inside the nozzle, a well reported phenomenon for both long and short carbon and glass fibres (Zhong *et al.*, 2001; Ferreira *et al.*, 2017; Brenken *et al.*, 2018). The printing process made the polymer structure amorphous (figure 44a, 44c and 44d), which could be associated to the fast cool down of material (Dionísio Viciosa, María Teresa, Wang, Yaming, Mano, João F., 2005; Cocca *et al.*, 2011). This structural change in crystallinity could lead to higher degradation rate since the crystal segments are chemically more stable than the amorphous ones. In applications where mechanical support is not essential, but biodegradability is sought, an amorphous structure might be desirable.

6.2.2 Mechanical properties and degradation profile

Both the average modulus and average yield stress were broadly consistent over the 8-week period for all three materials. The addition of the short AW fibres slightly increased the flexural strength and elastic modulus of the scaffolds as printed. Angular shaped particles are preferred for reinforcement as they act as interlocks, decreasing the disruption between matrix and filler during mechanical testing. Unless used in high ratios, > 30% (Shikinami and Okuno, 1999; Tripathi, Choudhury and Basu, 2010), the use of bioceramic particles as reinforcement will not provide an improvement of mechanical properties, and are used instead to stimulate a response (Tripathi, Choudhury and Basu, 2010; Ramesh, Moratti and Dias, 2017). The slight improvement in initial mechanical properties of the fibre reinforced composite could be associated with factors such as fibre wetting. Fibres can retain heat which promotes material diffusion, resulting in improved bonding with the matrix, consequently a stronger material (Pipes *et al.*, 1991; Brenken *et al.*, 2018).

All samples remained stable under PBS immersion, with no mass loss reported. This suggests the sample is not degrading in bulk. The pH oscillated but stayed within the physiological range, ideal for implantation (Cüneyt Tas, 2000b). The NMR data (figure 47) suggests that the material is not suffering chemical degradation, which is supported by previous studies (Gaona *et al.*, 2012; Felfel *et al.*, 2013). This data is reinforced by the absence of changes in

the mechanical behaviour of the parts, and lack of defect sites and cracks that are common for PLLA hydrolytic degradation process (Cüneyt Tas, 2000b).

The ion release profile changes significantly only for the composites. Since Ca and Mg are easy to release from the structure, their presence is noted from week 1 (Hench and Clark, 1978a). The Ca and Mg are only present in the AW, suggesting they are being leached from exposed fibres and particles. Once they are consumed, the values drop, in this case by week 4, and are maintained relatively stable until the end. This suggests that the filler in no longer exposed and that the ions were consumed (Hench and Clark, 1978b). This release is gradual suggesting that there are multiple fibres and particles, possibly of different sizes or with different amounts exposed (Ahmed *et al.*, 2011; Felfel *et al.*, 2013). The lower leaching for the PLLA/AWp samples suggests that less of the AW is present at the surface of these composites. Smaller particles with a less rounded shape may be easier to submerge into the matrix as a result of the high shear stresses at the walls when the filament is extruded.

6.2.3 Bioactivity study

The bioactivity of the composite is dependent on the exposure of ceramic at the surface. A minimum bioceramic loading of 20% is advised in order to attain bioactivity (Wang, 2003). The SEM and EDS analysis, shows deposits on top of both composites, identified as Ca deficient apatite, with CaP ratio varying between 0.4 and 1.7, the latter close to bone apatite (1.67) (Mekmene *et al.*, 2009). This would improve osteoconductive behaviour and promote implant-bone bonding for both materials (Hench, 1991; Fu *et al.*, 2011). Both cauliflower and flake form apatite were detected at the biocomposite's surface. Cauliflower apatite is commonly observed as a product of bioactivity, but flake apatite is harder to produce once it demands the growth in specific crystalline planes (Lu *et al.*, 2005; Ekmene *et al.*, 2009).

6.2.4 Influence of samples in cell behaviour

6.2.4.1 Cells growth and morphology

The PLLA and PLLA/AWp materials showed no significant differences in terms of cell viability and proliferation, nonetheless PLLA/AWf and TCP cell numbers were significantly higher from day 7 onwards (figure 50a). Cells grew and proliferated in all types of samples, as observed in figure 51, presenting fibroblastic morphology at day 1 (typical of hMSCs), which evolved into pre osteoblastic at day 7. At day 21, cells evidenced a polygonal cell shape typical of osteoblasts (Di Silvio, Dalby and Bonfield, 1998; Marion and Mao, 2006;

Krishnan *et al.*, 2010; Sayin *et al.*, 2017) and ECM production. A high proliferation rate is common on TCP since its surface is treated to support cell growth (Skardal *et al.*, 2013). The main difference between samples was based on the proliferation rates for the PLLA/AWf material. Since both composites contains the same filler composition (AW precursor), degradability and higher ion release in PLLA/AWf (figure 48d and 48e) may stimulate cell growth however, further studies must be performed to assess these effects. To understand the ECM depositions at each time point, the concentration of sGAGS was estimated and visually observed using alcian blue staining (figure 54). It is known that GAGs are the major structural components of ECM, responsible for the maintenance of both its structure and organization (Robey *et al.*, 1993). In bone, the small sGAGS like biglycan, are present in the osteoid and progenitor cells, suggesting it participates in bone formation, including cell differentiation (Sommarin *et al.*, 1998). Later, other like decorin are expressed. It can bind to collagen type I, and its influence on the mineralisation process has been suggested. Studies have shown its significant decrease, or disappearance just before or during the bone mineralisation process. A later discovery revealed another proteoglycan, osteoadherin, which is mainly produced by mature osteoblasts. From this information is possible to understand the increasing amount of sGAGs (figure 54b). No investigation was done aiming the specific identification of the sGAGs being produced at each point, therefore they cannot be associated to any of the mentioned ones. These results are a demonstration of a constant and increased ECM production, positive regarding the cell proliferation and possibly cell development.

6.2.4.2 Cell differentiation and biomineralisation

In terms of ALP concentration, the samples only differed between each other at day 1, where PLLA and PLLA/AWp present a higher level of ALP production per cell (figure 52a) compared to PLLA/AWf and TCP. PLLA and PLLA/AWp appear to be more osteoinductive at first contact. Nevertheless, all three cultures produced differentiated cells by day 21 (figure 51, figure 52a and 52b). Osteogenesis can also be detected by increase in the production of collagen type I. The confocal imaging (figure 53) shows the presence of collagen type I increases significantly from day 7, for all types of samples. The production of collagen type I and type II by stem cells prior to differentiation is known (Stein, Lian and Owen, 1990; Marion and Mao, 2006; James *et al.*, 2015). Depending on the cell line, collagen type I gene is upregulated and collagen type II is downregulated during osteogenesis, after 7 and/or 14 days (Stein, Lian and Owen, 1990; Marion and Mao, 2006; Krishnan *et al.*, 2010; Astachov, Nevo and Vago, 2012b).

Following the differentiation of cells into osteoblasts, mineralisation occurs, characterised by a drop in ALP values and production of Ca deposits that are visible around the cells, trapped in ECM (Stein, Lian and Owen, 1990; James *et al.*, 2015). Although ALP is a common marker for MSCs differentiation, it does not predict the mineralisation stage or rate by itself (Štefková, Procházková and Pacherník, 2015; Abdallah *et al.*, 2016; Marklein *et al.*, 2016). Cells seeded on all samples produced ALP, but mineralisation was missing from the TCP control, and the mineral shape differed between the polymer and composite samples. PLLA/AWf showed consistent plate-like structures of CaP (figure 52b), whilst PLLA and PLLA/AWp evidenced small Ca deposits on top of the cells. To confirm and evaluate the amount of Ca and its distribution, alizarin red staining was performed and confirmed high levels of Ca at the surface of the samples, where a denser coating is visible for PLLA/AWf, compared to PLLA/AWp, which shows more mineralisation than PLLA.

6.3 Conclusion

Three types of samples were studied, PLLA and PLLA reinforced with AW particles and PLLA reinforced with AW fibres to assess their suitability as scaffolds for bone repair in critical size defects. Both polymer and biocomposites showed a good biocompatibility, and mechanical properties equivalent to cancellous bone, under degrading conditions, with the fibre reinforced composite performing better as produced. No mass loss is detected indicating the sample is not degrading in bulk up to 8 weeks therefore it could be used for long term applications. Its degradability can be tuned by increasing the AW content (Ahmed *et al.*, 2011; Felfel *et al.*, 2013). All samples promoted osteogenesis, however the biocomposites induced a higher degree of biomineralisation. The presence of Ca on top of the biocomposite samples indicated the material ability to induce apatite deposition, which was detected with SEM and alizarin red staining. This is an asset since once implanted there would be two sources of Ca, which would directly accelerate bone repair and regeneration. Overall both composites developed in this study could be used on critical size defects since the mechanical properties are within the range of cancellous bone and cells grew and proliferated in the scaffolds. AWf composites demonstrated higher ion leaching which rapidly stimulated cell proliferation and biomineralization, making them an interesting material to pursue.

Chapter 7. General discussion

7.1 Summary

The data presented in this thesis confirms the possibility to print devices for bone repair using different AM techniques, and materials. It highlights the importance of the material choice on the development of osteoinductive devices, and the influence of its quality in the manufacturing process. Emphasis is put on the processing methods, opting for a lean manufacturing model at all steps, proven to be ideal for industrial scale-up.

The first experimental chapter (chapter 4) explores the influence of surface contaminations, arising from the powder processing step of glass-ceramics. It was observed that these contaminations can attach to the powder particle's surface and hinder the material crystallisation during thermal treatment. It was also seen that the way the contaminant affects the process depends on the material's innate crystallisation mechanism. A material that crystallises via surface will only suffer changes in the crystallisation process, if the impurity is at the surface. When used as dopant, it does not produce a visible effect in the crystallisation of the material, but it does affect the development and amount of each crystalline phase. The presence of the dopant allows for higher control in the development of the microstructure, while maintaining crystallisation and mechanical performance.

Chapter 5 explores the printing of a powder blend with a small particle size range, theoretically considered out of printing range. It was proven that these blends, qualified as non/poor-flowing, can be printed using binder jetting, in a reproducible way. For this, compliance with the minimum amount of material needed for feedstock is key. The porosity values obtained were lower than the ones deemed as ideal for cell migration and proliferation, however the biological tests revealed that both were attained successfully. Adding to high cell viability, stem cell differentiation into osteoblasts, and consequent mineralisation, occurred. Despite the low amount of open porosity, cells were able to migrate inside the structure and were found in the centre of it, even after 21 days in culture. The mechanical properties obtained were lower than in previous work but also within the range of several studies reported in literature. Uncontrolled crystallisation of the structure and layer defects were deemed responsible for the decrease in effective modulus. These values impede the use of the struts for load bearing applications, emphasizing the fact that the raw material quality can change the outcome of the manufacturing process, and the application. In this case, the presence of a contaminant was considered valuable, and should be considered in the future. It

was also proven that the presence of crystallisation did not affect the bioactive character of the material, contrary to the results stated in literature.

Chapter 6 reports the successful development of osteoinductive polymer-ceramic biocomposites and explores the potential of fillers with different forms. A new technique was developed to blend the polymer and ceramic and proved to benefit the filler homogeneous distribution within the matrix. Using the developed biocomposite filaments, woodpile scaffolds were effectively manufactured using FFF, showing the potential of this technique to process particle and fibre filled biocomposite filaments in a reproducible way. The mechanical properties of the structure were within the range of cancellous bone and can be tuned by changing either filler amount and/or shape, and/or the design of the part. It also shown that a biological response can be attained for a minimum amount of filler in the matrix (5 wt%), which preserves the mechanical properties and integrity of the device, for the average time needed for bone repair. Furthermore, it is demonstrated the importance of the leached ions in the cell's response. The amount and timing of the leaching influenced both cell proliferation and differentiation. We proved the fillers leaching duration was different, and that the fibres high aspect ratio allows for higher exposure and longer leaching time, compared to the particulate biocomposite. This then reflected in the cell's response, however, in the end both promoted cell proliferation, differentiation and mineralisation.

7.2 Novelty

In this work it is presented novelty in three levels of the manufacturing process of a medical device: the material development, process optimisation and biological response.

- Firstly, the developed 2 types of AW glass-ceramic, doped with alumina, a known stabiliser (Lara *et al.*, 2004; Baino *et al.*, 2016). By comparing them to previously developed formulations, we attest that the influence of this dopant can be used to control or repress crystallisation, dependant on how it is placed in the material. This is of great value for the industry, since it allows for a better regulation and quality inspection of the raw materials (glasses and glass-ceramic precursors) prior to commercialisation. Also, it can aid the optimisation of the manufacturing process so that it is possible to produce AW bone implants with different glass formulations and obtain a wide range of abilities.
- Secondly, as seen in literature (Freiman & Hench 1972b; El-Kheshen et al. 2008), crystallisation benefits the mechanical properties of a part and therefore is desired for

load bearing applications. We prove that for glass-ceramics that is not applicable, and that uncontrolled crystallisation can indeed hinder the mechanical performance of a device. An element that was at first considered an impurity proved to be of value for the stabilisation of the material under heat treatment and can be used to tune the microstructure when added in different ways. It is also shown that these devices are osteoconductive. An accelerated cell response towards differentiation and mineralisation was noticed, present from the first week of cell contact with the device.

- Finally, FFF is used to process for the first time two types of osteoinductive biocomposites for bone repair, using only 5 wt% of filler loading. FFF has been used to print different composites for other applications (Brenken *et al.*, 2018), but none containing these raw materials and these filler forms (PLLA and AW particles and fibres). We exploit and prove the potential of this technique to fabricate osteoinductive devices, using its versatility, at the material and design level, as an advantage and opportunity to apply it in other areas.

7.3 Limitations of the techniques and devices

Throughout the execution of the project, several limitations were met regarding the techniques used, considering the processes should be simple and lean, to allow for an easy scale-up.

The production of AW pure and doped powder is time consuming and does not allow for the making of high quantities per batch. A maximum of 0.5-1 kg of glass was produced within 1 week, therefore decreasing the amount of experiments possible to perform. The glass was made within industrial context, and at the company site (GTS, Sheffield, UK) which meant limited time for production due the company's ongoing activities.

The binder jetting process relies on powder blend formulation, which is laborious and implies several powder processing steps. The minimum amount of powder needed to print is 0.5 kg, but it was stated that below 0.2 kg the prints fail due to layer dragging. Since the AW used for binder jetting underwent the same industrial fabrication process, a limited stock was available for the performance of more experiments. The resultant devices form the process have a low open porosity, and that influences the number of cells able to migrate inside the strut, as well has the number of layers formed before clogging the pore. The pore size must be bigger than 200 μm to allow multiple cell layers to form (Sachlos and Czernuszka, 2003; Willie *et al.*, 2010). In this work the pore size attained was below 100 μm, but cells were still able to migrate and colonize the implant. The processing technique, however, does allow for bigger

pore size ranges (Suwanprateeb *et al.*, 2009; Alharbi *et al.*, 2015; Mancuso *et al.*, 2017), a feature that makes it appealing for bone related applications. Despite the presence of cells inside the device, when translated to an *in vivo* model, these results would most likely differ due to exposure to higher number of cells that could cause pore clogging faster. The sintering process was optimised but the lack of control over the material crystallisation could represent a problem for the mechanical performance, limiting the range of applications.

Regarding the biocomposites production, the use of an extruder that does not allow matrix and filler to be mixed directly, implied the development of a pre-blending step, which adds a step to the manufacturing process. The blending process is long and has a limit for filler that can be added to the polymer (assuming successful physical bond). The filament was produced in-house and was highly dependent on human skill and manual control. This resulted in an uneven diameter (1.4-1.8 mm) which caused some prints to fail and originated defects in others, observable on the XCT analysis. Layer heterogeneity can lead to weaker parts, limiting the range of applications in scope. The presence of pores was also a result of poor layer deposition due to the filament incongruences. This reflects on the mechanical properties as a produced, and also during the exposure to body fluids which can accelerate the chemical degradation of the material (Ahmed *et al.*, 2011; Felfel *et al.*, 2013).

7.4 Potential clinical applications

Healing of bone fractures and reconstruction of critical-size defects is a significant challenge, since these do not heal spontaneously over the patient lifetime. Bone is a self-healing organ; however, this type of defect is highly dependent on 2 factors: 1) the surrounding tissue health, namely its vascularisation to allow nutrient access; 2) the MSCs present in bone marrow and periosteum, which are the osteoprogenitor cells. Secondary mechanisms influencing these cells include osteogenesis, osteoinduction and osteoconduction. At the fracture site, osteoinductive factors are delivered by the vascular network. In defects where vascularisation is limited, an external stimulus must be applied to induce the cells differentiation (Roddy *et al.*, 2018). In terms of osteoconduction within the human body, the osteoconductive platform is created via the formation of hematoma and cartilage callus, which then supports the osteoblast growth at the defect site (Roddy *et al.*, 2018). Clinically, the most commonly used treatments for critical size defects are bone grafts, distraction osteogenesis (DO) and induced membrane technique (Masquelet), but all have their own limitations. From these 3 procedures, DO and Masquelet are the ones used in load bearing areas and suitable for long bone treatment due to the use of metal fixation systems. Bone grafts are used on their own, and also

in combination with DO and Masquelet, to promote faster bone regeneration at the defect site (Roddy *et al.*, 2018).

None of the implants developed in this work reached the mechanical properties needed for load bearing areas, especially in long bone defects. The bioceramic scaffolds developed using binder jetting of AW, could compete with the current metal based devices (Kokubo *et al.*, 1982; Chang, Mao and Wu, 2000a; Mancuso *et al.*, 2017) but processing issues reflected on a decrease of the flexural strength of the printed implants. Changes in the processing and intensive study of the material properties (chapter 4), implied that the material composition should be improved, and the processing further optimised, so that values can better fit the needs of cortical bone, and therefore allow for the device to withstand the site loads. For that reason, the main potential clinical application area is bone substitutes.

Commercially available products used as bone substitutes are listed in table 26, and, on their own, all share the same issue: not suitable for loaded areas. These exist mainly under the form of granules, cements of injectable pastes. The presence of antibiotics also limits their use, especially during pregnancy and nursing, e.g. ChonOS and Palacos (R+G). There is a need for bone substitutes capable of supporting initial loading (minimum for cortical bone, ~ 50 MPa), without sourcing problems and size restrictions, and with an efficient manufacturing method. The production should allow for a versatile design able to be tailored to the defect site, which is not as accurate when the device consists of a granular filler or a mouldable cement and paste.

Commercial product and composition	Form/Use	Weaknesses
*Osteoset (Wright Medical Technology, USA). Calcium Sulphate + 4% tobramycin sulphate	Filler to be packed in defect	Not suitable for structural support. Dependent of patient compliance regarding substance use (drugs/alcohol). Hypercalcemia.
*ProStim (Wright Medical Technology, USA). Mixture of calcium sulphate, calcium phosphate and DBM	Filler to be packed in defect or in injectable form	
*ChonOS (Depuy Synthes, USA). TCP	Filler	Not suitable in the presence of infection, unclosed epiphyseal cartilage, segmental bone defects and areas of loading.
**Allomatrix (Wright Medical Technology, USA). DBM + calcium sulphate powder	Injectable gel and putty	Not suitable for structural support. Highly dependent on processing and donor variables
*Osteomatrix (Bioventus Surgical, USA). 40 % TCP 60% HA Type 1 collagen, purified (bovine)	Filler, < 30ml	Potential allergy to bovine collagen. Not suitable for children, pregnant women and individuals with osteomyelitis, and avascular sites.
*Palacos R and Palacos R+G (Zimmer Biomet, USA). PMMA (R) PMMA + gentamycin (R+G)	Cement	Not suitable for infectious sites, including infectious arthritis. R+G can't be applied in pregnant and during nursing period.
***Vitoss BBTRauma (Stryker, USA)	Bioglass porous scaffold	Not suitable for structural support. Fast degradation. Bioactivity of bioglass not proven in clinical trials. .
***Vitoss (Stryker, USA)	TCP-based bone graft	
***Vitoss BA (Stryker, USA)	Bioglass flexible foam	
***MEDPOR (Stryker, USA)	PE porous implant	

*(Lobb, DeGeorge and Chhabra, 2019); **(Gruskin *et al.*, 2012); *** (Stryker, 2019)

Table 26 - Current products available as bone grafts, suppliers and weaknesses associated their use.

In this work we present a new process for the development and manufacturing of bespoke osteoinductive, and osteoconductive resorbable biocomposites without the use of additives, surface treatment or differentiation media.

The biocomposite scaffolds developed here were intact after 8 weeks in degradation media, covering the period for initial bone repair, 35 days for low loading areas such as maxilla. The device mechanical performance will also depend on the bone formation throughout the healing period. The average bone remodelling rate is between 0.7-1 μm/day (Burr and Gallant, 2012), but these values are relative since the amount of remodelling depends on several factors such as age, site, surrounding tissue conditions and external stimulatory effects. Here, the biocomposite scaffolds have shown to enhancing biomineralization, therefore be of value for *in vitro* models.

Another potential option for the developed devices would be the use as a disease model for both bone and joints. Previous work (Rodrigues, 2018) using AW scaffolds and PLA hybrids attempted to mimic the bone tissue structure, where the porous bioceramic would act as the cortical fraction and the polymer as the trabeculae. *In vivo* testing showed that the hybrid structure improved bone growth when compared to AW. Also, it is suggested that the bioactivity of the AW influenced and enhanced cell migration and proliferation on the PLA fraction of the device. Advances in processing techniques such as AM permitted the creation of osteochondral scaffolds consisting of β-TCP and PEG based hydrogel, that structurally mirrored the bone-cartilage interface (Zhang *et al.*, 2015). The *in vitro* testing, was performed only for the bioceramic section of the device, showing satisfactory cell proliferation and ALP production by rabbit BMSCs (bone MSCs). Based on this, AW scaffolds printed with binder jetting could be used to create osteochondral plugs, when combined with cartilage-like materials such as hydrogels and other soft polymers (natural and/or synthetic).

Finally, from a commercial and manufacturing point of view, both binder jetting and FFF allow the production of samples with complex shapes but without the use of chemicals and other additives, which facilitates the process scale up to industrial level. This would permit the production of more devices faster and at a lower cost. The uniqueness of each device, and the design freedom provided by these techniques introduces a new option within the bone regenerative medicine market, where most of the approved products are in the form of injectable pastes and putties, pellets, powders and cements (Oryan *et al.*, 2014). The offer is still limited regarding 3D constructs, personalised or not, capable of producing the same

results attained by the ones in the market. This creates the perfect gap to insert devices, alone, or in combination with hMSCs, to promote and improve bone regeneration at the defect sites, or to be used for pharmaceutical testing when applied within disease model context.

Chapter 8. General conclusion and future recommendations

8.1 Conclusions

The research performed for this project allowed the understanding and development of new materials, from glass-doping to biocomposites comprising fillers with different shapes. The studied AM techniques allow the production of devices for bone repair in a controlled fashion, using both polymer and bioceramics, individually and combined. Overall, the aim of the project was fulfilled, leading to the major conclusions presented in the following sections.

8.1.1 AW processing

- Addition of alumina to the original AW glass formulation allowed the processing of 2 new glasses with different physicochemical properties.
- Extensive milling of powders with alumina containing balls, causes the attachment of alumina particles to the AW powder particles, creating a contamination with implications on the sintering process of parts.
- As a contaminant, above 0.14 wt%, alumina hindered the crystal growth during the crystallisation process but allowed for material processing at lower sintering temperatures.
- Doping AW powders with 0.14 wt% alumina improves the parts without affecting mechanical properties, while maintaining the crystallinity profile innate to the material.

8.1.2 Binder jetting and sintering

- Polydisperse blends made of irregular shaped particles with sizes < 90 μm have a poor printability. Binder jetting equipment should operate within a minimum amount of feedstock to avoid layer heterogeneity during processing.
- Crystallisation of AW scaffolds could be tuned without affecting the bioactivity and osteoconductivity of the material, at the expense of application range.
- Produced implants displayed osteoconductive properties, and allowed the differentiation of hMSCs into osteoblasts.

8.1.3 PLLA/AW biocomposite processing

- The developed method for the material blending enabled the creation of both particle and fibre reinforced composite filaments for FFF printing.
- Printing process of structures was repeatable and accurate without nozzle clogging or other mechanical issues.
- Defects arising from oscillation on filament diameter caused layer defects which led to the need of printing each scaffold individually.

8.1.4. FFF of PLLA/AW composites

- Both polymer and biocomposites showed a good biocompatibility, and mechanical properties equivalent to cancellous bone with the fibre reinforced composite performing better as produced.
- All three materials promoted osteogenesis, however the biocomposites induced a higher degree of biomineralisation.
- Both composite materials have potential for use in bone defects, with the AWf composite showing greater levels of ion release, stimulating more rapid cell proliferation and greater levels of mineralisation during cell assays.

8.2 Future recommendations

The worked developed in this project showed that both techniques, binder jetting and FFF, have the capability to manufacture devices for bone repair, and that different applications can be targeted for each. In the future, further analysis should be performed so that the next steps can be taken towards the industrialisation of the processes and the commercialisation of the devices.

8.2.1 Doping of AW powders with alumina for crystallisation control

Several steps should be taken in the future to further address the effects of alumina in the crystallisation process of AW parts, and to explore the benefits of this dopant in the mechanical properties of future bone implants.

- Here the AW powders contaminated at the surface with more than 0.68 wt% presented a crystalline profile below the microscale. Analysis of the microstructure should be

extended to the nanoscale to confirm the presence of nanocrystals and understand how the nucleation mechanism changes.

- Surface doping of the powders should be explored, whilst adopting a change in the milling process into an alumina free one. By surface doping the powder, the amount of crystallisation can be controlled in a repeatable way.
- Further studying how the alumina content affects the generation of glassy phase, and the cracking mechanism, can lead to the improvement of the process by inserting steps aiming to reduce internal stresses, and possibly to attain crystal orientation.
- Different protocols should be tried for the newly developed AW/alumina powders, to attempt an ideal balance between nucleation and crystal growth, and to in the future be able to improve the mechanical properties of the parts.

8.2.2 Binder Jetting of AW scaffolds for bone repair

The process of producing scaffolds using AW and MD is vastly reported, and a respectable catalogue of blends have been attempted and printed so far. Within the work developed in this project, and based on previous studies, a couple of parameters could be further optimised and understood.

- Explore how the crystallisation of the material is affecting the microstructure of the printed parts which are porous, by using doped powders as feedstock.
- Study the contribution of the crystallisation to the mechanical properties, to ensure it can be used as positive effect.
- Attempt to process the implants using different solid binders, and combinations of particle size and shape to avoid the drying step involved in the use of MD.
- Design different shapes and possibly combine other glasses in attempt to create ceramic on ceramic composites, proved to be useful in load bearing applications.

8.2.3 FFF of PLLA/AW biocomposites for bone repair

The composites developed in this work are unique, and so is their processing. For the first time these materials were 3D printed using FFF, to create scaffolds for bone repair. Being a first study on these, several issues must be addressed regarding the processing and also material and biological characterisation.

- The material blending process is limited in terms of filler amount usable. A new method should be developed if higher percentages of filler are to be explored.

- The filament manufacturing must be improved, and if possible, more controlled so that a consistent size is attained, matching the industry standards. This is particularly important for the acceleration of the manufacturing process. Several scaffolds could be made simultaneously, without the concern of excessive/insufficient deposition.
- Topographical studies would allow a better understanding of cell behaviour in different composites, namely targeting their migration and the influence on the proliferation.
- Genetic assay, namely PCR, would be an asset to further confirm the expression of genes related to differentiation and mineralisation, validating the previous results.
- Different filler shapes could be tested, in different amounts, to complete the repertoire of possible types of composite, as well other materials.

References

Abdallah, E. A. A. *et al.* (2016) 'Serial serum alkaline phosphatase as an early biomarker for osteopenia of prematurity', *Medicine*. Wolters Kluwer Health, 95(37), pp. e4837–e4837. doi: 10.1097/MD.0000000000004837.

Abou Neel, E. A. *et al.* (2009) 'Structure and properties of strontium-doped phosphate-based glasses', *Journal of the Royal Society, Interface*. 2008/09/30. The Royal Society, 6(34), pp. 435–446. doi: 10.1098/rsif.2008.0348.

Adamovic, D., Ristic, B. and Zivic, F. (2018) 'Review of existing biomaterials—method of material selection for specific applications in orthopedics - Biomaterials in clinical practice : advances in clinical research and medical devices', in Zivic, F. et al. (eds). Cham: Springer International Publishing, pp. 47–99. doi: 10.1007/978-3-319-68025-5_3.

AESCULAP implant systems (no date) *Plasmafit acetabular system with Vitelene Liner*. Available at: https://www.aesculapimplantsystems.com/plasmafit (Accessed: 13 April 2017).

Agarwal, B. D., Broutman, L. J. and Chandrashekhara, K. (2006) *Analysis and performance of fibre composites*. Third.

Ahmed, I. *et al.* (2011) 'Composites for bone repair : phosphate glass fibre reinforced PLA with varying fibre architecture', pp. 1825–1834. doi: 10.1007/s10856-011-4361-0.

Ahmetoglu, C. *et al.* (2009) 'Production and properties of Apatite-Wollastonite ceramics for biomedical applications', *InterCeram: International Ceramic Review*, 58, pp. 86–90.

Alharbi, N. *et al.* (2015) 'Processing of Apatite-Wollastonite (AW) glass-ceramic for three dimensional printing (3DP)', *Applied Mechanics and Materials*. Trans Tech Publications, 754–755, pp. 974–978. doi: 10.4028/www.scientific.net/AMM.754-755.974.

Alharbi, N. H. (2016) *Indirect three dimensional printing of Apatite-Wollasotnite structures for biomedical applications*. Newcastle University.

Astachov, L., Nevo, Z. and Vago, R. (2012a) 'Calcite biohybrids as microenvironment for stem cells', *Polymers*, 4, pp. 1065–1083. doi: 10.3390/polym4021065.

Astachov, L., Nevo, Z. and Vago, R. (2012b) *Calcite Biohybrids as Microenvironment for Stem Cells*, *Polymers*. doi: 10.3390/polym4021065.

Baino, F. *et al.* (2016) 'Design , selection and characterization of novel glasses and glass-ceramics for use in prosthetic applications', *Ceramics International*. Elsevier, 42(1), pp.

1482–1491. doi: 10.1016/j.ceramint.2015.09.094.

Bian, W. *et al.* (2016) ‘Morphological characteristics of cartilage-bone transitional structures in the human knee joint and CAD design of an osteochondral scaffold’, *BioMedical Engineering OnLine*, 15(1), p. 82. doi: 10.1186/s12938-016-0200-3.

Bignon, A. *et al.* (2003) ‘Effect of micro and macroporosity of bone substitutes on their mechanical properties and cellular response.’, *Journal of materials science. Materials in medicine*. United States, United States, 14(12), pp. 1089–1097.

Biomet (no date) *DVR anatomic plate*. Available at: http://ortomedic.no/images/uploads/product_brochures/DVR_brosjyre.pdf (Accessed: 13 April 2017).

Boccaccini, A. and Maquet, V. (2003) *Bioresorbable and bioactive polymer/bioglass composites with tailored pore structure for tissue engineering applications*, *Composites Science and Technology*. doi: 10.1016/S0266-3538(03)00275-6.

Bos, R. R. M. *et al.* (1987) ‘Resorbable poly (L-lactide) plates and screws for the fixation of zygomatic fractures’, *J. Oral. Maxillofac. Surg.*, 45, pp. 751–753.

Bottom, R. (2008) ‘Thermogravimetric Analysis’, in *Principles and Applications of Thermal Analysis*. Blackwell Publishing Ltd, pp. 87–118. doi: 10.1002/9780470697702.ch3.

Brenken, B. *et al.* (2018) ‘Fused filament fabrication of fiber-reinforced polymers: A review’, *Additive Manufacturing*, 21, pp. 1–16. doi: https://doi.org/10.1016/j.addma.2018.01.002.

Buck, D. and Dumanian, G. (2012) ‘Bone biology and physiology: part II. Clinical correlates.’, *Plast Reconstr Surg*, 129(6), pp. 950e-956e. doi: 10.1097/PRS.0b013e31824eca94.

Buck, D. W. and Dumanian, G. A. (2012) ‘Bone biology and physiology: Part I. The Fundamentals.’, *Plastic and reconstructive surgery*, 129(6), p. 1314. doi: 10.1097/PRS.0b013e31824ec354.

Burr, D. B. and Gallant, M. A. (2012) ‘Bone remodelling in osteoarthritis’, *Nature Reviews Rheumatology*. Nature Publishing Group, a division of Macmillan Publishers Limited. All Rights Reserved., 8, p. 665. Available at: https://doi.org/10.1038/nrrheum.2012.130.

Burstein, A. H., Reilly, D. T. and Martens, M. (1976) ‘Aging of bone tissue: mechanical properties’, *The Journal of Bone & Joint Surgery Joint Surgery*, 58(1), pp. 82 LP – 86.

Available at: http://jbjs.org/content/58/1/82.abstract.

Butscher, A. *et al.* (2011) 'Structural and material approaches to bone tissue engineering in powder-based three-dimensional printing', *Acta Biomaterialia*. Acta Materialia Inc., 7(3), pp. 907–920. doi: 10.1016/j.actbio.2010.09.039.

Butscher, A. *et al.* (2012) 'Printability of calcium phosphate powders for three-dimensional printing of tissue engineering scaffolds', *Acta Biomaterialia*. Acta Materialia Inc., 8(1), pp. 373–385. doi: 10.1016/j.actbio.2011.08.027.

Butscher, A. *et al.* (2013) 'Moisture based three-dimensional printing of calcium phosphate structures for scaffold engineering', *Acta Biomaterialia*. Acta Materialia Inc., 9(2), pp. 5369–5378. doi: 10.1016/j.actbio.2012.10.009.

Caffrey, T., Campbell, I. and Wholers, T. (2016) *Wohlers Report 2016*. Available at: https://wohlersassociates.com/press71.html (Accessed: 20 April 2017).

Cain, E. L. (2002) 'Stimulating Treatment', *Orthopedic Technology Review*, 4 (4).

Callister, W. D. and Rethwisch, D. G. (2007) *Materials science and engineering: an introduction*. Wiley New York.

De Campos, M. M. and Ferreira, M. D. C. (2013) 'A comparative analysis of the flow properties between two alumina-based dry powders', *Advances in Materials Science and Engineering*, 2013. doi: 10.1155/2013/519846.

Chan, O. *et al.* (2012) 'The effects of microporosity on osteoinduction of calcium phosphate bone graft substitute biomaterials', *Acta Biomaterialia*, 8(7), pp. 2788–2794. doi: https://doi.org/10.1016/j.actbio.2012.03.038.

Chang, C. K., Mao, D. L. and Wu, J. S. (2000a) 'Characteristics of crystals precipitated in sintered apatite-wollastonite glass ceramics', *Ceramics International*, 26(7), pp. 779–785. doi: https://doi.org/10.1016/S0272-8842(00)00019-5.

Chang, C. K., Mao, D. L. and Wu, J. S. (2000b) 'Characteristics of crystals precipitated in sintered apatite/wollastonite glass ceramics', *Ceramics International*. doi: 10.1016/S0272-8842(00)00019-5.

Christel, P. *et al.* (1989) 'Mechanical properties and short-term in vivo evaluation of yttrium-oxide-partially-stabilized zirconia', *Journal of Biomedical Materials Research*. John Wiley & Sons, Ltd, 23(1), pp. 45–61. doi: 10.1002/jbm.820230105.

Chu Liu, Xuanyong, P. K. (2008) *Biomaterials fabrication and processing handbook*. USA: Taylor & Francis Group, LLC.

Clarke, B. (2008) 'Normal bone anatomy and physiology.', *Clinical journal of the American Society of Nephrology : CJASN*, 3 Suppl 3, pp. 131–139. doi: 10.2215/CJN.04151206.

Clarke, K. I. *et al.* (1993) 'Investigation into the formation and mechanical properties of a bioactive material based on collagen and calcium phosphate', *Journal of Materials Science: Materials in Medicine*, 4(2), pp. 107–110. doi: 10.1007/BF00120378.

Cocca, M. *et al.* (2011) 'Influence of crystal polymorphism on mechanical and barrier properties of poly(l-lactic acid)', *European Polymer Journal*, 47(5), pp. 1073–1080. doi: https://doi.org/10.1016/j.eurpolymj.2011.02.009.

Costa, J. B. *et al.* (2018) 'Current advances in solid free-form techniques for osteochondral tissue engineering', *Bio-Design and Manufacturing*, 1(3), pp. 171–181. doi: 10.1007/s42242-018-0017-y.

Cüneyt Tas, A. (2000a) 'Synthesis of biomimetic Ca-hydroxyapatite powders at 37°C in synthetic body fluids', *Biomaterials*, 21(14), pp. 1429–1438. doi: https://doi.org/10.1016/S0142-9612(00)00019-3.

Cüneyt Tas, A. (2000b) 'Synthesis of biomimetic Ca-hydroxyapatite powders at 37°C in synthetic body fluids', *Biomaterials*, 21(14), pp. 1429–1438. doi: https://doi.org/10.1016/S0142-9612(00)00019-3.

Deckers, J., Vleugels, J. and Kruth, J. P. (2014) 'Additive manufacturing of ceramics: A review', *Journal of Ceramic Science and Technology*, 5(4), pp. 245–260. doi: 10.4416/JCST2014-00032.

Dionísio Viciosa, María Teresa, Wang, Yaming, Mano, João F., M. (2005) 'Glass transition dynamics of poly(L-lactic acid) during isothermal crystallisation monitored by real-time dielectric relaxation spectroscopy measurements', *Macromolecular Rapid Communications*, 26, pp. 1423–1427.

Du, Y. *et al.* (2017) 'Selective laser sintering scaffold with hierarchical architecture and gradient composition for osteochondral repair in rabbits', *Biomaterials*, 137, pp. 37–48. doi: https://doi.org/10.1016/j.biomaterials.2017.05.021.

Duminis, T., Shahid, S. and Hill, R. G. (2017) 'Apatite Glass-Ceramics: A Review', *Frontiers in Materials*, 3(January), pp. 1–15. doi: 10.3389/fmats.2016.00059.

Dyson, J. A. *et al.* (2007) ‘Development of custom built bone scaffolds using mesenchymal stem cells and apatite-wollastonite glass-ceramics’, *Tissue Engineering*, 13(12), pp. 2891–2901. doi: 10.1089/ten.2007.0124.

Einhorn, T. A. and Gerstenfeld, L. C. (2015) ‘Fracture healing: mechanisms and interventions’, *Nat Rev Rheumatol*. Nature Publishing Group, a division of Macmillan Publishers Limited. All Rights Reserved., 11(1), pp. 45–54. Available at: http://dx.doi.org/10.1038/nrrheum.2014.164.

Einhorn, T. a, Joint, J. B. and Am, S. (2007) ‘Enhancement of fracture-healing enhancement: Concepts review of fracture-healing’, *The Journal of Bone & Joint Surgery*, pp. 940–956.

Ekmene, O. M. *et al.* (2009) ‘Original article Effects of pH and Ca / P molar ratio on the quantity and crystalline structure of calcium phosphates obtained from aqueous solutions’, 89, pp. 301–316. doi: 10.1051/dst/2009019.

El-Kheshen, A. A. *et al.* (2008) ‘Effect of Al2O3 addition on bioactivity, thermal and mechanical properties of some bioactive glasses’, *Ceramics International*, 34(7), pp. 1667–1673. doi: https://doi.org/10.1016/j.ceramint.2007.05.016.

Emad, E.-M. and Van Noort, R. (2011) *Glasses and Glass Ceramics for Medical Applications*. Springer science & business media.

Endres, M. *et al.* (2003) ‘Osteogenic induction of human bone marrow-derived mesenchymal progenitor cells in novel synthetic polymer–hydrogel matrices’, *Tissue Engineering*. Mary Ann Liebert, Inc., publishers, 9(4), pp. 689–702. doi: 10.1089/107632703768247386.

Fatah, N. (2009) ‘Study and comparison of micronic and nanometric powders: Analysis of physical, flow and interparticle properties of powders’, *Powder Technology*, 190(1–2), pp. 41–47. doi: 10.1016/j.powtec.2008.04.055.

Felfel, R. M. *et al.* (2013) ‘Cytocompatibility, degradation, mechanical property retention and ion release profiles for phosphate glass fibre reinforced composite rods’, *Materials Science and Engineering C*. Elsevier B.V., 33(4), pp. 1914–1924. doi: 10.1016/j.msec.2012.12.089.

Ferreira, R. *et al.* (2017) ‘Experimental characterization and micrography of 3D printed PLA and PLA reinforced with short carbon fibers’, *Composites Part B: Engineering*, 124. doi: 10.1016/j.compositesb.2017.05.013.

Fielding, G. A., Bandyopadhyay, A. and Bose, S. (2012) ‘Effects of silica and zinc oxide doping on mechanical and biological properties of 3D printed tricalcium phosphate tissue

engineering scaffolds', *Dental Materials*, 28(2), pp. 113–122. doi: https://doi.org/10.1016/j.dental.2011.09.010.

Filho, O. P., La Torre, G. P. and Hench, L. L. (1996) 'Effect of crystallization on apatite-layer formation of bioactive glass 45S5', *Journal of Biomedical Materials Research*. John Wiley & Sons, Ltd, 30(4), pp. 509–514. doi: 10.1002/(SICI)1097-4636(199604)30:4<509::AID-JBM9>3.0.CO;2-T.

Fishcher, T. (2019) *Thermo Fischer scientific XRF technology*. Available at: http://www.thermofisher.com/za/en/home/industrial/spectroscopy-elemental-isotope-analysis/spectroscopy-elemental-isotope-analysis-learning-center/elemental-analysis-information/xrf-technology.html (Accessed: 11 May 2018).

Frankel, N. and Margareta, V. H. (2012) *Basic Biomechanics of the Musculoskeletal System*. 4th edn. Wolters Kuwer Health, Lippincontt Williams & Wilkins.

Freiman, S. W. and Hench, L. L. (1972) 'Effect of crystallization on the mechanical properties of Li2O-SiO2 glass-ceramics', *Journal of the American Ceramic Society*. John Wiley & Sons, Ltd (10.1111), 55(2), pp. 86–90. doi: 10.1111/j.1151-2916.1972.tb11216.x.

Fu, Q. *et al.* (2011) 'Bioactive glass scaffolds for bone tissue engineering: state of the art and future perspectives', *Materials Science and Engineering C*. Elsevier B.V., 31(7), pp. 1245–1256. doi: 10.1016/j.msec.2011.04.022.

Fujita, H. *et al.* (2000) 'Porous apatite-wollastonite glass-ceramic as an intramedullary plug', *The Journal of Bone and Joint Surgery*, pp. 1–5.

Ganesan, V., Rosentrater, K. A. and Muthukumarappan, K. (2008) 'Flowability and handling characteristics of bulk solids and powders – a review with implications for DDGS', *Biosystems Engineering*, 101(4), pp. 425–435. doi: https://doi.org/10.1016/j.biosystemseng.2008.09.008.

Ganguli, D. and Chatterjee, M. (1997) *Ceramic powder preparation: a handbook*. Springer.

Gao, C. *et al.* (2017) 'Bone biomaterials and interactions with stem cells', *Bone Research*. The Author(s), 5, p. 17059. Available at: https://doi.org/10.1038/boneres.2017.59.

Gao, W. *et al.* (2015) 'The status, challenges, and future of additive manufacturing in engineering', *Computer-Aided Design*. Elsevier Ltd, 69, pp. 65–89. doi: 10.1016/j.cad.2015.04.001.

Gaona, L. A. *et al.* (2012) ‘Hydrolytic degradation of PLLA/PCL microporous membranes prepared by freeze extraction’, *Polymer Degradation and Stability*, 97(9), pp. 1621–1632. doi: https://doi.org/10.1016/j.polymdegradstab.2012.06.031.

Geldart, D., Abdullah, E. C. and Verlinden, A. (2009) ‘Characterisation of dry powders’, *Powder Technology*, 190(1–2), pp. 70–74. doi: 10.1016/j.powtec.2008.04.089.

Gerhardt, L.-C. and Boccaccini, A. R. (2010) ‘Bioactive glass and glass-ceramic scaffolds for bone tissue engineering’, *Materials*, 3(7), pp. 3867–3910. doi: 10.3390/ma3073867.

Giannoudis, P., Psarakis, S. and Kontakis, G. (2007) ‘Can we accelerate fracture healing?. A critical analysis of the literature’, *Injury*, 38(SUPPL. 1). doi: 10.1016/j.injury.2007.02.013.

Gibson, I., Rosen, D. W. and Stucker, B. (2010) *Additive manufacturing technologies*. New York Springer.

Goldberg, A. J. and Burstone, C. J. (1992) ‘The use of continuous fiber reinforcement in dentistry’, (May), pp. 197–202.

Gomes, C. M. *et al.* (2014) ‘Designing apatite-wollastonite (AW) porous scaffolds by powder-based 3D printing’, *High Value Manufacturing: Advanced Research in Virtual and Rapid Prototyping*, (December 2015), pp. 159–163. doi: 10.1201/b15961-30.

Gomes, C. M., Zocca, A. and Guenster, J. (2015) *Designing apatite-wollastonite (AW) porous scaffolds by powder-based 3D printing*.

Goudouri, O. M., Balasubramanian, P. and Boccaccini, A. R. (2016) *Characterisation and Design of Tissue Scaffolds*, *Characterisation and Design of Tissue Scaffolds*. Elsevier. doi: 10.1016/B978-1-78242-087-3.00006-7.

Gruskin, E. *et al.* (2012) ‘Demineralized bone matrix in bone repair: History and use’, *Advanced Drug Delivery Reviews*, 64(12), pp. 1063–1077. doi: https://doi.org/10.1016/j.addr.2012.06.008.

Haeseker, B. (1988) ‘Mr. Job van Meekeren (1611-1666) and surgery of the hand.’, *Plastic and reconstructive surgery*. United States, 82(3), pp. 539–546.

Hatakeyma, W. *et al.* (2013) ‘Effects of apatite particle size in two apatite/collagen composites on the osteogenic differentiation profile of osteoblastic cells’, *International Journal of Molecular Medicine*. D.A. Spandidos, 32(6), pp. 1255–1261. doi: 10.3892/ijmm.2013.1516.

Hausner, H. H. (1981) ‘Powder characteristics and their effect on powder processing’, *Powder Technology*, 30(1), pp. 3–8. doi: https://doi.org/10.1016/0032-5910(81)85021-8.

Healey, J. H. *et al.* (1990) ‘Percutaneous bone marrow grafting of delayed union and nonunion in cancer patients.’, *Clinical orthopaedics and related research*, (256), pp. 280–285. doi: 10.1097/00003086-199007000-00039.

Hench, L. L. (1991) ‘Bioceramics: From Concept to Clinic’, *Journal of the American Ceramic Society*, 74(7), pp. 1487–1510. doi: 10.1111/j.1151-2916.1991.tb07132.x.

Hench, L. L. (1998) ‘Bioceramics’, *J. Am. Soc.*, 81 (7), pp. 1705–1728.

Hench, L. L. and Clark, D. E. (1978a) ‘Physical chemistry of glass surfaces’, *Journal of Non-Crystalline Solids*, 28(1), pp. 83–105. doi: https://doi.org/10.1016/0022-3093(78)90077-7.

Hench, L. L. and Clark, D. E. (1978b) ‘Physical chemistry of glass surfaces’, *Journal of Non-Crystalline Solids*, 28(1), pp. 83–105. doi: https://doi.org/10.1016/0022-3093(78)90077-7.

Henkel, J. *et al.* (2013) ‘Bone Regeneration Based on Tissue Engineering Conceptions — A 21st Century Perspective’, *Bone Research*. Sichuan University, 1, p. 216. doi: 10.4248/br201303002.

Hollister, S. J. (2005) ‘Porous scaffold design for tissue engineering’, *Nature materials*, 4(July), pp. 518–24. Available at: http://www.ncbi.nlm.nih.gov/pubmed/16003400.

Hrubý, A. (1972) ‘Evaluation of glass-forming tendency by means of DTA’, *Czechoslovak Journal of Physics B*, 22(11), pp. 1187–1193. doi: 10.1007/BF01690134.

Huang, W. *et al.* (2013) ‘Using spray-dried lactose monohydrate in wet granulation method for a low-dose oral formulation of a paliperidone derivative.’, *Powder Technology*, 246, pp. 379–394. doi: 10.1016/j.powtec.2013.05.042.

Hutmacher, D. W. (2000) ‘Scaffolds in tissue engineering bone and cartilage’, *Biomaterials*, 21(24), pp. 2529–2543. doi: http://dx.doi.org/10.1016/S0142-9612(00)00121-6.

James, S. *et al.* (2015) ‘Multiparameter analysis of human bone marrow stromal cells identifies distinct immunomodulatory and differentiation-competent subtypes’, *Stem Cell Reports*. The Authors, 4(6), pp. 1004–1015. doi: 10.1016/j.stemcr.2015.05.005.

Javaid, M. and Haleem, A. (2019) ‘Current status and challenges of Additive manufacturing in orthopaedics: An overview’, *Journal of Clinical Orthopaedics and Trauma*, 10(2), pp. 380–386. doi: https://doi.org/10.1016/j.jcot.2018.05.008.

Johnson, E. E., Urist, M. R. and Finerman, G. A. (1992) ‘Resistant nonunions and partial or complete segmental defects of long bones. Treatment with implants of a composite of human bone morphogenetic protein (BMP) and autolyzed, antigen-extracted, allogeneic (AAA) bone.’, *Clinical orthopaedics and related research*, 277(277), pp. 229–37. Available at: http://www.ncbi.nlm.nih.gov/pubmed/1555346.

Jones, J. R. and Hench, L. L. (2006) ‘Biomaterials: Bioceramics’, in *Encyclopedia of Medical Devices and Instrumentation*. John Wiley & Sons, Inc. doi: 10.1002/0471732877.emd024.

Joshi, V. S. *et al.* (2013) ‘Macroporosity enhances vascularization of electrospun scaffolds’, *Journal of Surgical Research*, 183(1), pp. 18–26. doi: http://dx.doi.org/10.1016/j.jss.2013.01.005.

Juhasz, J. A. *et al.* (2004) ‘Mechanical properties of glass-ceramic A–W-polyethylene composites: effect of filler content and particle size’, *Biomaterials*. Elsevier, 25(6), pp. 949–955. doi: 10.1016/J.BIOMATERIALS.2003.07.005.

K.H. Jürgen Buschow, Robert W. Cahn, P. V. (3001) ‘Bone Mineralization’, in *Encyclopedia of Materials: Science and Technology*. Elsevier Ltd, p. 10388. Available at: https://www.sciencedirect.com/topics/engineering/bone-apatite/pdf.

Kalsoom, U., Nesterenko, N. and Paull, B. (2016) ‘Recent developments in 3D printable composite materials’, *RSC Advances*. Royal Society of Chemistry, 6, pp. 60355–60371. doi: 10.1039/C6RA11334F.

Keaveny, T. M. and Hayes, W. C. (1993) ‘Mechanical properties of cortical and trabecular bone’, *Bone*. CRC Pres, Boca Raton, FL, 7, pp. 285–344.

Khang Kim, Moon Suk, Less, Hai Bang, G. and Ltd., W. S. P. C. P. (2007) *A manual for biomaterials/scaffold fabrication technology, Manuals in Biomedical Research*.

Kim, S. S. *et al.* (1998) ‘Survival and function of hepatocytes on a novel three-dimensional synthetic biodegradable polymer scaffold with an intrinsic network of channels’, *Annals of surgery*, 228(1), pp. 8–13. Available at: https://www.ncbi.nlm.nih.gov/pubmed/9671060.

Kokosis, G. *et al.* (2016) ‘Mandibular reconstruction using the free vascularized fibula graft: an overview of different modifications’, *Archives of Plastic Surgery*. The Korean Society of Plastic and Reconstructive Surgeons, 43(1), pp. 3–9. doi: 10.5999/aps.2016.43.1.3.

Kokubo, T. *et al.* (1982) ‘Apatite and Wollastonite containing glass-ceramics for prosthetic application’, *Bulletin of the Institute for Chemical Research*, 60(3–4), pp. 260–268.

Kokubo, T. *et al.* (1985) ‘Mechanical properties of a new type of apatite-containing glass-ceramic for prosthetic application’, *Journal of Materials Science*, 20(6), pp. 2001–2004. doi: 10.1007/BF01112282.

Kokubo, T. (1991) ‘Bioactive glass ceramics: properties and applications’, *Biomaterials*. Elsevier, 12(2), pp. 155–163.

Kokubo, T. (2008) *Bioceramics and their clinical applications*. Elsevier.

Kokubo, T., Kim, H. M. and Kawashita, M. (2003) ‘Novel bioactive materials with different mechanical properties’, *Biomaterials*, 24(13), pp. 2161–2175. doi: 10.1016/S0142-9612(03)00044-9.

Kokubo, T. and Takadama, H. (2006) ‘How useful is SBF in predicting in vivo bone bioactivity?’, *Biomaterials*, 27(15), pp. 2907–2915. doi: https://doi.org/10.1016/j.biomaterials.2006.01.017.

Krishnan, V. *et al.* (2010) ‘Osteogenesis in vitro: from pre-osteoblasts to osteocytes: a contribution from the Osteobiology Research Group, The Pennsylvania State University.’, *In vitro cellular & developmental biology. Animal*. Germany, Germany, 46(1), pp. 28–35. doi: 10.1007/s11626-009-9238-x.

Ladizesky, H. N., Ward, I. and Bonfield, W. (1997) *Hydrostatic extrusion of polyethylene filled with hydroxyapatite, Polymers for Advanced Technologies*. doi: 10.1002/(SICI)1099-1581(199708)8:8<496::AID-PAT676>3.0.CO;2-R.

Lam, C. X. F. *et al.* (2002) ‘Scaffold development using 3D printing with a starch-based polymer’, *Materials Science and Engineering: C*, 20(1), pp. 49–56. doi: https://doi.org/10.1016/S0928-4931(02)00012-7.

Lanzetta, M. and Sachs, E. (2003) ‘Improved surface finish in 3D printing using bimodal powder distribution’, *Rapid Prototyping Journal*, 9(3), pp. 157–166. doi: 10.1108/13552540310477463.

Lara, C. *et al.* (2004) ‘Sintering of glasses in the system RO-Al2O3-BaO- SiO2 (R=Ca, Mg, Zn) studied by hot-stage microscopy’, *Solid State Ionics*, 170(3–4), pp. 201–208. doi: 10.1016/j.ssi.2004.03.009.

Laurencin, C. T. and Freeman, J. W. (2005) ‘Ligament tissue engineering: An evolutionary materials science approach’, *Biomaterials*, 26(36), pp. 7530–7536. doi: https://doi.org/10.1016/j.biomaterials.2005.05.073.

Lee, E. J., Kim, H. W. and Knowles, J. C. (2014) ‘Ceramic biomaterials as tissue scaffolds’, *Stem Cell Biology and Tissue Engineering in Dental Sciences*. Elsevier Inc., pp. 163–174. doi: 10.1016/B978-0-12-397157-9.00014-X.

Lee, J. A. *et al.* (2015) ‘In vivo biocompatibility of custom-fabricated apatite-wollastonite-mesenchymal stromal cell constructs’, *Journal of Biomedical Materials Research Part A*, 103(10), pp. 3188–3200. doi: 10.1002/jbm.a.35448.

Lee, W. E. (1996) ‘Ceramic processing and sintering’, *International Materials Reviews*, 41(1), pp. 36–37. doi: 10.1179/095066096790151286.

Li, H. C., Wang, D. G. and Chen, C. Z. (2015) ‘Effect of zinc oxide and zirconia on structure, degradability and in vitro bioactivity of wollastonite’, *Ceramics International*, 41(8), pp. 10160–10169. doi: 10.1016/j.ceramint.2015.04.117.

LINK (no date) *LCU prosthesis*. Available at: https://www.linkorthopaedics.com/en/for-the-physician/products/huefte/primary/stems-cementless/lcu/ (Accessed: 13 April 2017).

Lobb, D. C., DeGeorge, B. R. and Chhabra, A. B. (2019) ‘Bone Graft Substitutes: Current Concepts and Future Expectations’, *The Journal of Hand Surgery*, 44(6), pp. 497-505.e2. doi: https://doi.org/10.1016/j.jhsa.2018.10.032.

Lorrison, J. C., Dalgarno, K. W. and Wood, D. J. (2005) ‘Processing of an apatite-mullite glass-ceramic and an hydroxyapatite/phosphate glass composite by selective laser sintering’, *Journal of Materials Science: Materials in Medicine*, 16(8), pp. 775–781. doi: 10.1007/s10856-005-2616-3.

Loty, C. *et al.* (2000) ‘In vitro bone formation on a bone-like apatite layer prepared by a biomimetic process on a bioactive glass-ceramic’, *Journal of Biomedical Materials Research*, 49(4), pp. 423–434. doi: 10.1002/(SICI)1097-4636(20000315)49:4<423::AID-JBM1>3.0.CO;2-7.

Lu, H. H. *et al.* (2005) ‘Compositional effects on the formation of a calcium phosphate layer and the response of osteoblast-like cells on polymer-bioactive glass composites’, *Biomaterials*, 26, pp. 6323–6334. doi: 10.1016/j.biomaterials.2005.04.005.

Lv, X. *et al.* (2019) ‘Binder jetting of ceramics: Powders, binders, printing parameters, equipment, and post-treatment’, *Ceramics International*, 45(10), pp. 12609–12624. doi: https://doi.org/10.1016/j.ceramint.2019.04.012.

Ma, P. X. *et al.* (2000) ‘Engineering new bone tissue in vitro on highly porous poly (hydroxyl

acids)/ hydroxyapatite composite scaffolds', *J Biomed Mater Res.*, 54(2)(Feb), pp. 1–3.

Malvern Ltd (2019) *Mastersizer - particle size analyser*. Available at: http://www.malvern.com/en/products/product-range/mastersizer-range/mastersizer-3000/default.aspx (Accessed: 9 March 2016).

Mancuso, E. (2016) 'Processing and characterisation of novel bioceramics for load bearing applications', (April).

Mancuso, E. *et al.* (2017) 'Three-dimensional printing of porous load-bearing bioceramic scaffolds', *Proceedings of the Institution of Mechanical Engineers, Part H: Journal of Engineering in Medicine*, p. 095441191668298. doi: 10.1177/0954411916682984.

Manicone, P., Rossi Iommetti, P. and Raffaelli, L. (2007) *An Overview of Zirconia Ceramics: Basic Properties and Clinical Applications, Journal of dentistry*. doi: 10.1016/j.jdent.2007.07.008.

Marion, N. W. and Mao, J. J. (2006) 'Mesenchymal Stem Cells and Tissue Engineering', 6879(06). doi: 10.1016/S0076-6879(06)20016-8.Mesenchymal.

marketsandmarkets.com (2016) *Bioceramics and Piezoceramics Market by Material (Bio-Inert, Bio-Active, & Bio-Resorbable Ceramics, Piezo Ceramcis), by Application (Dental & Orthopedic Implants, Surgical, & Diagnostic Instrument, Implanatable Electronic Devices), by Region - Global Fore*. Available at: http://www.marketsandmarkets.com/Market-Reports/medical-ceramics-market-3496695.html.

Marklein, R. A. *et al.* (2016) 'High Content Imaging of Early Morphological Signatures Predicts Long Term Mineralization Capacity of Human Mesenchymal Stem Cells upon Osteogenic Induction', *STEM CELLS*. John Wiley & Sons, Ltd, 34(4), pp. 935–947. doi: 10.1002/stem.2322.

Marsell, R. and Einhorn, T. A. (2012) 'The biology of fracture healing', *Injury*, 42(6), pp. 551–555. doi: 10.1016/j.injury.2011.03.031.THE.

Massera, J. *et al.* (2015) 'Crystallization behavior of phosphate glasses and its impact on the glasses' bioactivity', *Journal of Materials Science*, 50(8), pp. 3091–3102. doi: 10.1007/s10853-015-8869-4.

Medical Expo (no date) *CEMFIX 3 by Teknimed*. Available at: http://www.medicalexpo.com/prod/teknimed/product-70291-547739.html (Accessed: 13 April 2017).

Mekmene, O. *et al.* (2009) ‘Effects of pH and Ca/P molar ratio on the quantity and crystalline structure of calcium phosphates obtained from aqueous solutions’, *Dairy Science & Technology*, 89(3), pp. 301–316. doi: 10.1051/dst/2009019.

Melo, P. (2014) *Electromechanical Poly(L-lactic acid) PLLA platforms for regenerative medicine*. Universidade de Aveiro. Available at: https://ria.ua.pt/handle/10773/15135.

Melo, P. *et al.* (2019) ‘Short phosphate glass fiber - PLLA composite to promote bone mineralization’, *Materials Science and Engineering: C*, 104, p. 109929. doi: https://doi.org/10.1016/j.msec.2019.109929.

Meyer Thomas *et al.* (2009) ‘Fundamentals of tissue enginerring and regenerative medicine’. Springer-Verlag Berlin Heidelberg.

Miola, M. *et al.* (2014) ‘In vitro study of manganese-doped bioactive glasses for bone regeneration.’, *Materials science & engineering. C, Materials for biological applications*. Netherlands, Netherlands, 38, pp. 107–118. doi: 10.1016/j.msec.2014.01.045.

Mistry, A. S. and A. G. M. (2005) ‘Tissue Engineering Strategies for Bone Regeneration’, *Adv Biochem Engin/Biotechnol*, 94, pp. 1–22.

Morris, S. *et al.* (2016) ‘Complex functional surface design for additive manufacturing’, *Conference: 26th Solid Freeform Fabrication Symposium*, pp. 1–5.

Murphy, S. *et al.* (2009) ‘The effect of composition on ion release from Ca-Sr-Na-Zn-Si glass bone grafts.’, *Journal of materials science. Materials in medicine*. United States, United States, 20(11), pp. 2207–2214. doi: 10.1007/s10856-009-3789-y.

Navarro, M. *et al.* (2008) ‘Biomaterials in orthopaedics’, (July), pp. 1137–1158. doi: 10.1098/rsif.2008.0151.

Ning, F. *et al.* (2015) ‘Additive manufacturing of carbon fiber reinforced thermoplastic composites using fused deposition modeling’, *Composites Part B: Engineering*, 80, pp. 369–378. doi: https://doi.org/10.1016/j.compositesb.2015.06.013.

Nordin, M. and Frankel, V. H. (2012) *Basic Biomechanics of the musculoskeletal system*. fourth. Lippincott Williams & Wilkins.

Ohtsuki, C., Kamitakahara, M. and Miyazaki, T. (2009) ‘Bioactive ceramic-based materials with designed reactivity for bone tissue regeneration.’, *Journal of the Royal Society, Interface / the Royal Society*, 6 Suppl 3(January), pp. S349–S360. doi: 10.1098/rsif.2008.0419.focus.

Oryan, A. *et al.* (2014) ‘Bone regenerative medicine: classic options, novel strategies, and future directions’, *Journal of Orthopaedic Surgery and Research*, 9(1), p. 18. doi: 10.1186/1749-799X-9-18.

Oscar, P. M., Bellini, F. E. and Dutra, Z. E. (2012) ‘Sintering Kinetics of Crystallizing Glass Particles. A Review’, *Melt Chemistry, Relaxation, and Solidification Kinetics of Glasses*. (Wiley Online Books). doi: doi:10.1002/9781118408063.ch13.

Ovsianikov, A., Yoo, J. and Mironov, V. (2018) *3D Printing and Biofabrication*. Springer International Publishing. Available at: https://link.springer.com/referencework/10.1007%2F978-3-319-45444-3.

Panna, W., Wyszomirski, P. and Kohut, P. (2016) ‘Application of hot-stage microscopy to evaluating sample morphology changes on heating’, *Journal of Thermal Analysis and Calorimetry*. Springer Netherlands, 125(3), pp. 1053–1059. doi: 10.1007/s10973-016-5323-z.

Park, J. *et al.* (2010) ‘Tribological behavior of alumina-added apatite–wollastonite glass–ceramics in simulated body fluid’, *Materials Chemistry and Physics*, 124(1), pp. 113–119. doi: https://doi.org/10.1016/j.matchemphys.2010.06.001.

Park, J. (2013) *Bioceramics: Properties, characterizations and applications.*

Peterson, D. R. and Bronzino, J. D. (2008) *Biomechanical Principles and Application, CRC Press*.

Pipes, R. B. *et al.* (1991) ‘A constitutive relation for the viscous flow of an oriented fiber assembly’, *Journal of Composite Materials*. SAGE Publications Ltd STM, 25(9), pp. 1204–1217. doi: 10.1177/002199839102500907.

Poitout, D. G. (2004) *Biomechanics and orthopedics*. Edited by Springer-Verlag. London.

Pooria Moghadam, G., Tohidi, T. and Ranjbar, B. (2010) ‘Differential Scanning Calorimetry Techniques: Applications in Biology and Nanoscience’, 21, pp. 167–193.

Rabinovich, I. B., Labashov, A. A. and Kucheryavyi, V. I. (1960) ‘No Title’, *Russ. J. Phys. Chem*, 34(1046).

Rahman, M. S. *et al.* (2015) ‘TGF-β/BMP signaling and other molecular events: regulation of osteoblastogenesis and bone formation’, *Bone Research*, 3(November 2014), p. 15005. doi: 10.1038/boneres.2015.5.

Raja, K. C. M. *et al.* (1989) ‘Material characterization studies of maltodextrin samples for the

use of wall material', *Starch - Stärke*, 41(8), pp. 298–303. doi: 10.1002/star.19890410805.

Ramesh, N., Moratti, S. C. and Dias, G. J. (2017) 'Hydroxyapatite–polymer biocomposites for bone regeneration: A review of current trends', *Journal of Biomedical Materials Research Part B: Applied Biomaterials*. John Wiley & Sons, Ltd, 106(5), pp. 2046–2057. doi: 10.1002/jbm.b.33950.

Ratner, B. D. *et al.* (2004) *Biomaterials science: an introduction to materials in medicine*. Academic press.

Robey, P. G. *et al.* (1993) 'Structure and molecular regulation of bone matrix proteins', *Journal of Bone and Mineral Research*. John Wiley & Sons, Ltd, 8(S2), pp. S483–S487. doi: 10.1002/jbmr.5650081310.

Roddy, E. *et al.* (2018) 'Treatment of critical - sized bone defects : clinical and tissue engineering perspectives', *European Journal of Orthopaedic Surgery & Traumatology*. Springer Paris, 28(3), pp. 351–362. doi: 10.1007/s00590-017-2063-0.

Rodrigues, N. (2018) *Materials processing and physical characterisation of a hybrid composite structure for bone replacement applications*. Newcastle University.

Sachlos, E. and Czernuszka, J. T. (2003) 'Making tissue engineering scaffolds work. Review: the application of solid freeform fabrication technology to the production of tissue engineering scaffolds', *Eur Cell Mater*, 5(29), pp. 39–40.

Sayin, E. *et al.* (2017) 'Human adipose derived stem cells are superior to human osteoblasts (HOB) in bone tissue engineering on a collagen-fibroin-ELR blend', *Bioactive Materials*, 2(2), pp. 71–81. doi: https://doi.org/10.1016/j.bioactmat.2017.04.001.

Shah, F. A., Thomsen, P. and Palmquist, A. (2019) 'Osseointegration and current interpretations of the bone-implant interface', *Acta Biomaterialia*, 84, pp. 1–15. doi: https://doi.org/10.1016/j.actbio.2018.11.018.

Shareef, M. Y. (2018) 'Biomaterials and Their Medical Applications', *United Journal of Chemistry*, 1(2), pp. 172–183.

Shikinami, Y. and Okuno, M. (1999) 'Bioresorbable devices made of forged composites of hydroxyapatite (HA) particles and poly- L -lactide (PLLA): Part I . Basic characteristics', 20, pp. 859–877.

Shofner, M. L. *et al.* (2003) 'Nanofiber-reinforced polymers prepared by fused deposition

modeling', *Journal of Applied Polymer Science*. John Wiley & Sons, Ltd, 89(11), pp. 3081–3090. doi: 10.1002/app.12496.

Di Silvio, L., Dalby, M. and Bonfield, W. (1998) 'In vitro response of osteoblasts to hydroxyapatite-reinforced polyethylene composites', *Journal of Materials Science: Materials in Medicine*, 9, pp. 845–848.

Skardal, A. *et al.* (2013) 'Substrate elasticity controls cell proliferation, surface marker expression and motile phenotype in amniotic fluid-derived stem cells', *Journal of the mechanical behavior of biomedical materials*. 2012/10/11, 17, pp. 307–316. doi: 10.1016/j.jmbbm.2012.10.001.

Sobieszczyk, S. (2010) 'Optimal features of porosity of Ti alloys considering their bioactivity and mechanical properties', *Advances in Materials Sciences*. Versita, 10(2), pp. 20–30.

Sommarin, Y. *et al.* (1998) 'Osteoadherin, a Cell-binding Keratan Sulfate Proteoglycan in Bone, Belongs to the Family of Leucine-rich Repeat Proteins of the Extracellular Matrix', *Journal of Biological Chemistry* , 273(27), pp. 16723–16729. Available at: http://www.jbc.org/content/273/27/16723.abstract.

Štefková, K., Procházková, J. and Pacherník, J. (2015) 'Alkaline phosphatase in stem cells', *Stem cells international*. 2015/02/12. Hindawi Publishing Corporation, 2015, p. 628368. doi: 10.1155/2015/628368.

Stein, G. S., Lian, J. B. and Owen, T. A. (1990) 'Relationship of cell growth to the regulation of tissue-specific gene expression during osteoblast differentiation.', *FASEB journal : official publication of the Federation of American Societies for Experimental Biology*. United States, United States, 4(13), pp. 3111–3123.

Stryker (2019) *Stryker, Official website*. Available at: https://www.stryker.com/us/en/index.html (Accessed: 18 September 2019).

Sukegawa, S. *et al.* (2016) 'Clinical evaluation of an unsintered hydroxyapatite / poly-L-Lactide osteoconductive composite device for the internal fixation of maxillofacial fractures', *Journal of Craniofacial Surgery*, 27(6), pp. 1391–1397. doi: 10.1097/SCS.0000000000002828.

Suuronen, R. (1993) 'Biodegradable fracture-fixation devices in maxillofacial surgery', *Int. J. Oral Maxillofac. Surg*, 22, pp. 50–57.

Suwanprateeb, J. *et al.* (2009) 'Mechanical and in vitro performance of apatite--wollastonite

glass ceramic reinforced hydroxyapatite composite fabricated by 3D-printing', *Journal of Materials Science: Materials in Medicine*, 20(6), p. 1281. doi: 10.1007/s10856-009-3697-1.

Suwanprateeb, J. *et al.* (2012) 'Influence of printing parameters on the transformation efficiency of 3D-printed plaster of paris to hydroxyapatite and its properties', *Rapid Prototyping Journal*, 18, pp. 490–499. doi: 10.1108/13552541211272036.

Suwanprateeb, J., Sanngam, R. and Panyathanmaporn, T. (2010) 'Influence of raw powder preparation routes on properties of hydroxyapatite fabricated by 3D printing technique', *Materials Science and Engineering: C*, 30(4), pp. 610–617. doi: https://doi.org/10.1016/j.msec.2010.02.014.

Suwanprateeb, J., Sanngam, R. and Suwanpreuk, W. (2008) 'Fabrication of bioactive hydroxyapatite/bis-GMA based composite via three dimensional printing', *Journal of Materials Science: Materials in Medicine*, 19(7), pp. 2637–2645. doi: 10.1007/s10856-007-3362-5.

Swift, T. *et al.* (2017) 'Analysis using size exclusion chromatography of poly(N-isopropyl acrylamide) using methanol as an eluent', *Journal of Chromatography A*, 1508, pp. 16–23. doi: https://doi.org/10.1016/j.chroma.2017.05.050.

Szucs, T. and Brabazon, D. (2009) 'Effect of Saturation and Post Processing on 3D Printed Calcium Phosphate Scaffolds', *Key engineering materials*, 396–398, pp. 663–666. doi: 10.4028/0-87849-353-0.663.

Technavio (2016) *Global bioactive materials market 2016-2020*. Available at: http://www.businesswire.com/news/home/20161024006506/en/Bioactive-Materials-Market-Impressive-Growth-CAGR-13.42.

Technologies, S. medical (no date) *Vertebro X by SOMATEX*. Available at: http://www.medicalexpo.com/prod/somatex-medical-technologies-gmbh/product-84863-551901.html (Accessed: 13 April 2017).

Tripathi, G., Choudhury, P. and Basu, B. (2010) 'Development of polymer based biocomposites: a review', *Materials Technology*. Taylor & Francis, 25(3–4), pp. 158–176. doi: 10.1179/175355510X12723642365089.

Venugopal, J. *et al.* (2010) 'Biomimetic hydroxyapatite-containing composite nanofibrous substrates for bone tissue engineering', *Philosophical Transactions of the Royal Society A: Mathematical, Physical and Engineering Sciences*, 368(1917), pp. 2065 LP – 2081. Available

at: http://rsta.royalsocietypublishing.org/content/368/1917/2065.abstract.

Vlasea, M. *et al.* (2010) 'Additive manufacturing of scaffolds for tissue engineering of bone and cartilage', *International Journal of Advanced Manufacturing Systems*, 13(1), pp. 129–147.

Wang, M. (2003) 'Developing bioactive composite materials for tissue replacement', *Biomaterials*, 24(October 2002), pp. 2133–2151. doi: 10.1016/S0142-9612(03)00037-1.

Wang, M., Kukobo, T. and Bonfield, W. (1996) 'A-W glass-ceramic reinforced polyethylene for medical applications', *Bioceramics*, 9, pp. 387–390. Available at: http://scholar.google.com/scholar?q=A-W+glass-ceramic+reinforced+polyethylene+for+medical+applications#0%5Cnhttp://www.amazon.com/Bioceramics-Volume-9-Tadashi-Kokubo/dp/0080426840/ref=sr_1_2?ie=UTF8&qid=1382407820&sr=8-2&keywords=bioceramics+kokubo.

Wang, M., L Hench, L. and Bonfield, W. (1999) *Bioglass®/high density polyethylene composite for soft tissue applications: Preparation and evaluation*, *Journal of biomedical materials research*. doi: 10.1002/(SICI)1097-4636(19981215)42:43.0.CO;2-2.

Wang, M., Porter, D. and Bonfield, W. (1994) *Processing, Characterization, and Evaluation of Hydroxyapatite Reinforced Polyethylene Composites*, *British Ceramic Transactions*.

Wang, M., Weng, J. and Poret, K. (2001) 'Manufacture and characterisation of biodegradable composites consisting of bioceramics and chitin', in *Proceedings of the 13th International Conference on Composite Materials (ICCM-13)*, p. 1547.

Wang, W. and Yeung, K. W. K. (2017) 'Bone grafts and biomaterials substitutes for bone defect repair: A review', *Bioactive Materials*, 2(4), pp. 224–247. doi: https://doi.org/10.1016/j.bioactmat.2017.05.007.

Wang, X. *et al.* (2000) 'Effect of collagen denaturation on the toughness of bone.', *Clinical orthopaedics and related research*, (371), pp. 228–39. doi: 10.1097/00003086-200002000-00027.

Williams, J. M. *et al.* (2005) 'Bone tissue engineering using polycaprolactone scaffolds fabricated via selective laser sintering', *Biomaterials*, 26(23), pp. 4817–4827. doi: 10.1016/j.biomaterials.2004.11.057.

Willie, B. M. *et al.* (2010) 'Designing biomimetic scaffolds for bone regeneration: why aim

for a copy of mature tissue properties if nature uses a different approach?', *Soft Matter*. The Royal Society of Chemistry, 6(20), pp. 4976–4987. doi: 10.1039/c0sm00262c.

Winkler, T. *et al.* (2018) 'A review of biomaterials in bone defect healing, remaining shortcomings and future opportunities for bone tissue engineering', *Bone & Joint Research*. The British Editorial Society of Bone & Joint Surgery, 7(3), pp. 232–243. doi: 10.1302/2046-3758.73.BJR-2017-0270.R1.

Wohlers, T. T. *et al.* (2018) *Wohlers Report 2018*.

Wong, K. V. and Hernandez, A. (2012) 'A Review of Additive Manufacturing', *ISRN Mechanical Engineering*, 2012, pp. 1–10. doi: 10.5402/2012/208760.

Wopenka, B. and Pasteris, J. D. (2005) 'A mineralogical perspective on the apatite in bone', *Materials Science and Engineering C*, 25(2), pp. 131–143. doi: 10.1016/j.msec.2005.01.008.

Xiang, Z. and Spector, M. (2006) 'Biocompatibility of Materials', in *Encyclopedia of Medical Devices and Instrumentation*. John Wiley & Sons, Inc. doi: 10.1002/0471732877.emd012.

Xiao, K. *et al.* (2008) 'Indirect selective laser sintering of apatite-wollostonite glass-ceramic', *Proceedings of the Institution of Mechanical Engineers, Part H: Journal of Engineering in Medicine*. IMECHE, 222(7), pp. 1107–1114. doi: 10.1243/09544119JEIM411.

Xiong, Z. *et al.* (2002) 'Fabrication of porous scaffolds for bone tissue engineering via low-temperature deposition', *Scripta Materialia*, 46(11), pp. 771–776. doi: 10.1016/S1359-6462(02)00071-4.

Yasa, E. and Ersoy, K. (2018) *Additive manufacturing of polymer matrix composites, Aircraft Technology*. Available at: https://www.intechopen.com/books/aircraft-technology/additive-manufacturing-of-polymer-matrix-composites.

Yuan, J. *et al.* (2007) 'Repair of canine mandibular bone defects with bone marrow stromal cells and porous β-tricalcium phosphate', *Biomaterials*, 28(6), pp. 1005–1013. doi: https://doi.org/10.1016/j.biomaterials.2006.10.015.

Zeng, J.-H. *et al.* (2018) 'Scaffolds for the repair of bone defects in clinical studies: a systematic review', *Journal of orthopaedic surgery and research*. BioMed Central, 13(1), p. 33. doi: 10.1186/s13018-018-0724-2.

Zhang, F. *et al.* (2007) 'Bioinspired structure of bioceramics for bone regeneration in load-bearing sites.', *Acta biomaterialia*, 3(6), pp. 896–904. doi: 10.1016/j.actbio.2007.05.008.

Zhang, J. *et al.* (2014) '3D-printed magnetic Fe3O4/MBG/PCL composite scaffolds with multifunctionality of bone regeneration, local anticancer drug delivery and hyperthermia', *Journal of Materials Chemistry B*. The Royal Society of Chemistry, 2(43), pp. 7583–7595. doi: 10.1039/C4TB01063A.

Zhang, R. and Ma, P. X. (1998) 'Poly (hydroxyl acids)/ hydroxyapatite porous composites for bone-tissue engineering. I. Preparation and morphology', *J Biomed Mater Res.*, 44(4)(March 15), pp. 446–55.

Zhang, W. *et al.* (2012) 'Fabrication of a bio-inspired beta -tricalcium phosphate/collagen scaffold based on ceramic stereolithography and gel casting for osteochondral tissue engineering', *Rapid Prototyping Journal*. Emerald, 18(1), pp. 68–80. doi: 10.1108/13552541211193511.

Zhang, W. *et al.* (2015) 'The effect of interface microstructure on interfacial shear strength for osteochondral scaffolds based on biomimetic design and 3D printing', *Materials Science and Engineering: C*, 46, pp. 10–15. doi: https://doi.org/10.1016/j.msec.2014.09.042.

Zhang, X. Z. *et al.* (2018) 'Selective electron beam manufactured Ti-6Al-4V lattice structures for orthopedic implant applications: current status and outstanding challenges', *Current Opinion in Solid State and Materials Science*, 22(3), pp. 75–99. doi: https://doi.org/10.1016/j.cossms.2018.05.002.

Zhong, W. *et al.* (2001) 'Short fiber reinforced composites for fused deposition modeling', *Materials Science and Engineering: A*, 301(2), pp. 125–130. doi: 10.1016/S0921-5093(00)01810-4.

Zhou, W. Y. *et al.* (2008) 'Selective laser sintering of porous tissue engineering scaffolds from poly(l-lactide)/carbonated hydroxyapatite nanocomposite microspheres', *Journal of Materials Science: Materials in Medicine*, 19(7), pp. 2535–2540. doi: 10.1007/s10856-007-3089-3.

ZIMMER (no date) *Products*. Available at: http://www.zimmer.co.uk/medical-professionals/products/hip.html (Accessed: 13 April 2017).

Zocca, A. *et al.* (2014) 'Powder-bed stabilization for powder-based additive manufacturing', *Advances in Mechanical Engineering*. SAGE Publications, 6, p. 491581. doi: 10.1155/2014/491581.

Zwingenberger, S. *et al.* (2012) 'Recommendations and Considerations for the Use of

Biologics in Orthopedic Surgery', *BioDrugs*, 26(4), pp. 245–256. doi: 10.1007/BF03261883.

Appendix – Conferences, journal papers and awards

Invited talks

2018	TCT conference and exhibition 2018, Birmingham, U.K.
	Health in 3D workshop 2018, Terceira, Portugal.

Oral presentations at national and international conferences

2017	Young Ceramist in Additive Manufacturing forum (yCAM). Berlin Germany.
2018	42nd International conference on advanced ceramics and composites. Daytona Beach, USA;
	Young Ceramist in Additive Manufacturing forum (yCAM). Padova, Italy.
2019	Young Ceramist in Additive Manufacturing forum (yCAM). Mons, Belgium;
	Tissue Engineering and Regenerative Medicine International Symposium. Rhodes, Greece.

Poster communications at national and international conferences

2017	MeDe conference. Bradford, United Kingdom.

Arthritis UK workshop. Newcastle Upon Tyne, United Kingdom.

Awards

2017	Travel award for the Young Ceramist in Additive Manufacturing forum (yCAM). Attributed by JECS Trust.
2018	Travel award to attend the 42nd International conference on advanced ceramics and composites. Attributed by the American Ceramics Society;
	Travel award for conference organisers Young Ceramist in Additive Manufacturing forum (yCAM). Attributed by JECS Trust.
2019	Travel award for conference organisers Young Ceramist in Additive Manufacturing forum (yCAM). Attributed by JECS Trust.

Media appearances

1. Women in 3D printing –Interview for the web page as a member of the community (https://womenin3dprinting.com/priscila-melo-i-was-most-excited-about-the-printing-of-cardiac-cells-and-the-fact-that-you-could-actually-see-them-pulsing-just-like-a-myocardium-cells-it-was-like-seeing-a-heart-beating-in-smal/);
2. 3Med Net – published article on the blog (https://www.3dmednet.com/users/14012-3dmednet/posts/19807-binder-jetting-processing-parameters-and-application-in-orthopedics);
3. Local newspaper interview (pdf attached);
4. Regional newspaper interview (pdf attached).

Journal publications

Morris, S. et al., 2016. Complex functional surface design for additive manufacturing. *Conference: 26th Solid Freeform Fabrication Symposium*, pp.1–5.

Melo, P. et al., 2019. Short phosphate glass fiber - PLLA composite to promote bone mineralization. *Materials Science and Engineering: C*, 104, p.109929. Available at:

http://www.sciencedirect.com/science/article/pii/S0928493118338414.

Melo, P. et al., 2019. Osteoinduction of 3D printed particulate and short-fibre reinforced composites produced using PLLA and Apatite-Wollastonite. *Composites Science and Technology*. [Under publication]